

---

# Resolution dependence of cumulus statistics in radiative-convective equilibrium

Katrin Scheufele

---



München 2014



---

# **Resolution dependence of cumulus statistics in radiative-convective equilibrium**

**Katrin Scheufele**

---

Dissertation  
an der Fakultät für Physik  
der Ludwig-Maximilians-Universität  
München

vorgelegt von  
Katrin Scheufele  
aus Weingarten

München, August 2014

Erstgutachter: Prof. Dr. George C. Craig  
Zweitgutachter: Prof. Dr. Roger K. Smith  
Tag der mündlichen Prüfung: 25.11.2014





# Contents

<b>Zusammenfassung</b>	<b>ix</b>
<b>Abstract</b>	<b>x</b>
<b>1 Introduction</b>	<b>1</b>
1.1 Cumulus clouds . . . . .	1
1.1.1 Convective processes and their interactions . . . . .	2
1.1.2 Simulating convective clouds . . . . .	4
1.2 Variability in a cumulus cloud ensemble . . . . .	6
1.2.1 Distribution of cumulus cloud size . . . . .	6
1.2.2 A theory on cloud mass flux . . . . .	8
1.3 What resolution is cloud-resolving? . . . . .	9
1.3.1 Large-Eddy Simulations . . . . .	10
1.3.2 Inertial subrange . . . . .	11
1.4 Thesis approach . . . . .	12
<b>2 Model description</b>	<b>15</b>
2.1 Introduction . . . . .	15
2.2 The LES model EULAG . . . . .	15
2.2.1 Model equations . . . . .	15
2.2.2 Subgrid model . . . . .	17
2.2.3 Moist microphysics . . . . .	18
2.2.4 Surface fluxes . . . . .	21
2.2.5 Other technical details . . . . .	22
2.3 Control simulation setup . . . . .	23
<b>3 Control simulations</b>	<b>25</b>
3.1 Evolution to radiative-convective equilibrium . . . . .	25
3.2 The simulated equilibrium state . . . . .	28
3.2.1 Equilibrium vertical profiles . . . . .	28
3.2.2 Response to changes in the forcing . . . . .	31
3.2.3 Cloud field structure . . . . .	33
3.3 Statistics of the equilibrium convective ensemble . . . . .	35

---

3.3.1	Sensitivity to the large-scale forcing . . . . .	35
3.3.2	Convective variability in statistical equilibrium . . . . .	37
3.3.3	Cloud field statistics . . . . .	42
<b>4</b>	<b>Resolution dependence of equilibrium convection</b>	<b>47</b>
4.1	Dependence of the simulated atmosphere . . . . .	48
4.1.1	Equilibrium vertical profiles . . . . .	48
4.1.2	Cloud field structure . . . . .	52
4.1.3	Convergence of the simulated atmosphere . . . . .	54
4.2	Sensitivity of equilibrium convective ensemble statistics . . . . .	58
4.2.1	Distribution of cloud size . . . . .	58
4.2.2	Distribution of cloud mass flux . . . . .	61
4.2.3	Properties of the convective ensemble . . . . .	72
4.3	Resolution dependence of the cloud field . . . . .	79
4.3.1	Cloud number and mass flux density . . . . .	79
4.3.2	Cloud number and mass flux variance . . . . .	82
<b>5</b>	<b>Summary and discussion</b>	<b>87</b>
	<b>List of abbreviations and symbols</b>	<b>96</b>
	<b>Bibliography</b>	<b>99</b>
	<b>Acknowledgements</b>	<b>107</b>
	<b>Curriculum vitae</b>	<b>108</b>



# Zusammenfassung

Ein theoretisches Modell welches die Fluktuationen innerhalb eines Wolkenensembles beschreibt, stellt die Basis für stochastische Konvektionsparametrisierung dar. Hochaufgelöste, idealisierte Simulationen eines Wolkenensembles über einer homogenen Meeresoberfläche werden benutzt um die Gültigkeit des theoretischen Modells im Strahlungs-Konvektions-Gleichgewicht zu evaluieren. Im ersten Schritt dieser Studie werden Kontrollsimulationen mit einer horizontalen Auflösung von 2 km durchgeführt, wobei fünf verschiedene Abkühlungsraten benutzt werden um das Wolkenensemble anzutreiben. In den Kontrollsimulationen wird die Gültigkeit einer exponentiellen Verteilung des vertikalen Massenflusses und der Wolkengrößen für alle Abkühlungsraten nachgewiesen. Desweiteren, nimmt die Anzahl der Wolken im Modellgebiet mit steigender Abkühlungsrate linear zu, wohingegen nur eine schwache Abhängigkeit der mittleren Wolkengrößen und deren Vertikalgeschwindigkeiten von der Stärke der Abkühlungsrate beobachtet wird. Diese Ergebnisse zeigen eine gute Übereinstimmung mit dem theoretischen Modell.

Im zweiten Teil dieser Studie wird die Gitterweite in den numerischen Simulationen sukzessive bis zu einer Auflösung von 125 m verfeinert. Hierbei treten signifikante Änderungen in der Wolkenstatistik und der Struktur der Wolkenfelder auf. Die Größe der Wolken nimmt mit zunehmender Auflösung stark ab, wohingegen die Anzahl der Gitterpunkte innerhalb einer Wolke ansteigt, da diese mit zunehmender Auflösung besser auf dem numerischen Gitter dargestellt werden können. Im Gegensatz zu den zufällig verteilten Wolken in den Kontrollsimulationen, wird in den feinaufgelösten Wolkenfeldern beobachtet, dass sich die einzelnen konvektiven Zellen in bandartigen Strukturen um wolkenfreie Gebiete anordnen. Der Umkreis einer Wolke in dem diese Cluster-Effekte beobachtet werden, scheint indes unabhängig von der horizontalen Auflösung zu sein. Mit feiner werdender Auflösung weicht darüber hinaus die Wahrscheinlichkeitsdichteverteilung der Wolkengrößen und des vertikalen Massenflusses immer stärker von der exponentiellen Verteilung ab. Für größere Werte in den Verteilungen zeigen sich Übereinstimmungen mit einer *Power-Law* Verteilung. Durch die Partitionierung der Wolken-Cluster in deren zugrundeliegende, einzelne Aufwindbereiche kann die erwartete, exponentielle Verteilung des Massenflusses und der Wolkengrößen wieder hergestellt werden. Das theoretische Modell ist daher in hochaufgelösten Simulationen für die einzelnen Aufwindbereiche gültig, allerdings müssen die Cluster-Effekte im Wolkenensemble hierbei berücksichtigt werden.



# Abstract

A theoretical model describing equilibrium fluctuations within a field of cumulus clouds is the basis for a stochastic parameterisation of cumulus convection. High-resolution simulations of an idealised ensemble of cumulus clouds over a uniform sea surface are performed to validate the theoretical model in radiative-convective equilibrium. First, a set of control simulations with a horizontal resolution of 2 km is conducted by applying five different radiative cooling rates in the range of -2 K/day to -12 K/day. Evaluating fluctuations within the equilibrium convective ensembles, the frequency distributions of cloud size and cloud vertical mass flux are validated to fit an exponential over a wide range of heights as well as the entire range of the prescribed forcing. Furthermore, a linear increase of the number of clouds in the domain with the magnitude of the prescribed forcing is obtained. In contrast, only a weak dependence on the forcing is observed for cloud size and cloud vertical velocity. These findings agree well with the theoretical model.

In the second part of this study, the full set of control simulations is repeated at smaller grid spacings of 1 km, 500 m, 250 m and 125 m. Significant changes in cloud statistics and the structure of the cloud fields are obtained when increasing horizontal resolution. Cloud size systematically decreases, whereas the number of grid points per cloud increases as the clouds and their turbulent, subcloud processes become better resolved with increasing resolution. In contrast to the randomly distributed cloud fields in the control simulations, clouds are observed to cluster and organise in band-like structures around cloud-free areas in the high-resolution simulations. This clustering of convective clouds in the near-cloud environment systematically increases with increasing horizontal resolution. However, the area surrounding each cloud where the clustering occurs, is found to be insensitive to changes in the grid spacing. Furthermore, strong deviations from the exponential distributions become apparent at smaller grid spacings. A transition from an exponential to a power law-like distribution is observed for cloud size and cloud mass flux with increasing horizontal resolution. However, applying a cloud search algorithm that partitions large clusters of spatially connected clouds into their single updrafts, restores the exponential distributions of cloud mass flux and cloud size. The theoretical model is thus validated in this resolution-sensitivity study when partitioning large cloud clusters into the single updrafts. However, one needs to adapt the theory to account for the observed clustering of convective clouds in the high-resolution cloud fields.



# Chapter 1

## Introduction

### 1.1 Cumulus clouds

Cumulus clouds are observed in the earth's atmosphere on a daily basis and are associated with strong vertical velocities, turbulence and precipitation. Their transport of heat, water and momentum is of central importance in the atmospheric energy cycle as are their radiative effects. Furthermore, they play an important part in the dynamics of the atmosphere as many scales are known to interact with them (Smith, 1997). A thorough understanding of their development and underlying processes is hence of great importance for daily weather forecasts, numerical simulations of mesoscale atmospheric dynamics as well as climate predictions.

Two different types of cumulus clouds are dominant phenomena in the earth's atmosphere: shallow cumulus clouds and deep precipitating cumulus clouds. Shallow cumulus clouds are often observed in fair weather periods (Stevens, 2005). They are shallow, short lived and form very little precipitation as almost all water that condenses inside these clouds, eventually re- evaporates (Smith, 1997). Examples of shallow cumulus clouds regularly observed in the earth's atmosphere are trade wind cumulus clouds and stratocumulus clouds. In contrast, deep cumulus clouds develop from shallow cumulus clouds, exhibiting a significantly larger vertical extend and higher vertical velocities. They often rise to altitudes of order 10 km and interact with the upper troposphere as well as the lower stratosphere (Stevens, 2005). Deep cumulus clouds are therefore essential for the atmospheric energy cycle due to their vertical transport of heat, water and momentum. Shallow and deep cumulus clouds can both appear isolated or organised in lines and clusters, with observed cloud sizes ranging from less than 100 m to tens of kilometers. Taking into account mesoscale organisation and large cloud clusters further extends this range of observed cumulus clouds sizes (Heus and Seifert, 2013).

### 1.1.1 Convective processes and their interactions

Cumulus clouds develop in vertical motions, which result from instabilities in the atmosphere. In general the atmosphere can be either stable, unstable or conditionally unstable. In a conditionally unstable atmosphere, a parcel of air is stable to upward vertical displacements as long as it is unsaturated. However, when the air parcel is lifted it cools due to decompression and becomes saturated if lifted high enough. The condensation of water within the air parcel then provides an extra source of energy and the air parcel becomes unstable. Conditional instability in the atmosphere is therefore important for the development of cumulus clouds. The cumulus clouds then form via moist convective processes. Convection in general can be understood as a transport process within the atmosphere where heat, moisture and momentum from the surface are moved upwards and are re-distributed throughout the atmosphere (Cohen, 2001).

To understand the concept of convection, one imagines a parcel of air, locally warmer than its environment. This parcel of air is considered to be buoyant as its temperature is warmer and it is therefore lighter than the surrounding air. The buoyant air parcel will rise upwards in a characteristic, intense plume. As air rises in the atmosphere it undergoes decompression and cools. This cooling causes the contained water vapour to condense into liquid water when the air parcel is cold enough and becomes saturated. The latent heat released by this phase change in turn constitutes an extra source of energy to the upward motion. Buoyant air parcels generally rise to the level of neutral buoyancy where the density of the air parcel is equal to the density of its environment. The buoyant air parcels rising in a conditionally unstable atmosphere re-stabilise their environment through transport processes of heat and moisture. Heat and moisture are moved upwards and the slowly descending air in the cloud-free areas undergoes compression, hereby warming the environment (so-called subsidence warming).

Figure 1.1 exhibits a schematic of a convective cumulus cloud and the most important physical processes involved in its life cycle. Five main processes are observed within a single convective cloud. First, the buoyant air parcels rise from the surface transporting heat, moisture and momentum upward throughout the troposphere (Figure 1.1 (1)). Turbulent mixing with and entrainment of environmental air occurs at the cloud edges. Meanwhile, as the parcels rise and cool, water vapour condenses and latent heat is released providing additional energy to the upward motion of the buoyant parcels. Second, as the cloud ascends to the level of neutral buoyancy, detrainment of liquid water and cloud ice occurs at cloud top (Figure 1.1 (2)). In the cloud-free environment, the cloud condensate then re-evaporates which results in a cooling and moistening of the environmental air. Third, subsidence occurs in the cloud-free environment, warming the atmosphere as air parcels compress while descending (Figure 1.1 (3)). Fourth, water vapour condenses during the vertical development of the cloud as the rising air parcels expand and cool. Due to collision of these cloud droplets in the turbulent rising motions within the developing cumulus clouds, the cloud droplets grow and fall out as precipitation when reaching a certain droplet size (Figure 1.1 (4)). Taking into account the net loss of moisture by convective processes

leads to an overall heating effect of precipitating cumulus clouds (Cohen, 2001). The drag caused by the falling precipitation and re-evaporation of rain below the cloud base provokes the development of negatively buoyant downdrafts (Figure 1.1 (5)). Cool, dry air from the free troposphere is transported directly into the boundary layer and the downdrafts spread into gust fronts at the surface, enhancing the local surface winds (Cohen, 2001). In connection with these so-called cold pools, an accumulation of moisture in patches around the cold pools is observed and new convective clouds are found to form on top of these moist patches (Tompkins, 2001; Khairoutdinov et al., 2009; Boing et al., 2012; Schlemmer and Hohenegger, 2014).

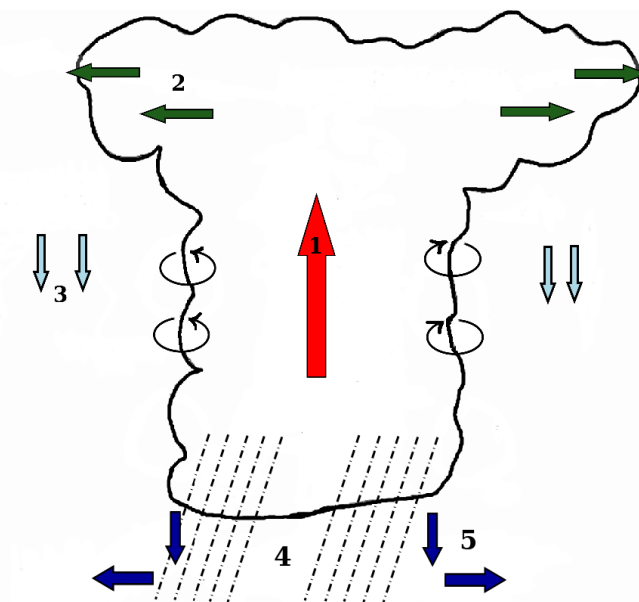


**Figure 1.1:** Schematic of main physical processes within a deep convective cumulus cloud.

Generally, an external source of energy or motion in the atmosphere is necessary to cause the development of cumulus clouds. This source of energy may for example be provided by surface fluxes of sensible and latent heat. Air parcels close to the surface will warm and moisten, causing bubbles of warm air to rise upwards. Furthermore, cooling due to thermal radiation can render the atmosphere unstable to air parcels rising from the warm surface. On the other hand, orographic and pre-frontal lifting of moist and warm air are often the underlying process for the development of cumulus clouds.

Therefore, many scales of the atmospheric flow are known to interact with cumulus clouds. Shallow, isolated cumulus clouds warm the atmosphere while transporting moisture upward and offsetting subsidence drying. Water vapour converges in the tropics where deep convective cumulus clouds develop. This is essential for the vertical transport of heat and moisture, balancing the energy budget of the equatorial trough zone (Johnson et al., 1999). Thereby, cumulus clouds constitute an energy source for large-scale atmospheric circulations, like the Hadley and Walker cells (Johnson et al., 1999) and are also known to provide

the fuel for tropical and extratropical cyclones (Cohen, 2001). Long-lived cloud systems, like squall lines for example, can develop in the presence of large-scale environmental wind shear and have a large impact on regional climate due to their precipitation. Cumulus clouds also have a significant influence on the climate considering radiative-convective feedbacks due to the influence of the deep convective clouds and their associated anvil cloud cover on the radiation budget. In addition, a wide range of studies has shown that clouds in general are highly heterogeneous entities with temperature, buoyancy and vertical velocity varying significantly among the air parcels that make up a single cloud (Warner, 1977; Jonas, 1990; Romps, 2010). Furthermore, a convective cumulus cloud is a complex process combining motions on different scales in space and time. Mesoscale atmospheric systems with scales up to thousands of kilometers often provide the *forcing* for the convective processes over a time scale of several days. In contrast, subcloud processes such as mixing, entrainment, detrainment and cloud microphysics occur down to scales of millimeters and seconds (Cohen, 2001; Heus and Seifert, 2013). It is a natural consequence that the interactions of this wide range of scales are difficult to represent in numerical simulations of convective cumulus clouds in the atmosphere. Further information regarding the issue of numerical simulations of cumulus clouds is provided hereinafter.

### 1.1.2 Simulating convective clouds

Representing interactions and effects of deep moist convection on the atmosphere is a key issue in numerical modeling with meteorological applications. Three ways of including deep moist convection in numerical simulations are commonly used in the scientific community. First, within global models simulating large-scale atmospheric phenomena, a grid spacing of order 10 km or larger is applied. These large-scale phenomena often provide the forcing that drives the convective cumulus cloud ensembles. However, when applying a grid spacing of order 10 km or larger, cumulus clouds and their underlying convective processes cannot be adequately represented by the resolved-scale motions. Hence, these models require some form of a convective parameterisation to represent the mean effect of the subgrid convective processes on the large-scale environment (see next paragraph).

Second, cloud-resolving models with a grid spacing of order 1 km are used on the global- and mesoscale. Within these so-called cloud-permitting models, deep convective clouds can be resolved on the model grid. However, the grid spacing is too coarse to explicitly simulate subcloud turbulent processes.

Third, large-eddy models do have the ability to reproduce local effects of convection by explicitly simulating convective clouds and their subcloud processes. However due to their limited domain size, these models are not capable of representing the interactions of cumulus convection with the mesoscale systems that provide the large-scale forcing of the cloud ensembles. In these high-resolution simulations of cumulus clouds, the forcing has to be provided via a prescribed large-scale radiative cooling that renders the atmosphere unstable and allows for convective processes to develop. Further information about large-eddy models is given in section 1.3.



## Convective parameterisation

In simulations of large-scale atmospheric phenomena with a grid spacing of order 10 km, cumulus clouds cannot be resolved on the model grid. Therefore, the mean effect of the unresolved convection within a model grid box on the simulated atmospheric state needs to be represented by a parameterisation. A convective parameterisation scheme aims to derive the statistical properties of the unresolved convective processes from the large-scale atmospheric properties and the forcing. Cumulus parameterisation schemes are generally based upon a local-equilibrium hypothesis, where it is assumed that the average properties of the (unresolved) convection within each grid box can be determined solely in terms of the large-scale (resolved) conditions. Therefore, one seeks a limited number of equations that govern the statistics of a system with huge dimensions (Arakawa, 2004).

Since the introduction of the first cumulus parameterisation in the early 1960s a number of different approaches has been formulated to represent cumulus convection in numerical models. Traditionally, convective parameterisation schemes are deterministic. The instantaneous grid-scale flow is taken as input and the scheme produces feedbacks to that flow from the subgrid convective motions. However, there may be a wide range of convective, subgrid states that are consistent with the resolved-scale flow due to a lack of scale separation between the convective motions and the resolved flow. Therefore, a deterministic scheme has to be regarded as an attempt to evaluate the ensemble-mean effect of the possible subgrid states (Xu et al., 1992; Plant and Craig, 2008).

The earliest and simplest convective parameterisation scheme was developed by Manabe and Strickler (1964) who simply adjusted the vertical moisture and heat in a grid box if the temperature lapse rate indicated conditional instability. A more advanced convective adjustment approach was proposed by Betts and Miller (1986), where temperature and moisture fields are simultaneously relaxed towards observed quasi-equilibrium, thermodynamic structures. Separate schemes for deep, precipitating and shallow, non-precipitating convection were derived in Betts (1986) and Betts and Miller (1986). In contrast, convective parameterisations by Fritsch and Chappell (1980) and Kain and Fritsch (1993) apply the convective available potential energy (effectively the positive buoyancy of an air parcel) in their closure assumptions. An equilibrium between surface enthalpy fluxes and input of low entropy air into the subcloud layer by convective updrafts is assumed in Emanuel and Rothman (1999).

Arakawa and Schubert (1974) assumed that convection can be represented as an ensemble of entraining and detraining plumes with different heights and entrainment rates. They furthermore concluded that the modification of the large-scale thermodynamic fields by a cumulus ensemble mainly depends on the total mass flux within the cloud ensemble. This cloud mass flux approach provides the basis for many other parameterisation schemes (Tiedtke, 1989; Moorthi and Suarez, 1992; Grell, 1993).

As noted above, a deterministic parameterisation scheme aims to represent the mean effect of the individual unresolved clouds within a grid box. However, a wide range of subgrid states may be consistent with the resolved-scale flow. Furthermore, strong inter-

actions between convective fluctuations, non-linearities in the convective system and the resolved-scale dynamics exist in the atmosphere. This motivates the application of stochastic elements in cumulus cloud parameterisation schemes to account for these uncertainties (Plant and Craig, 2008). Approaches range from introducing a stochastic forcing (Buizza et al., 1999; Palmer, 2001; Bright and Mullen, 2002; Wilks, 2005), evaluating the fractional area of a grid box that supports deep convection to involving systematically derived cloud birth/death processes (Khouider et al., 2003). Furthermore, random perturbations to the convective available potential energy or the vertical heating profile are used as a basis for stochastic parameterisations of deep convection (Lin and Neelin, 2003).

However, these parameterisation schemes use rather ad hoc assumptions about the scales and structures of the convective variability. Ultimately, a stochastic parameterisation scheme of deep convection should be based on systematic observations or simulations of the convective behaviour though. One approach of a stochastic cumulus parameterisation, designed to produce this “correct” convective variability is developed by Plant and Craig (2008). In this stochastic parameterisation scheme a theoretical model describing the equilibrium convective statistics (Craig and Cohen, 2006) (see next section) is applied. Different theories on the convective variability within a cloud ensemble are described in the next section.

## 1.2 Variability in a cumulus cloud ensemble

Strong interactions between convective fluctuations, non-linearities in the convective systems and the resolved-scale dynamics exist in the convecting atmosphere. Reproducing the correct variability present in cumulus cloud ensembles within a convective parameterisation scheme is therefore essential. However, this poses a challenge to the meteorological community (Khouider et al., 2003; Lin and Neelin, 2003; Plant and Craig, 2008) as representing fluctuations in convective cloud ensembles first requires a knowledge of the variability observed in these ensembles. Ideally, this knowledge would be based on systematic observations of cumulus cloud ensembles. However, systematic direct measurements of cloud size and in-cloud properties like vertical mass flux, entrainment or detrainment rates are not feasible up to this point. Deriving theories on the convective behaviour in cumulus cloud ensembles has therefore been and still is an important topic of research in the scientific community. The distribution of cloud size in a cumulus cloud ensemble is of great interest in this context and discussed in the first part of this section. In the second part, a theory on the distribution of cloud mass flux is presented.

### 1.2.1 Distribution of cumulus cloud size

In the past, studies regarding the physical structure of a convective cloud field have primarily focused their attention on the particular size distribution of the cumulus clouds. Up to today however, there is no general agreement on a universal functional form for the

distribution of cumulus cloud sizes (Lennard, 2004). Using photographs of cumulus cloud fields taken from aircrafts over Florida, Plank (1969) was amongst the first to conduct a cumulus cloud size study. He obtained the number density of the cumulus clouds to decrease approximately exponential with increasing diameter of the clouds in early morning cloud fields. His theory however, failed to describe the cloud populations in the afternoon (Plank, 1969; Lennard, 2004). Other observational studies by Hozumi et al. (1982) and Wielicki and Welch (1986) using photographs and satellite images also proposed an exponential distribution of cumulus cloud size.

Studies suggesting a log-normal distribution were undertaken by LeMone and Zipser (1980) and Lopez (1977), investigating convection over the tropical eastern atlantic as well as radar echoes of tropical disturbances. LeMone and Zipser (1980) found cloud diameter, average vertical velocity and mass flux to be approximately log-normally distributed, whereas Lopez (1977) obtained log-normal behaviour analysing cloud mass flux and average cloud sizes. In contrast, evaluating satellite data, Machado and Rossow (1993) observed a single power law distribution in deep convective cloud fields including clusters of individual convective cells. Applying an eight-connected segmentation technique to define the convective clouds, this single power law behaviour was found to be valid up to cloud cluster radii of 50 km.

The shape most often observed in cloud size studies of shallow convection, is a double power law distribution. One of the first studies obtaining a double power law distribution was undertaken by Cahalan and Joseph (1989). Obtaining different power law exponents for various cloud types, they suggested a scale break to exist at the size of the largest individual shallow convective cell and that any cloud larger than this size, is actually made up of smaller clouds (Cahalan and Joseph, 1989; Lennard, 2004).

Other studies revealing double power law distributions of shallow cumulus cloud size were conducted by Kuo et al. (1993), Nair et al. (1998), and Neggers et al. (2003). Different cloud sizes at the scale break and different power law exponents have been obtained in their studies. Comparing cloud size density distributions from cloud-resolving models with observational data, Neggers et al. (2003) observed a distinct scale break at a cloud size of 1 km. Double power law behaviour with a scale break at 1 km has also been found in the tracking of shallow cumulus clouds in numerical simulations performed by Heus and Seifert (2013) and Dawe and Austin (2012).

It was concluded in Lennard (2004) that it is sometimes possible to fit more than one functional form to cloud data and that variations in cloud size distributions may sometimes be explained by differences in data analysis techniques. Analysing model data of simulations of deep convective cloud ensembles at different height levels revealed the distribution of cloud sizes to be exponential at most of the vertical levels and a double power law with a distinct scale break to be a reasonable fit for the others. However, Lennard (2004) claims the size distribution might mistakenly be found to resemble an exponential when the range of cloud sizes is limited by the grid spacing used, causing the entire spectrum of clouds to fall on one side of the scale break size.

### 1.2.2 A theory on cloud mass flux

Convective parameterisations based on vertical mass flux (Tiedtke, 1989; Plant and Craig, 2008) require an additional knowledge of the particular distribution of cloud vertical mass flux in the convective cloud ensembles. In contrast to cloud size, the upward mass flux within convective cloud ensembles cannot be obtained from photographs or measured by airplanes. Hence, one needs to rely on theories proposing the structure and variability of cloud mass flux in cumulus cloud fields. Parameterisations of cumulus convection are generally based upon a local-equilibrium hypothesis, where it is assumed that the average properties of the (unresolved) convection within each grid box can be determined solely in terms of the large-scale (resolved) conditions.

In the absence of large-scale circulations, the tropical atmosphere assumes a state of radiative-moist-convective equilibrium in which the divergence of the net vertical radiative flux is compensated by the convergence of the vertical flux of enthalpy in convective clouds. The paradigm of moist convection in a state of radiative-convective equilibrium is highly idealised and has been found to be unstable to large-scale perturbations. However, this idealised state has been very useful for understanding many aspects of deep convection and invaluable in studies of climate sensitivity (Manabe and Strickler, 1964; Asai and Najasuji, 1977; Held et al., 1993; Randall et al., 1994; Parodi and Emanuel, 2009).

Within the concept of a radiative-convective equilibrium, the atmosphere is rendered unstable through a combination of radiative cooling (radiative forcing), large-scale ascent and surface fluxes of latent and sensible heat. Moist convection, consisting of moist updrafts and downdrafts, then acts to reduce this instability by the vertical transport of heat and moisture. Air mass descending between the convective updrafts warms the atmosphere by adiabatic compression (subsidence warming) and thus restores stability of the simulated atmosphere (Craig and Cohen, 2006). Several studies have used three-dimensional simulations integrated to a state of radiative-convective equilibrium, evaluating the convective feedbacks to changes in the magnitude of the prescribed forcing (Tompkins and Craig, 1998a; Robe and Emanuel, 2001; Pauluis and Held, 2002).

A statistical model describing the fluctuations of cloud upward mass flux in terms of the same large-scale properties that determine the mean behaviour of the convective ensemble has been derived in Craig and Cohen (2006) and is the basis for a stochastic parameterisation of deep convection (Plant and Craig, 2008). Craig and Cohen (2006) used elementary concepts from statistical mechanics to derive a probability density function of cloud mass flux for an ensemble of weakly interacting clouds in statistical equilibrium. In the equilibrium state the net convective mass flux is constrained by the need to produce subsidence warming equal to the magnitude of the large-scale cooling that poses the forcing of the convective ensemble. Therefore, one can assume that the convective mass flux over an area of interest is constrained by the large-scale flow. The variability within the equilibrium cloud ensemble then comes from the fact that the net upward mass flux is split up among a number of finite sized clouds. However, within a given region containing various clouds of different size and strength, the domain total upward mass flux again must approach this

net upward mass flux if the region is very large (Craig and Cohen, 2006). Assuming that the forcing of convection does not vary significantly over a specific region, that clouds are sufficiently separated, and interactions between neighbouring clouds are weak, Craig and Cohen (2006) derived the probability density function  $p(m)$  of cloud upward mass flux  $m$  to be exponential as depicted in Equation (1.1).

$$p(m)dm = \frac{1}{\langle m \rangle} \exp\left(\frac{-m}{\langle m \rangle}\right) dm \quad (1.1)$$

Angle brackets in Equation (1.1) denote an average over the ensemble of clouds. This result is analogous to the Boltzmann distribution, with  $\langle m \rangle$  playing the role of temperature (Cohen, 2001). To validate their theoretical distribution of cloud mass flux (Equation (1.1)), three-dimensional simulations of an ensemble of cumulus clouds in a state of radiative-convective equilibrium were performed in Cohen and Craig (2006). A horizontal grid spacing of 2 km was applied and radiative cooling rates ranging from -2 K/day to -16 K/day were prescribed. Sensitivity of the cloud mass flux distributions and cloud ensemble statistics to the magnitude of the prescribed forcing was evaluated. The distribution was verified to be exponential over a wide range of heights and found to be independent of the magnitude of the forcing. An increase in the magnitude of the prescribed cooling was found to primarily increase the number of clouds observed in the domain. The shape of the distribution was shown to be almost insensitive to changes in the forcing though. In general, numerical models with a grid spacing of 2 km are not capable of accurately representing the complex turbulent flow that makes up a cumulus cloud (Craig and Dörnbrack, 2008). However they are often referred to as “cloud-resolving”. The question what resolution is indeed cloud-resolving is investigated in the following section.

### 1.3 What resolution is cloud-resolving?

Until recently, cloud models with a grid spacing in the range of 1 km to 2 km have been referred to as *cloud-resolving* or *cloud-permitting* and considered sufficient to simulate deep moist convection (Bryan et al., 2003; Craig and Dörnbrack, 2008). Several studies have used simulations with grid spacings of order 1 km as *ground truth* when evaluating coarser resolution simulations of convective processes (Weisman et al., 1997). The long history of simulations with grid spacings of order 1 km followed from a scale analysis associated with deep moist convection. It is clear from earlier studies that a grid spacing of order 1 km captures the basic structures of the convective clouds, but is clearly insufficient to resolve any intracloud motions like the subcloud-scale turbulent eddies for example. It is commonly assumed that subgrid turbulence parameterisations account for these unresolved motions. However, the appropriateness of applying such a turbulence closure at these grid spacings has never been confirmed.

Recent advances in massively parallel computing at national supercomputers facilitated simulations of convective cloud ensembles at horizontal resolutions of order 100 m. A

strong sensitivity of simulation results has been obtained in studies applying grid spacings smaller than 1 km (Petch and Gray, 2001; Adlerman and Droegemeier, 2002; Bryan et al., 2003; Grabowski and Morrison, 2008). Thus, it is of importance to identify the grid spacing that in fact is *cloud-resolving* in simulations of cumulus cloud ensembles, explicitly predicting convective clouds and their subcloud turbulent eddies.

### 1.3.1 Large-Eddy Simulations

Simulating deep convective processes does require the structure of the convective clouds to be resolved on the model grid. Furthermore, the subcloud turbulent eddies need to be represented correctly. The challenge of simulating turbulent flows becomes apparent when taking a close look at the Navier-Stokes equation for an incompressible flow as denoted in Equation (1.2). The variable  $u_i$  denotes velocity,  $p$  pressure,  $\rho$  density and  $\nu$  the molecular kinematic viscosity.

$$\frac{\partial u_i}{\partial t} = -\frac{\partial u_i u_j}{\partial x_j} - \frac{1}{\rho} \frac{\partial p}{\partial x_i} + \nu \frac{\partial^2 u_i}{\partial x_j \partial x_j} \quad (1.2)$$

In direct numerical simulations of a turbulent flow it is essential to resolve all scales of motion as energy is generated by the largest eddies in the flow and dissipated at the smallest scales (Lilly, 1967; Bryan et al., 2003). A grid spacing of approximately 0.1 mm was derived in Bryan et al. (2003) for accurately resolving these dissipative eddies at the Kolmogorov microscale  $\eta$ . Simulating ensembles of deep convective clouds at this resolution however, is beyond the computing powers at the national supercomputing facilities today, as well as in the foreseeable future.

An alternative way to simulating the turbulent flows was first proposed by Lilly (1967), commonly known as large-eddy simulations (LES). Spatial filtering Equation (1.2) with the scale of the filtering operator much larger than the Kolmogorov microscale,  $\eta$ , removes the small-scale details from the solution and facilitates an integration with the presently available computer power. Following Bryan et al. (2003), the filtered form of the Navier-Stokes Equation (1.3) can be written as,

$$\frac{\partial u_i^r}{\partial t} = -\frac{\partial u_i^r u_j^r}{\partial x_j} - \frac{\partial \tau_{ij}}{\partial x_j} - \frac{1}{\rho} \frac{\partial p^r}{\partial x_i} \quad (1.3)$$

where all variables are resolved on the model grid except for the new term  $\tau_{ij}$ . Noting that the velocity  $u_i = u_i^r + u_i^s$  denotes the sum of resolved and subgrid components,  $\tau_{ij}$  can be written as,

$$\tau_{ij} = [(u_i^r u_j^r)^r - u_i^r u_j^r] + [(u_i^r u_j^s)^r + (u_i^s u_j^r)^r] + (u_i^s u_j^s)^r \quad (1.4)$$

and has to be accounted for via a parameterisation (turbulence closure problem). Resolving one end of the energy cascade explicitly on the model grid, whereas the other end

is accounted for through the parameterisation of  $\tau_{ij}$  is commonly known as LES modeling. These models have been used successfully to simulate various types of turbulent and geophysical flows in previous studies (Bryan et al., 2003).

### 1.3.2 Inertial subrange

In order for these subgrid LES models to work appropriately to their design, one needs the grid spacing  $\Delta$  to be much larger than the scale of the dissipative eddies  $\eta$ , but much smaller than the scale of the large energy-producing and containing eddies  $l$ ,  $l \gg \Delta \gg \eta$ . In order to ensure that the simulation accurately resolves the large eddies containing most of the kinetic energy and flux in the turbulent flow, the grid spacing  $\Delta$  has to be within the inertial subrange (Moeng, 1984; Bryan et al., 2003).

The inertial subrange denotes the range of wavelengths smaller than the energy-containing but larger than the viscous eddies. In this range the net energy coming from the larger eddies is balanced by the energy cascade to smaller scales. The slope of the energy spectrum in the inertial subrange is constant at  $-5/3$ , commonly known from turbulence theory as 'Kolmogorov-Obukhov  $-5/3$  law' (Kolmogorov, 1941). In simulations of deep moist convection the appropriateness of applying traditional LES closures therefore strongly depends on whether an inertial subrange exists in the numerical simulations. However, the question where the inertial subrange begins in deep moist convection and what grid spacing is necessary for results to converge is still an ongoing topic of research.

Droegemeier et al. (1997) concluded that with a grid spacing of 250 m turbulent features in deep moist convection are beginning to be explicitly resolved. However, no signs of convergence of cloud properties and statistics was observed at this resolution. In resolution tests simulating shallow cumulus convection, Stevens et al. (2002) claimed a grid spacing of approximately 20 m necessary to adequately resolve subcloud processes and obtain reliable statistics. Sensitivity of results to horizontal resolution in the range of 80 m to 10 m was tested in their study.

Bryan et al. (2003) analysed the sensitivity of a simulated squall line to horizontal resolution and observed that a 1 km grid spacing captures the basic structures. However, the correct magnitude and scale of the spectral kinetic energy maximum was not reproduced at this resolution and simulations contained an unacceptable large amount of subgrid turbulent kinetic energy. An inertial subrange was obtained in simulations with grid spacings of 250 m and 125 m. However, the slope of the energy spectra at smaller wavelengths was found to be slightly shallower than the expected  $-5/3$ . Bryan et al. (2003) concluded a horizontal resolution of order 100 m to be necessary for traditional LES closures to perform as designed in their squall line simulations.

Systematic experiments to determine the spatial resolution required to accurately simulate the transport, entrainment and detrainment in a moist thermal were conducted by Craig and Dörnbrack (2008). Two candidates for the dominant turbulence scale were analysed in this study: the diameter of the cloud and the buoyancy length scale. The buoyancy length scale  $L_{buoy}$  describes the maximum vertical displacement that can be induced against the

stratification (stability) of the environment by the buoyancy-driven pressure perturbations in the cloud.  $L_{buoy}$  therefore strongly depends on the stability of the atmosphere and increases with decreasing stability. Results of Craig and Dörnbrack (2008) are consistent with their hypothesis that the smaller of the two length scales determines the resolution requirement for large-eddy simulations of cumulus clouds. They note that for atmospheric values it is likely to be the buoyancy length scale that qualifies for the dominant turbulence scale. Convergence of results in their simulations of a warm moist bubble was obtained at grid spacings of  $\Delta x \approx 0.2 \cdot L_{buoy}$ , where  $L_{buoy}$  in deep cumulus cloud ensembles is typically of a few hundred meters.

## 1.4 Thesis approach

Representing interactions and effects of deep moist convection on the atmosphere is a key issue in numerical simulations with meteorological applications. A theoretical model has been developed by Craig and Cohen (2006), describing the variability within a convective cloud ensemble in terms of the same large-scale properties that determine its mean behaviour. Simulations validating this theory were performed with a grid spacing of 2 km in Cohen and Craig (2006). They predicted the probability density function of cloud vertical mass flux to be exponential over a wide range of height levels and magnitudes of the prescribed radiative cooling (forcing). Furthermore, they found an increase of the prescribed forcing to primarily increase the number of clouds in the domain, whereas the ensemble average cloud mass flux and vertical velocity were observed to be quite insensitive to changes in the forcing.

However, recent studies have shown a grid spacing of order 1 km to be inadequate for resolving subcloud processes and obtaining meaningful statistics of cloud and ensemble properties. Previous resolution sensitivity studies of convective processes have shown a strong sensitivity of simulation results when further refining the grid spacing. Applying horizontal resolutions of at least order 100 m or smaller was suggested in previous studies for resolving subcloud processes, for traditional LES closures to perform appropriately to their design and to obtain convergence of the simulation results. It is therefore of great interest to validate the theoretical model (Craig and Cohen, 2006) in high-resolution simulations and to analyse the convective variability within the equilibrium ensembles of cumulus clouds and their dependence on horizontal resolution and the magnitude of the prescribed forcing.

In the first part of this study, results derived by Cohen and Craig (2006) are reproduced with a numerical fluid solver at a grid spacing of 2 km. Three-dimensional simulations of a cloud ensemble in radiative-convective equilibrium over a uniform sea surface are performed (control simulations). Sensitivity of the simulated cloud ensembles to the magnitude of the prescribed forcing is evaluated following Cohen and Craig (2006).

In the second part of this study, the set of control simulations is repeated, stepwise increasing horizontal resolution from 2 km to 125 m in steps of 1 km, 500 m and 250 m. Changes of the variability in the convective cloud ensembles appearing with increasing resolution



are analysed and sensitivities of cloud and ensemble properties to the grid spacing and magnitude of the prescribed forcing are evaluated in the high-resolution simulations.

### **The objectives of this thesis are as follows:**

- Results of Cohen and Craig (2006) are reproduced with a numerical fluid solver at a horizontal resolution of 2 km. The exponential distribution of cloud vertical mass flux is validated in a set of control simulations prescribing five different magnitudes of a radiative cooling rate. Variability within the cumulus ensembles is analysed and sensitivity of cloud and cloud ensemble properties to changes in the magnitude of the prescribed radiative forcing is evaluated.

### **With increasing resolution, the following questions are then investigated:**

- Is the theoretical, exponential distribution of cloud vertical mass flux valid in high-resolution simulations of cumulus cloud ensembles?
- Does the structure of the simulated cloud fields change with increasing resolution, e.g. exhibiting a trend towards regularity or clustering at finer grid spacings?
- Is the effect that an increase in the magnitude of the forcing has on the properties of the cloud ensemble sensitive to the grid spacing? Is an increase in forcing still primarily increasing the number of clouds in the domain? Are cloud mass flux and cloud vertical velocity insensitive to changes in the magnitude of the forcing at high resolutions?
- Does a power law or a double power law distribution of cloud sizes, obtained in earlier studies of shallow convection, pose an adequate fit to the cumulus cloud size distributions in the high-resolution simulations in this study?
- And finally, are signs of convergence and an inertial subrange present in the high-resolution simulation results?

These questions are investigated performing simulations of a cumulus cloud ensemble in a state of radiative-convective equilibrium with the numerical fluid solver EULAG. A detailed description of this anelastic, non-hydrostatic numerical solver is given in Chapter 2, including a general model description as well as an overview of the subgrid turbulence model and the moist microphysics. Furthermore, the setup of the numerical model for the control simulations is outlined. Chapter 3 describes the evolution of the simulated atmospheric states to their radiative-convective equilibrium states at a horizontal resolution of 2 km (control simulations). Sensitivity of cloud properties and statistics to the magnitude of the prescribed forcing is evaluated and results of the control simulations are compared

to the findings of Cohen and Craig (2006). The effect of stepwise increasing horizontal resolution on the state of the simulated atmosphere is illustrated in Chapter 4. Resolution dependence of cloud field structure, ensemble mean cloud properties and fluctuations of the convective ensemble are investigated. Sensitivity of the results to the method of cloud definition is analysed and underlying subcloud processes are investigated. Findings of this resolution sensitivity study are summarised and discussed in Chapter 5 in the context of current knowledge. In addition, an outlook of possible future work is provided.

# Chapter 2

## Model description

### 2.1 Introduction

In this study an ensemble of cumulus clouds is simulated in a three-dimensional domain over a uniform tropical ocean surface. The cloud ensemble is simulated in a state of radiative-convective equilibrium by applying horizontally uniform radiative cooling rates. Several sets of simulations are conducted, evaluating the sensitivity of the convective ensemble to the prescribed radiative forcing and horizontal resolution. Simulations are performed with the anelastic, non-hydrostatic fluid solver EULAG. The first section of this chapter describes the fluid solver, giving an overview of the governing equations, the numerical solver as well as the subgrid scale and surface flux parameterisations. The second part of this chapter gives an overview of the model setup for the 2 km resolution control simulations.

### 2.2 The LES model EULAG

#### 2.2.1 Model equations

Simulations are performed with the anelastic, non-hydrostatic fluid solver EULAG. The name EULAG alludes to the capability to solve the fluid equations in either an Eulerian (flux form) or a Lagrangian (advective form) mode. For this thesis the Eulerian formulation is chosen as it is better suited for the simulation of clouds (Smolarkiewicz and Margolin, 1997). The fluid solver integrates the anelastic, non-hydrostatic, three-dimensional equations of motion with a second order accurate, semi-implicit, non-oscillatory forward-in-time approach (Smolarkiewicz and Margolin, 1998; Grabowski and Smolarkiewicz, 2002; Smolarkiewicz, 2005). The governing partial differential equations are formulated and solved in generalised, time-dependent, curvilinear coordinates with a semi-implicit scheme (Prusa et al., 2008). The essence of semi-implicit schemes for the dynamics is that both momentum and temperature equations are solved simultaneously. This approach maintains com-

putational stability with respect to internal gravity waves (Grabowski and Smolarkiewicz, 2002). The anelastic equations for the dry adiabatic dynamics can be written as denoted in Equations (2.1) and (2.2).

$$\frac{d\mathbf{u}}{dt} = -\nabla \left( \frac{p'}{\bar{\rho}} \right) + \mathbf{g} \frac{\theta'}{\bar{\theta}} - \mathbf{f} \times \mathbf{u}' + \mathbf{M}' \quad (2.1)$$

$$\frac{d\theta'}{dt} = -\mathbf{u} \cdot \nabla \theta_e \quad (2.2)$$

In these equations  $\mathbf{u}$  denotes the velocity vector, whereas  $\mathbf{g}$  and  $\mathbf{f}$  are vectors of gravity and the Coriolis parameter, respectively.  $\bar{\theta}$  is the base-state anelastic potential temperature profile,  $\mathbf{M}$  symbolises appropriate metric terms and primes generally denote deviations from the ambient (environmental) state, e.g.  $\theta' = \theta - \bar{\theta}$ ,  $\mathbf{u}' = \mathbf{u} - \bar{\mathbf{u}}$ . The perturbation pressure  $p'$  is evaluated via the mass continuity constraint:  $\bar{\nabla}(\bar{\rho}\mathbf{u}) = 0$ .

Each of these prognostic equations forming the anelastic system can be written as either a Lagrangian evolution equation (2.3) or an Eulerian conservation law (2.4). The variable  $\Psi$  symbolises either the components of the velocity vector  $\mathbf{u}$  or the potential temperature deviation  $\theta'$ .  $R$  denotes the associated right hand side of Equations (2.1) and (2.2).

$$\frac{d\Psi}{dt} = R \quad (2.3)$$

$$\frac{d\bar{\rho}\Psi}{dt} + \bar{\nabla}(\bar{\rho}\mathbf{u}\Psi) = \bar{\rho}R \quad (2.4)$$

Equation (2.3) and (2.4) are approximated to second-order accuracy in space and time using a non-oscillatory forward-in-time (NFT) approach as depicted in Equation (2.5). In this equation  $\Psi_i^{n+1}$  denotes the solution sought at the grid point  $(t^{n+1}, \mathbf{x}_i)$ .  $\tilde{\Psi}$  is given by  $\tilde{\Psi} = \Psi^n + 0.5\Delta t R^n$  and LE symbolises the two-time-level either advective, semi-lagrangian or eulerian NFT transport operator as described in Prusa et al. (2008),

$$\Psi_i^{n+1} = LE_i(\tilde{\Psi}) + 0.5\Delta t R_i^{n+1} \quad (2.5)$$

Indices  $i$  and  $n$  in Equation (2.5) denote the spatial and temporal location on a rectangular cartesian mesh, whereas  $\Delta t$  is the time step of the model. The underlying transport operator ( $LE_i$ ) is formulated for arbitrary, curvilinear frameworks and employs the MPDATA (multi-dimensional positive definite advection transport algorithm) methods that are described in detail in Smolarkiewicz and Margolin (1998). MPDATA is a finite-differencing algorithm for approximating the advective terms in fluid equations. It is second-order-accurate in space and time, positive definite, sign preserving and computationally efficient (Prusa et al., 2008). The first pass is a simple donor cell approximation (so-called upstream differencing) that is positive definite but only first order accurate. The second pass increases the accuracy of the calculation by estimating and compensating for the

(second-order) truncation error of the first pass. Additional passes are used to estimate the residual error of the previous pass and approximately compensate for it (Smolarkiewicz and Margolin, 1998). Completion of the model algorithm then requires a straightforward inversion of Equation (2.5), resulting in the formulation of a boundary value problem for pressure, implied by the anelastic mass continuity equation  $\bar{\nabla}(\bar{\rho}\mathbf{u}) = 0$ . The resulting elliptic operator for the anelastic system and a detailed description of the complete pre-conditioned Krylov solver can be obtained from Smolarkiewicz et al. (1998).

### 2.2.2 Subgrid model

Earlier simulations of turbulent flows with the numerical fluid solver EULAG have shown that the non-oscillatory advection scheme MPDATA can accurately reproduce the dynamics of the boundary layer (e.g. Margolin et al., 1999). However, as non-linearities in the Navier-Stokes Equations (Chapter 1, Equation (1.2)) couple the energy at different scales of motion, one cannot simply neglect the unresolved scales of motion. Subgrid scale (SGS) models parameterise the influence of the subgrid scale on the grid scale and the energy transport between resolved and unresolved scales. MPDATA itself has shown to include an effective SGS model, however, in the case of applying an explicit turbulence model, it does not induce any unnecessary, additional diffusion (Margolin et al., 1999). Two options for the subgrid scale model are available in the numerical fluid solver, based on either a Smagorinsky-Lilly approach (Lilly, 1962; Smagorinsky, 1963) or a turbulent kinetic energy approach (Schumann, 1991; Sorbj an, 1996). This study applies the subgrid parameterisation based on the explicit computation of turbulent kinetic energy as described in Sorbj an (1996). In this subgrid parameterisation, the coefficient of the turbulent viscosity  $K_m$  (Equation (2.6)) is assumed to be proportional to the turbulent mixing length  $\lambda_m$  and to the square root of the turbulent kinetic energy  $\text{sqrt}(tke)$ . The subgrid flux terms  $\tau_{ij}$ ,  $H_j$  and  $Q_j$  are then parameterised as denoted in Equations (2.7) to (2.9).

$$K_m = c_m \cdot \lambda_m \cdot \text{sqrt}(tke) \quad (2.6)$$

$$\tau_{ij} = -K_m \left( \frac{\partial u_i}{\partial x_j} + \frac{\partial u_j}{\partial x_i} \right) \quad (2.7)$$

$$H_j = -K_h \left( \frac{\partial \Theta}{\partial x_j} \right) \quad (2.8)$$

$$Q_j = -K_q \left( \frac{\partial q}{\partial x_j} \right) \quad (2.9)$$

The eddy diffusivity coefficients  $K_h$  and  $K_q$  are functions of the subgrid turbulent kinetic energy, the mixing length  $\lambda$  and the Prandtl number  $Pr = K_m/K_h = c_m/c_h$ . The subgrid turbulent kinetic energy satisfies the prognostic equation (2.11) where  $\epsilon$  is the viscous dissipation rate,  $T_j$  denotes the turbulent transport term and  $P_j$  symbolises the pressure

term and is computed as illustrated in Equation (2.10) (Lilly, 1987; Sorbjan, 1996). The turbulent transport terms in Equation (2.11) are then parameterised following Deardorff (1973) as denoted in Equation (2.12) and (2.13).

$$P_j = (\overline{\pi u_j} - \overline{\pi} \overline{u_j}) \quad (2.10)$$

$$\frac{\partial tke}{\partial t} + \frac{\partial u_j tke}{\partial x_j} = \tau_{ij} \frac{\partial u_i}{\partial x_j} + \beta H_3 - \frac{\partial}{\partial x_j} (T_j + P_j) - \epsilon \quad (2.11)$$

$$P_j + T_j = -c_e K_m \frac{\partial tke}{\partial x_j} \quad (2.12)$$

$$\epsilon = c_\epsilon \frac{tke^{3/2}}{\lambda} \quad (2.13)$$

In these equations  $c_e$  and  $c_\epsilon$  are taken to be constant values as described in Schumann (1991) and  $\lambda$  denotes the mixing length  $\lambda = \min(\Delta, c_L z)$ , where the average grid spacing  $\Delta = (\Delta x + \Delta y + \Delta z)/3$  must fall within the inertial subrange. Analogously to Schumann (1991) the following values for the constants in the turbulent transport computations are adopted in this study:  $c_\epsilon = 0.845$ ,  $c_e = 2.0$ ,  $c_m = 0.0856$ ,  $c_h = 0.204$ ,  $c_L = 0.845$ .

### 2.2.3 Moist microphysics

Three moist prognostic variables are available in the anelastic, non-hydrostatic fluid solver: the water vapour mixing ratio  $q_v$ , the cloud condensed water mixing ratio  $q_c$  and the cloud rain water mixing ratio  $q_r$ . In general, moist processes have only a small impact on the mathematical form of the governing equations, as water substance variables enter the dynamics of moist air and clouds only through the buoyancy term in the vertical momentum equation. This is due to water vapour and cloud condensate constituting only a small fraction of the mass of a moist cloudy volume (usually less than 1%). Most importantly, moisture has a negligible effect on the phase speed of gravity waves in the domain. Hence, there is no need for extending the semi-implicit numerics of the dry dynamics model to the moisture variables. The governing anelastic thermodynamic equations are then written as denoted in Equations (2.14) to (2.17) (Grabowski and Smolarkiewicz, 2002). In this set of equations  $\theta_{env}$  and  $T_{env}$  denote the ambient (environmental) potential temperature and total temperature.  $L_v$  is the latent heat of evaporation,  $c_p$  the specific heat at constant pressure and  $V_T$  the terminal velocity of precipitation.  $S_i$  - terms in Equations (2.14) to (2.17) represent sources and sinks in the equations due to processes not directly represented in the above equations (e.g. surface fluxes, subgrid turbulence).

$$\frac{d\theta}{dt} = \frac{L_v \bar{\theta}}{c_p \bar{T}} (C_d + E_p) + S_\theta \quad (2.14)$$

$$\frac{dq_v}{dt} = -C_d - E_p + S_{q_v} \quad (2.15)$$

$$\frac{dq_c}{dt} = C_d - A_r - C_p + S_{q_c} \quad (2.16)$$

$$\frac{dq_r}{dt} = \frac{1}{\bar{\rho}} \frac{\partial}{\partial z} (\bar{\rho} V_T q_r) + A_r + C_p + E_p + S_{q_r} \quad (2.17)$$

Phase change processes are represented by the condensation of water vapour  $C_d$ , the autoconversion term  $A_r$ , deposition/evaporation of precipitation due to diffusion of water vapour  $E_p$ , and the growth of precipitation due to accretion of cloud condensate  $C_p$ . In moist simulations the governing Equations (2.14 - 2.17) are therefore written compactly as denoted in Equations (2.18) and (2.19).

$$\frac{d\mathbf{u}}{dt} = -\nabla \left( \frac{p'}{\bar{\rho}} \right) + \mathbf{g} \frac{\theta'_d}{\bar{\theta}} - \mathbf{f} \times \mathbf{u}' + \mathbf{M}' \quad (2.18)$$

$$\frac{d\theta'}{dt} = -\mathbf{u} \cdot \nabla \theta_e + F_\theta \quad (2.19)$$

Equation (2.18) and Equation (2.19) include the temperature forcing  $F_\theta$  and the modified buoyancy term as denoted in Grabowski and Smolarkiewicz (2002). The buoyancy term is given by  $\mathbf{g} \cdot \theta'_d / \bar{\theta}$  with  $\theta'_d$  being the perturbation of the density potential temperature computed as follows:

$$\theta_d = \theta + \bar{\theta} (\epsilon q_v - q_c - q_p) \quad (2.20)$$

The constant  $\epsilon = R_v/R_d - 1$  depicts the ratio of the gas constants for water vapour and dry air (Emanuel, 1994). Consequently, the temperature forcing  $F_\theta$  and the moisture variables ( $q_v$ ,  $q_c$ ,  $q_r$ ) used for computing the buoyancy term, are evaluated using an explicit scheme. However, for long model time steps the explicit scheme needs special refinement to accurately represent moist processes (Grabowski and Smolarkiewicz, 2002).

As noted previously, EULAG considers only two classes of condensed water: the cloud condensed water mixing ratio  $q_c$  and the cloud rain water mixing ratio  $q_r$ . Depending on the temperature within the grid box, cloud condensate represents either cloud water or cloud ice, precipitable water either rain or snow. Sedimentation of cloud condensate is neglected. The analytic advection-condensation model applied in EULAG is based on the bulk thermodynamics approximation described in Clark (1977) and Clark (1979). Within

this approximation, the condensation rate  $C_d$  is determined by the constraint of zero supersaturation in cloudy regions and zero cloud water in subsaturated conditions.

$$q_v = q_{vs} \quad \text{if } q_c > 0 \quad (2.21)$$

$$q_c = 0 \quad \text{if } q_v < q_{vs} \quad (2.22)$$

The advection-condensation scheme is referred to as fractional-time-steps approach where the amount of water substance being subject to phase change  $\Delta q_v = C_d \Delta t$ , is evaluated by a transcendental equation (Equation 2.23). Within this transcendental equation, the variables  $\theta^*$  and  $q_v^*$  are already updated in the first step of solving the equation (Grabowski and Smolarkiewicz, 1990).

$$q_v^* - \Delta q_v = q_{vs}(\theta^* + \frac{L\bar{\theta}}{c_p T} \Delta q_v) \quad (2.23)$$

This equation is solved by a Newton-Raphson iterative procedure which offers, in principle, arbitrary accuracy and fast convergence (Grabowski and Smolarkiewicz, 1990). In the case of evaporation of cloud water, the amount of water substance being subject to phase change  $\Delta q_v$  is limited by the amount of cloud water present within the grid box. Saturated conditions are defined using the saturated water vapour mixing ratio with respect to a plane of water for temperatures above a threshold temperature,  $T_w = 273$  K, and with respect to a plane of ice for temperatures below a threshold temperature,  $T_i = 263$  K. In between these two thresholds, the coexistence of water and ice is described by a linear interpolation of the water and ice content within the grid box.

Precipitation development and further growth are calculated using formulas appropriate for rain and snow depending on the temperature in a specific grid box. Total growth is then calculated as the sum of the growth rates for the rain and snow part of the precipitation field if the temperature in the grid box falls between the two threshold temperatures. Precipitation is initiated from cloud condensate and either grows by deposition of water vapour and accretion of cloud condensate inside clouds, or evaporates (resublimates) outside of clouds (Grabowski, 1998). The autoconversion term for rain is parameterised according to Berry as applied by Simpson and Wiggert (1969) with coefficients given by Kessler (1969). For snow, the autoconversion is parameterised following studies by Hsie et al. (1980) and Lin et al. (1983). The growth rates due to accumulation and deposition are computed as described in Grabowski (1988) and Grabowski (1998). Analogously to the computation of the growth rates, the mass-weighted terminal velocity of precipitation particles is computed as denoted in Grabowski (1998) for rain and snow separately, with a linear interpolation of the terminal velocities if the grid box temperature falls within the two threshold temperatures.



### 2.2.4 Surface fluxes

In this study an ensemble of cumulus clouds is simulated in a three-dimensional domain over a uniform tropical ocean surface. To account for the upward transport of heat and moisture above a tropical ocean surface, a bulk aerodynamic formula is applied to parameterise surface fluxes of sensible and latent heat similar to Grabowski (1998). Some small adaptations to the bulk aerodynamic formula are made to better account for surface fluxes in small wind speed conditions following Stull (1994) and Schumann (1987). Surface fluxes of latent and sensible heat are hence computed as denoted in Equation (2.24).

$$F_{\Phi} = C_d \cdot U \cdot (\Phi_{srf} - \Phi_{z=0}) \quad (2.24)$$

In this bulk aerodynamic formula, the variable  $\Phi$  denotes either the potential temperature  $\Theta$  or the water vapour mixing ratio  $q_v$ . The index *srf* indicates the prescribed ocean surface values for  $\Theta$  and  $q_v$ . Potential temperature directly above the ocean surface is assumed to be equal to the sea surface temperature (SST) and the lowest model layer above the ocean surface to be saturated at this temperature. Variables with index  $z = 0$  represent the model-predicted values of potential temperature and water vapour mixing ratio for the lowest model level. The drag coefficient  $C_d$  within the surface flux parameterisation is taken to be  $1.2 \cdot 10^{-3}$ , and  $U$  denotes a measure of the strength of the surface wind.

Within this bulk aerodynamic formula (Equation 2.24) the surface fluxes decrease to zero in low wind speed conditions. There are two options to overcome this issue. First, as applied in Grabowski (1998), one can set a minimum wind speed when computing the surface wind  $U$ . Second, and being the option applied in this study, one can add a component  $u_*$  based on the free convective boundary layer scaling to the surface wind  $U$ . In this study the surface wind  $U$  is computed following Equation (2.25) where  $u_{z=0}$  depicts the model-predicted horizontal wind at the lowest model layer.

$$U = \max[0., (u_{z=0}^2 + u_*^2)^{0.5}] \quad (2.25)$$

The component  $u_*$  is computed from the buoyancy velocity scale as described in Stull (1994) following Grabowski (1998) where  $H = 600 \text{ m}$  denotes the assumed height of the boundary layer (Equation (2.26)). The coefficient  $C_s = 0.7$  is chosen following Schumann (1987) to account for the free convective boundary layer scaling in low wind conditions.

$$u_* = g \cdot H \cdot C_s \cdot [(\theta_{srf} - \theta_{z=0})/\theta_{env} + 0.61 \cdot (q_{vsrf} - q_{vsz=0})] \quad (2.26)$$

### 2.2.5 Other technical details

The model grid in this numerical fluid solver is an unstaggered Arakawa-A grid with the lowest model level at height  $z = 0$  m above the surface. A two-dimensional parallel design of the model code greatly enhances the efficacy of the fluid solver by distributing the overall computational load to multiple processors. This distribution to multiple processors has been accomplished applying a two-dimensional horizontal decomposition of the model grid. Each processor is responsible for a subset of the horizontal and all associated grid points in the vertical. Halo cells are used for collecting information from the neighbouring subgrids with a predefined size for array memory allocation. Information between the processors is exchanged employing the Message Passing Interface (MPI). Good scalability of EULAG was obtained in previous studies with the optimal number of processors (NPE) given by  $NPE = \sqrt{n \cdot m}$ , where  $n$  and  $m$  denote the number of horizontal grid points (Prusa et al., 2008; Piotrowski et al., 2011).

In order to prevent the development of a mean horizontal wind during the integration time, a Newtonian relaxation of model wind is applied in these simulations. This method relaxes the model state towards an *observed* state by adding artificial tendencies based on the difference between the two states, to the prognostic equations. The tendencies added to the u- and v-components of the velocity field are computed as denoted in Equation (2.27) where the variable  $\Psi_{relax}$  denotes the *observed* state ( $u_{relax} = v_{relax} = 0 \frac{m}{s}$ ), the variable  $\Psi_{model}$  describes the state of the simulated atmosphere and  $\tau_{relax}$  is the relaxation time scale taken to be 12 hours following Lipps and Helmer (1986) and Robe and Emanuel (2001).

$$\frac{\partial \Psi_{model}}{\partial t} = \frac{\Psi_{relax} - \Psi_{model}}{\tau_{relax}} \quad (2.27)$$

In order to avoid gravity waves from being reflected at the top of the domain, a Newtonian damping layer is applied to the velocity, temperature and moisture fields in the upper part of the domain. Within this damping layer the prognostic variables are slowly relaxed to their environmental mean values. The rate  $R_d$  at which the prognostic values are damped is computed analogously to Cohen and Craig (2006) as denoted in Equation (2.28), where  $H_D = 3$  km denotes the damping layer height scale, and  $\tau_{damp} = 1000$  s is the damping coefficient. The Newtonian damping of the prognostic variables is implemented from a height of  $z_D = 16.75$  km to the highest model level.

$$R_d = \frac{1}{\tau_{damp}} \left[ \exp\left(\frac{z - z_D}{H_D}\right) - 1 \right] \quad (2.28)$$

## 2.3 Control simulation setup

This study investigates the sensitivity of an ensemble of cumulus clouds over a uniform sea surface to the magnitude of the prescribed radiative cooling and the grid spacing. The set of control simulations performed with the numerical fluid solver EULAG consists of five simulations with different magnitudes of the prescribed forcing. The intention is to generate an idealised ensemble of cumulus clouds over the tropical ocean in radiative-convective equilibrium following Cohen and Craig (2006). The development of the equilibrium ensemble is forced by applying a horizontally homogeneous radiative cooling that is constant in time and height up to 400 hPa analogously to Cohen and Craig (2006). Between the levels of 400 hPa and 200 hPa the prescribed cooling rate decreases linearly to zero. Figure 2.1 illustrates the vertical profile of the prescribed radiative cooling with the environmental pressure and the associated height levels.

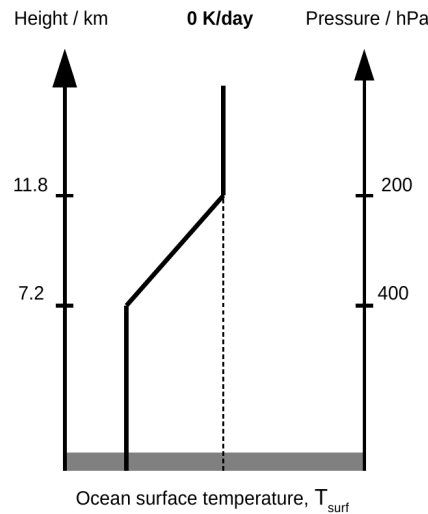


**Figure 2.1:** Schematic of the horizontally homogeneous radiative cooling profile in dependence of the environmental pressure profile and vertical levels of the model.

Prescribing a horizontally homogeneous, non-interactive radiative forcing poses a significant simplification to the atmospheric situation, ignoring all cloud-radiative feedbacks. The motivation for implementing this simplified forcing is threefold. First, a fixed cooling rate is computationally more efficient than an interactive radiation scheme. Second, by applying a fixed radiative cooling rate, the forcing is effectively 'externalised' from the convective activity, allowing the sensitivity of results to the forcing to be extracted unambiguously and cleanly (Cohen, 2001). Third, previous studies with an interactive radiation scheme have shown that especially in interaction with a mean model wind, convection tends to organise in band-like structures after a couple of days (Tompkins and Craig, 1998a). The intention of this study however, is to simulate an ensemble of randomly distributed convective clouds. Several previous radiative-convective equilibrium studies with a fixed cooling

rate have shown to produce realistic cloud ensemble results (Islam et al., 1993; Robe and Emanuel, 1996; Cohen and Craig, 2006).

A three-dimensional computational domain with a size of  $128 \text{ km} \times 128 \text{ km}$  in the horizontal and 20 km in the vertical is set up to simulate the equilibrium convective ensemble. An evaluation of the optimum domain size for these simulations has been undertaken and described in Cohen and Craig (2006). On the one hand, the domain needs to be large enough to contain a sufficient number of clouds in order to generate robust time-averaged statistics and convection occurring continuously throughout the domain. On the other hand, the size of the domain is limited by computing time especially for the high-resolution simulations performed in this study. Tompkins and Craig (1998a) argued that the minimum domain size for a prescribed radiative cooling of  $-2 \text{ K/day}$  is given by  $50 \times 50$  grid points at 2 km horizontal resolution. It is clear though that domain averaged statistics become more robust as domain size increases, which makes a bigger domain desirable. Compromising with limitations of computing time and in line with the study of Cohen and Craig (2006) this study applies a horizontal grid of  $64 \times 64$  with 101 vertical levels. A timestep of 5 s is chosen in the control simulations in order to balance the need for computational efficiency against the model’s numerical stability criteria constraints. Rotation is neglected and no mean wind or wind shear is imposed in the simulations. A horizontal resolution of 2 km with 200 m grid spacing in the vertical is applied in the set of control simulations. An overview of the control simulation parameters can be obtained from Table 2.1.

Domain size	$128 \times 128 \times 20 \text{ km}^3$
Horizontal grid spacing	2 km
Vertical grid spacing	200 m
Model grid	$64 \times 64 \times 101$
Timestep	5 s
Sea surface temperature	300 K
Mean wind/wind shear	None
Coriolis parameter	Zero
Boundary conditions	Periodic in x and y direction Fixed lid at 20 km
Newtonian damping layer	$z_D = 16.75 \text{ km}$ $\tau_{damp} = 1000 \text{ s}$
Initial/Environmental Profile	Mean sounding from the west indies (Jordan, 1958)

**Table 2.1:** Summary of the setup of the control simulations at 2 km horizontal resolution.

# Chapter 3

## Control simulations

The objective of this study is to validate a theoretical model that predicts the convective variability within a cumulus cloud ensemble in high-resolution simulations. In the first part of this study, results of Cohen and Craig (2006) (hereinafter CC06) are reproduced with the anelastic, non-hydrostatic fluid solver EULAG described in Chapter 2. The set of control simulations employs a horizontal resolution of 2 km and sensitivity of results to the magnitude of the prescribed radiative forcing is evaluated. Radiative cooling rates ranging from -2 K/day (a value often used to simulate the tropical atmosphere) to -12 K/day, with steps of -4 K/day, -6 K/day and -8 K/day are applied. In contrast to CC06, no simulation with a prescribed forcing of -16 K/day is included in this study due to the development of an unrealistically moist layer in the simulated upper troposphere. This chapter gives an overview of the 2 km control simulation results and illustrates similarities and differences in comparison to the findings of CC06 where possible.

### 3.1 Evolution to radiative-convective equilibrium

Each of the five control simulations is started from a horizontally homogeneous state with no convection, employing Jordan's mean sounding over the west indian ocean (Jordan, 1958) as initial and environmental model state. A small perturbation to the vertical velocity field is added in order to break the symmetry of the horizontally homogeneous model state and hence, facilitate the development of convective cumulus clouds. Each simulation is integrated to a state of radiative-convective equilibrium, which requires between 30 and 40 simulated days, depending on the magnitude of the prescribed forcing. The development of the simulated model state to radiative-convective equilibrium is illustrated in the following figures. The evolution of domain averaged potential temperature (left) and column integrated moisture content (right) for the 2 km control simulations is illustrated in Figure 3.1. Figure 3.2 (left) depicts the development of the domain maximum vertical velocity to the radiative-convective equilibrium state. Different colours denote different magnitudes of the prescribed radiative forcing. In line with the findings of Cohen (2001) and Tompkins and Craig (1998b) different scales of variability are observed in these figures. First, a

high-frequency signal with a timescale of about one hour is apparent in the evolution of all model variables with time. This time scale can directly be related to the life cycle of the single clouds in the equilibrium convective ensemble. Second, a long, slow trend illustrates the overall evolution of the simulated atmosphere to equilibrium with a timescale between 30 and 40 days. After this integration time a state of radiative-convective equilibrium is reached for all model variables.

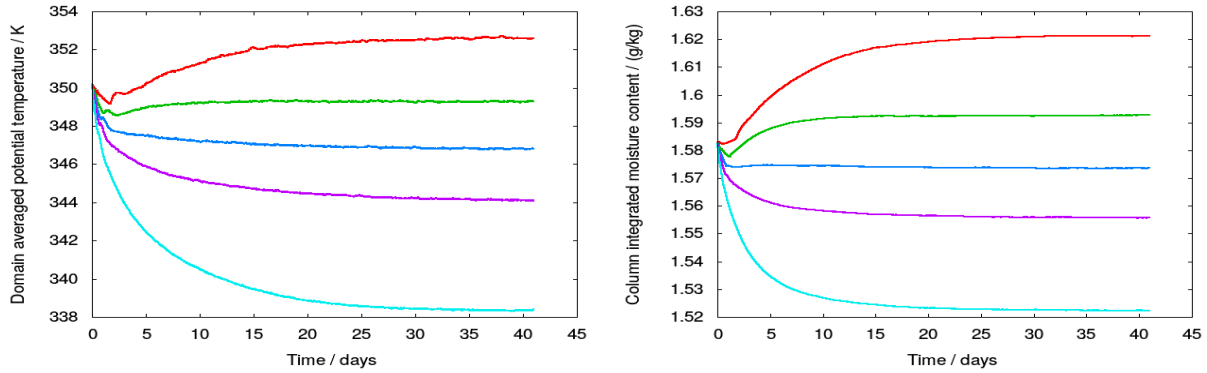


**Figure 3.1:** Timeseries of domain-averaged potential temperature (left) and column integrated moisture content (right) for -2 K/day (red), -4 K/day (green), -6 K/day (blue), -8 K/day (purple) and -12 K/day (light blue) control simulations.

Due to the complexity of the convective system the approach to radiative-convective equilibrium is observed on different timescales for different model variables. A long timescale is apparent in the domain averaged potential and absolute temperature (not shown), column integrated moisture content and domain maximum precipitation rate (not shown). In contrast, a high-frequency signal is the more dominant feature in Figure 3.2 (left) illustrating the evolution of domain maximum vertical velocity for radiative forcings of -4 K/day (green) and -12 K/day (blue) and the evolution of this quantity to an equilibrium state is significantly shorter. An equivalent short time scale is observed in timeseries of the domain total precipitation rate (Figure 3.2 right) and surface fluxes of sensible and latent heat (Figure 3.3). Regarding differences in the simulated equilibrium states, it is observed in Figure 3.1 that the state of the simulated atmosphere evolves to be drier and cooler with increasing magnitude of the prescribed radiative cooling. Domain maximum vertical velocity increases with increasing forcing and a comparable systematic shift to larger values is observed for surface fluxes of latent and sensible heat (Figure 3.3). Fluctuations of the vertical velocity around its arithmetic mean also increase with increasing forcing as illustrated in Figure 3.2 (left) for -4 K/day (green) and -12 K/day (blue) control simulations. The opposite is observed in Figure 3.2 (right) illustrating the evolution of the domain total precipitation rate for the -4 K/day and -12 K/day simulations. Absolute values of the domain total precipitation rate and their fluctuations decrease slightly as radiative cooling increases. This is consistent with the drying of the atmospheric conditions observed in Figure 3.1 (right).

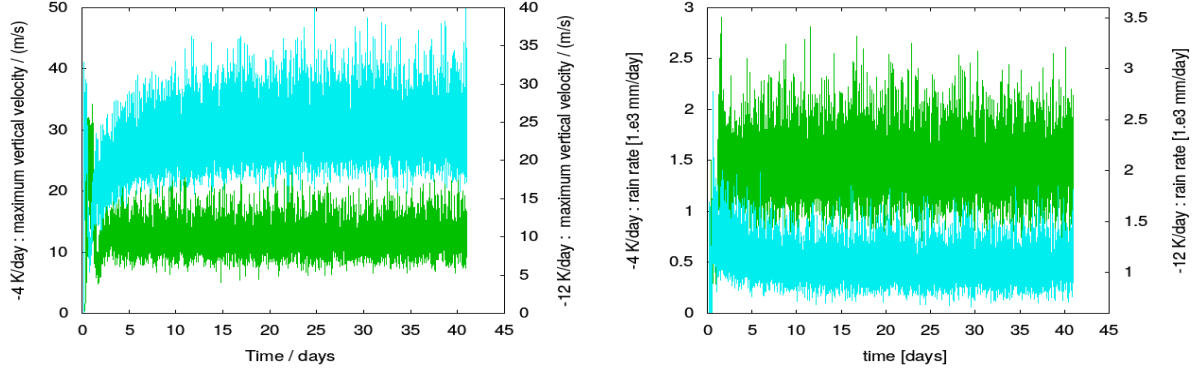


**Figure 3.2:** Timeseries of domain maximum vertical velocity (left) and precipitation rate (right) for -4 K/day (green) and -12 K/day (blue) simulations.

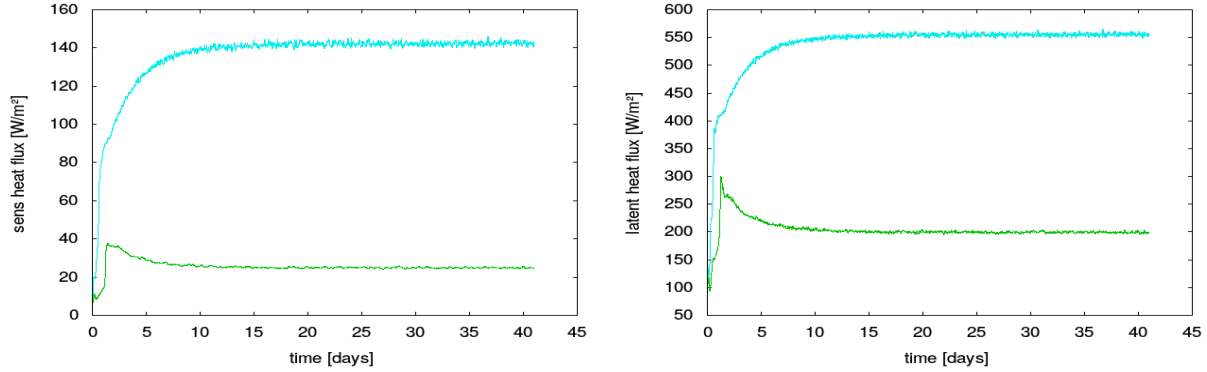


**Figure 3.3:** Timeseries of the sensible (left) and latent heat flux (right) for -4 K/day (green) and -12 K/day (blue) simulations.

Once a radiative-convective equilibrium state is reached, the input of energy by surface fluxes of latent and sensible heat provides exactly the amount of energy required to drive the convective ensemble that compensates for the radiative cooling via the appropriate amount of subsidence warming (Cohen, 2001). The amount of energy removed from the simulated atmosphere by the prescribed radiative cooling can be computed following Equation (3.1) where  $\dot{T}dz$  denotes the change of total temperature with time,  $c_p$  is the heat capacity and  $\rho$  the density of air.

$$Q_{Rad} = \int_0^{z_t} \rho \cdot c_p \cdot \dot{T} \cdot dz \quad (3.1)$$

Each of the control simulations is started from the same horizontally homogeneous state with no convection. A strong convective outbreak occurs during the first simulated day

(Figure 3.2 and 3.3). Surface fluxes of sensible and latent heat gradually increase as the domain total temperature of the atmosphere decreases due to the radiative cooling  $Q_{Rad}$  (Figure 3.3). This increase of the energy input in the boundary layer interacting with the tropospheric radiative cooling facilitates the evolution of a convective cumulus cloud ensemble in the domain, with the resulting subsidence warming and moistening effects balancing the moisture and energy budget. Within the equilibrium state, the ratio between sensible and latent heat fluxes, the so-called Bowen ratio is found to be approximately 0.19 for a radiative cooling of -8 K/day. This is consistent with observations and results of previous numerical simulations (e.g. 0.18 in the -8 K/day simulation by Cohen (2001)).

## 3.2 The simulated equilibrium state

### 3.2.1 Equilibrium vertical profiles

Despite the complexity of simulating convective processes in the atmosphere, a balanced state is achieved in the numerical simulations after an integration time of 30 to 40 days. For each magnitude of the prescribed forcing, an equilibrium state is reached where the convective heating in the subsiding air in the cloud-free area (subsidence warming), balances the energy extracted from the system by the prescribed radiative cooling. Hence, an increase in the forcing is expected to result in an increase of the convective activity in the domain. In addition, as pointed out in Cohen (2001) and commonly known as *le Chatelier's principle*, one expects a systematic shift of the vertical profiles in the equilibrium state in the direction of the forcing, meaning the atmosphere evolving correspondingly drier and cooler for stronger cooling rates.

### Thermodynamic variables

Differences of the simulated equilibrium states in the 2 km control simulations are evaluated by comparing vertical profiles of horizontally averaged atmospheric properties. Figure 3.4 illustrates vertical profiles of potential temperature (left) and moist static energy (right). Averages are computed over the horizontal extend of the domain and for one day within the equilibrium state, using 15 minute data. Moist static energy (mse) is commonly defined as  $mse = c_p \cdot T + g \cdot z + L_v \cdot q$  and denotes the total energy of an air parcel, including adiabatic heating, potential energy and moisture effects, but neglecting kinetic energy. This quantity is generally assumed to be conserved in saturated air and its form is similar to the equivalent potential temperature. It hence gives an overview over the combined effects of cooling and drying in these simulations. The vertical profile of moist static energy (Figure 3.4 right) first exhibits a decrease of values followed by very slowly increasing values up to the height of the tropopause. Changes in the moist static energy profiles with forcing are significant, exhibiting smaller values for larger magnitudes of the prescribed forcing.



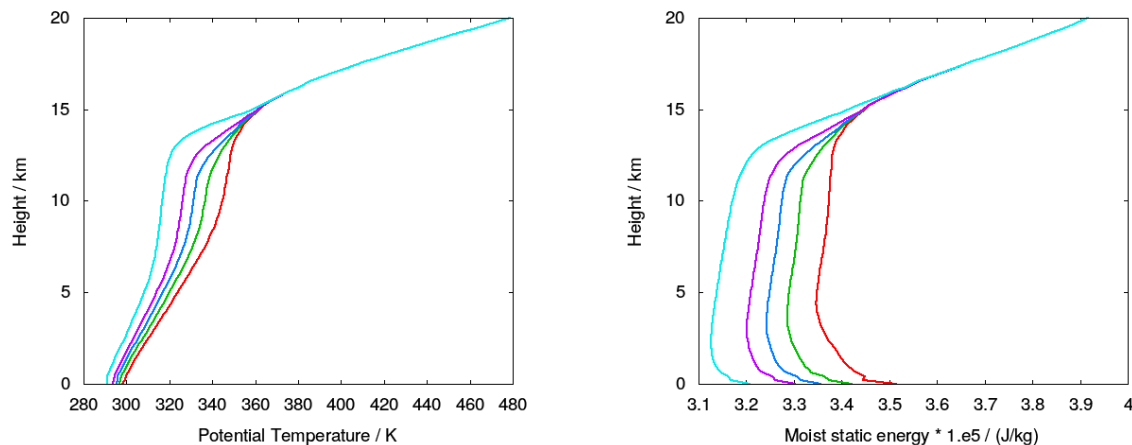


**Figure 3.4:** Vertical profiles of horizontally averaged potential temperature (left) and moist static energy (right) for the 2 km control simulations. Different colours denote cooling rates of -2 K/day (red), -4 K/day (green), -6 K/day (blue), -8 K/day (purple) and -12 K/day (light blue).

This systematic decrease is in line with the decreasing domain-averaged temperature (Figure 3.1) with stronger forcing as well as the drier equilibrium states, in terms of absolute moisture content as well as relative humidity (not shown). A minimum in the moist static energy profile is obtained from this figure, its position increasing in height with decreasing magnitude of the prescribed forcing. This minimum is in line with the findings of CC06. They observed a minimum of moist static energy at a height of 2 km in their -8 K/day simulations which they explained to be owed to the boundary between the shallow cumulus and the upper deep convective layer.

As already expected from analysing the evolution to radiative-convective equilibrium in Figure 3.1 (left and right), the vertical profiles of potential temperature (Figure 3.4 left) exhibit a systematic shift to cooler temperatures with increasing magnitude of the prescribed forcing. Throughout the lowest 600 m the potential temperature values are almost constant, especially in the stronger forced simulations (-8 K/day and -12 K/day) and then increase throughout the troposphere. Values of the potential temperature being approximately constant between the surface and a height of 600 m indicates a well-mixed boundary layer. However, Figure 3.4 (left) shows the boundary layer not being as nicely developed for the weaker forced simulations (-2 K/day and -4 K/day) as for the stronger forced ones. This is most likely caused by under-resolved turbulent eddies limited by the vertical resolution of 200 m in combination with smaller surface fluxes in the weaker forced simulations.

### Convective variables

Convective transport of heat and moisture and the resulting subsidence warming balances the energy loss caused by the imposed radiative cooling. To quantify the amount of up- and downward transport, vertical mass flux is computed for the up- and downward motions. A

grid point is considered to be part of an up- or downdraft based upon a vertical velocity criterium ( $w > 1 \text{ m/s}$ ,  $w < -1 \text{ m/s}$ ). This threshold definition has been conventionally used in preceding studies (LeMone and Zipser, 1980; Cohen, 2001) and has proven itself by excluding weaker gravity wave motions occurring between the convective cumulus clouds. Sensitivity of results to the definition of a cloudy grid point was evaluated in Cohen (2001) and little sensitivity was found. Figure 3.5 (left) illustrates vertical profiles of the up- and downdraft mass flux in the domain. The fractional area of the domain covered by convective updrafts, hereinafter called “convective fraction”, is depicted in Figure 3.5 (right). A systematic increase of both quantities with increasing magnitude of the forcing is observed, which compares well to the results of CC06. Deep convection is observed to reach a maximum height of approximately 12 km.

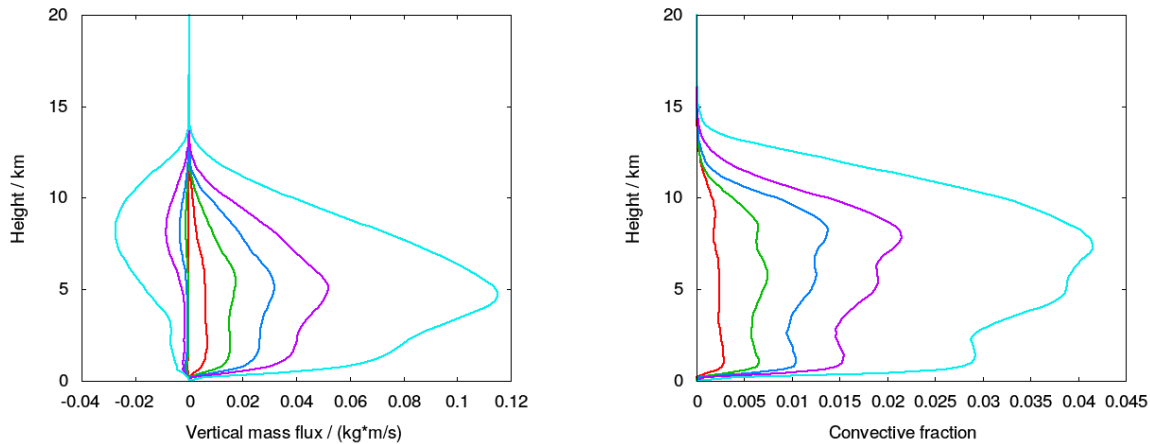


**Figure 3.5:** Profiles of upward and downward mass flux (left) and the fractional area of the domain covered by convective updrafts (right). Different colours denote radiative cooling rates of -2 K/day (red), -4 K/day (green), -6 K/day (blue), -8 K/day (purple) and -12 K/day (light blue).

A bimodal structure is visible in the upward mass flux profiles. This structure results from the coexistence of shallow and deep convective regimes and is even more apparent in the vertical profiles of the convective fraction with a shallow convective peak at a height of 1.5 km. Regarding the fractional area of the domain covered by convection, Figure 3.5 (right) even illustrates signs of a trimodal structure. The existence of this third mode has previously been noted by Johnson et al. (1999). This mode is owed to cumulus congestus attributing to the development of a stable layer at the freezing level due to re-evaporation of detrained ice from organised systems. Profiles agree well with previous studies (Cohen, 2001) and observations (BOMEX (Nitta, 1975)), however, some differences are apparent. First, the local maxima in the up- and downward mass fluxes associated with the shallow convective layer observed at a height of 1 km in CC06, are significantly weaker in this study. This is consistent with the underresolved boundary layer structure (Figure 3.4). Second, signs of a trimodal structure seen in the convective fraction profiles (Figure 3.5 right) have not been observed in CC06. In order to quantify this systematic increase of upward mass

flux, its dependence on the magnitude of the prescribed forcing is further evaluated in the next paragraph.

### 3.2.2 Response to changes in the forcing

In a state of radiative-convective equilibrium, the energy loss resulting from the large-scale radiative cooling has to be balanced by subsidence warming occurring around and between the convective clouds. Hence, the upward mass flux is expected and has been observed in earlier studies to be proportional to the magnitude of the prescribed radiative cooling (Robe and Emanuel, 1996; Shutts and Gray, 1999; Cohen, 2001). The relation between the upward mass flux and the radiative forcing can be illustrated in terms of the prescribed radiative cooling  $Q_{rad}$ , the subsidence vertical velocity  $w_{sub}$  and the potential temperature lapse rate  $d\theta/dz$ . The amount of subsidence warming is constrained by the magnitude of the prescribed forcing, the stability of the atmosphere and mass continuity. Equation (3.2) describes the relationship between the prescribed cooling rate and the potential temperature lapse rate.

$$w_{sub} \cdot \frac{d\theta}{dz} = Q_{rad} \quad (3.2)$$

In contrast to Cohen (2001), where all potential temperature profiles were found to be close to a moist adiabat, different slopes of the temperature profiles in Figure 3.4 (left) suggest a change of the tropospheric potential temperature lapse rate with increasing forcing. An overview of the potential temperature lapse rates  $d\theta/dz$  for the different prescribed radiative forcings  $Q_{rad}$  is given in Table 3.1.

$Q_{rad}$	[K/day]	-2	-4	-6	-8	-12
$d\theta/dz$	[K/km]	4.3	3.7	3.3	3.0	2.4
$Q_{Eff-rad}$	[K/day]	-1.6	-3.6	-6.1	-8.9	-16.7

**Table 3.1:** Potential temperature lapse rate in the convective region for the 2 km control simulations. Effective forcing  $Q_{Eff-rad}$  considers stability differences between the weaker and stronger forced simulations.

A general decrease of potential temperature lapse rate with increasing magnitude of the prescribed forcing is apparent in this table. This decrease and the general change of shape obtained from the potential temperature profiles (Figure 3.4 left) suggest increasing deviations of the atmospheric conditions from a moist adiabat. Changes in the atmospheric stability conditions are known to influence properties of the convecting atmosphere like the amount of subsidence warming in the cloud-free environment. Simulations with a cooling of -2 K/day (red) and -4 K/day (green) exhibit a temperature lapse rate quite close to a moist adiabat, whereas the stronger forced simulations illustrate a lapse rate larger than

the associated moist adiabats (not shown). It is therefore necessary to consider these stability changes and their influence on the convective ensemble.

Taking into account the relationship between the potential temperature lapse rate and the radiative forcing, one can derive an *effective* radiative forcing that considers the observed stability differences between the simulated atmospheric states and is directly connected to the amount of subsidence warming in the model domain. The effective forcing  $Q_{Eff-rad}$  is computed for each prescribed forcing  $Q_{rad}$  as described in Equation (3.3), where  $d\theta/dz$  denotes the potential temperature lapse rate averaged over all 2 km resolution control simulations.

$$Q_{Eff-rad} = Q_{rad} \cdot (\overline{d\theta/dz}) / (d\theta/dz) \quad (3.3)$$

As noted above, a systematic increase of vertical mass flux and convective fraction with increasing radiative cooling is obtained in Figure 3.5. This systematic increase and the fact that it is not entirely uniform with height, agrees well with the findings of preceding studies. In contrast to the systematic shift of potential temperature observed in the simulations, Cohen (2001) expected changes to the smaller-scale details of the convective system as a function of the forcing to be quite complicated and hard to predict. However, they found the response of upward mass flux to changes in the magnitude of the prescribed forcing to be approximately linear in their study.

To evaluate this relation in the 2 km control simulations, upward mass flux is replotted as a function of forcing in Figure 3.6 (left). Two different sets of points are depicted in this figure. Blue x's denote the upward mass flux as function of the prescribed radiative forcing  $Q_{rad}$ , whereas black boxes illustrate upward mass flux as function of the effective forcing  $Q_{eff-rad}$  as denoted in Equation (3.3).

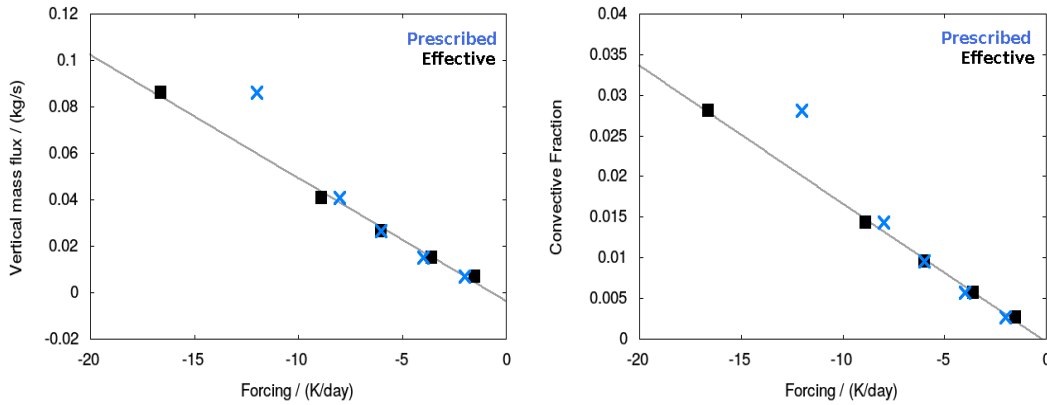


**Figure 3.6:** Domain vertical mass flux (left) and convective fraction (right) at 2.4 km height replotted as function of the prescribed radiative forcing (blue) and the effective radiative forcing  $Q_{Eff-rad}$  (black). Grey solid lines denote least squares best fits to the equilibrium data scaling with  $Q_{rad}$ .

Figure 3.6 (right) illustrates the relationship between the fractional area of the domain covered by convection, the prescribed (blue) and the effective radiative forcing (black) analogously. It is clear from this figure that both quantities scale linearly with the effective forcing  $Q_{Eff-rad}$ , whereas a curved relationship is obtained when plotting upward mass flux and cloud fraction against the prescribed radiative forcing  $Q_{rad}$ . This curvature is in line with the observed stability changes motivating the computation of an effective forcing, taking into account the relationship between subsidence warming and the radiative forcing. In contrast, CC06 obtained an approximately linear relation between domain upward mass flux, cloud fraction and the prescribed radiative forcing. However, a small tendency towards a curvature is apparent in their results as well. Due to the fact that upward mass flux is directly connected to the amount of subsidence warming in the convective atmosphere, the effective forcing  $Q_{eff-rad}$  is applied in further analysis of the relationship between the convective ensemble and the magnitude of the prescribed forcing in this chapter.

### 3.2.3 Cloud field structure

An evaluation of vertical profiles and domain averaged upward mass flux cannot provide a complete understanding of the processes in the equilibrium convective cloud ensemble. Especially the effect of an increase of the prescribed cooling on the structure and properties of the cloud field is of great interest. Figure 3.7 exhibits vertical cross-sections of the vertical velocity field in radiative-convective equilibrium for prescribed cooling rates of -4 K/day (left) and -12 K/day (right). Several updrafts are illustrated in this figure (yellow/white) varying in their maximum height and width. The associated downdraft areas are illustrated in dark red.

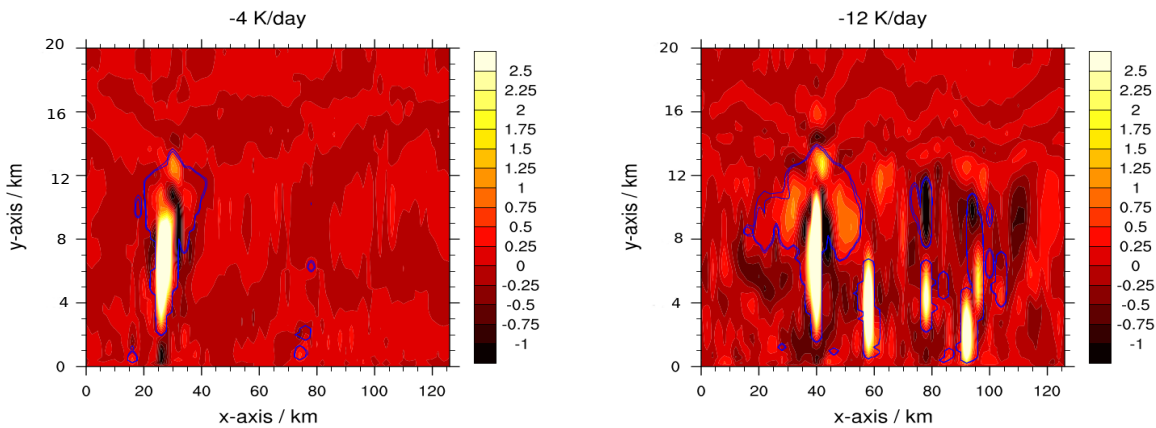


**Figure 3.7:** Vertical cross-sections of the vertical velocity field (m/s) for the -4 K/day (left) and -12 K/day (right) simulation. Contours denote presence of condensed cloud water (g/kg).

For both forcings a deep convective cloud rises to a height of approximately 12 km and blue contours of condensed cloud water mixing ratio suggest the formation of anvil clouds at this height. This is in line with the height level that convective fraction and upward mass flux profiles suggest to be the detrainment level. In the -12 K/day simulation (right) several small updrafts are apparent as well. Comparing the number of updrafts and their shape for the -4 K/day and -12 K/day simulation, the number of updrafts is found to increase with increasing forcing. The general shape of the convective updrafts and downdrafts is to be comparable though.

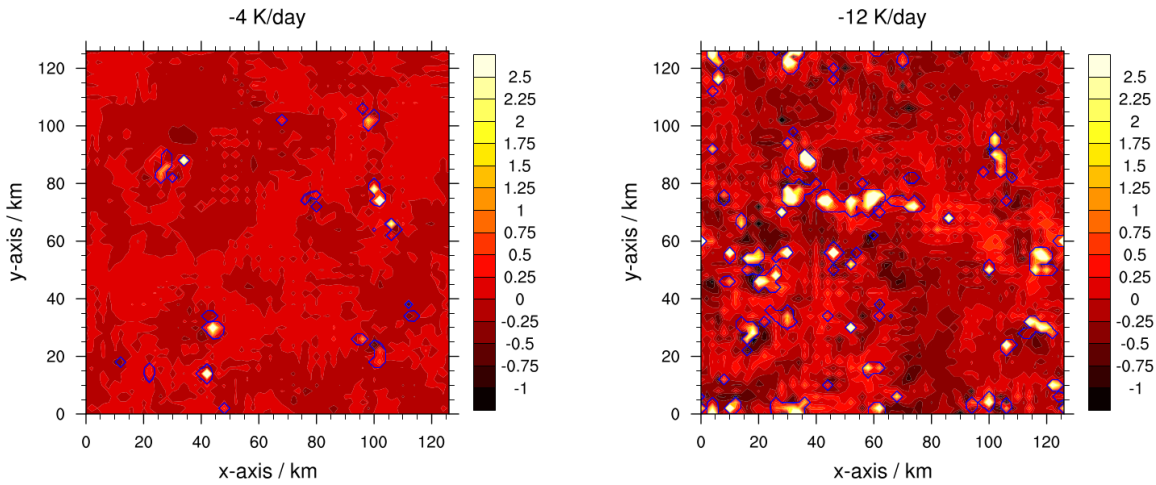


**Figure 3.8:** Horizontal cross-sections through the vertical velocity field (m/s) of -4 K/day (left) and -12 K/day (right) simulations. Contours denote presence of condensed cloud water (g/kg).

Figure 3.8 exhibits horizontal cross-sections through the vertical velocity field at a height of 2.4 km for the -4 K/day (left) and -12 K/day (right) simulation. Updraft (yellow/white) and downdraft cores (dark red) are apparent in this figure and blue contours denote the presence of condensed cloud water analogously to Figure 3.7. Convective clouds are found to be randomly distributed throughout the domain at both forcings. Cloud number increases significantly with increasing magnitude of the forcing and a comparison of weakly and strongly forced cloud fields exhibits slightly larger cloud sizes in the stronger forced simulations. These changes observed with increasing magnitude of the prescribed forcing are further evaluated statistically in the next section.

### 3.3 Statistics of the equilibrium convective ensemble

In order to quantify the fluctuations within the simulated cloud ensembles in their radiative-convective equilibrium state, individual cloud statistics are computed. Results are compared to the theoretical model on equilibrium ensemble statistics derived in Craig and Cohen (2006) and to numerical simulation results from Cohen and Craig (2006). To facilitate a comparison with these studies the same method of identifying the convective updrafts in the domain is applied. This method employs a search algorithm that scans horizontal cross-sections of the vertical velocity and cloud water mixing ratio fields for cloudy grid points and adjacent cloudy grid points in a computationally efficient way (Hoshen and Kopelman, 1976; Dahl, 2010). Grid points are defined to be cloudy if their vertical velocity exceeds a threshold of 1 m/s and the condensed cloud water content is non-zero. The algorithm identifies directly connected cloudy grid points (four-connectivity) to be associated with the same cloud. Mean updraft velocity  $\overline{w}_i$  and the area occupied by each cloud ( $\sigma_i$ ) are computed after identifying all cloudy updrafts in the domain. Sensitivity of the equilibrium statistics to the definition of a cloudy grid point was evaluated in Cohen (2001). They compared results applying merely a threshold of condensed water versus a combination of vertical velocity and cloud water thresholds, and found both definitions to produce comparable results. Both cloud definitions were capable of reproducing the theoretical Boltzmann distribution of cloud vertical mass flux in their study (Cohen, 2001).

#### 3.3.1 Sensitivity to the large-scale forcing

Evaluation of upward mass flux and convective fraction profiles in section 3.2.1 has revealed a systematic increase with increasing strength of the forcing. In addition, cross sections of the cloud fields for different forcings suggest a significant increase of the number of clouds and a small increase of cloud size. To further evaluate this sensitivity Figure 3.9 illustrates the relation between the magnitude of the forcing, the mean number of clouds observed in the domain (left) and the average area occupied by the clouds (right). A strong sensitivity of the number of clouds on the magnitude of the forcing is apparent in this figure. Mean cloud numbers scale linearly with the forcing for all cooling rates. Average cloud numbers range from 8 clouds in the -2 K/day to 56 clouds in the -12 K/day domains. These numbers and the linear scaling compare well with results from CC06. Sensitivity of cloud size to the magnitude of the forcing is significantly weaker. Mean cloud areas range from 5 km<sup>2</sup> to 8 km<sup>2</sup>, increasing slightly with stronger cooling rates. Similar cloud sizes were observed in CC06. In terms of grid points, clouds in the equilibrium convective ensemble are found to encompass merely one or two grid boxes on average. The size of the convective updrafts being strongly limited by the grid scale further motivates the evaluation of the resolution dependence of cumulus cloud statistics.

In addition to cloud number and cloud size, the relation of the in-cloud vertical velocity to the magnitude of the forcing is illustrated in Figure 3.10. As expected from earlier studies (Robe and Emanuel, 1996; Shutts and Gray, 1999; Cohen, 2001) this cloud property exhibits a rather weak dependence on the strength of the radiative cooling. In-cloud

vertical velocity increases from 2.9 m/s to 3.3 m/s as the magnitude of the radiative cooling increases by a factor of six from -2 K/day to -12 K/day. This weak dependence of updraft velocity on the magnitude of the forcing agrees well with results of CC06. Hence, most of the increase in upward mass flux obtained in Figure 3.6 (left), is owed to the increase in cloud number, and therefore in the fractional area of the domain occupied by convection. However, the intensity of the individual clouds in the 2 km simulations is not significantly affected by changes in the magnitude of the forcing.

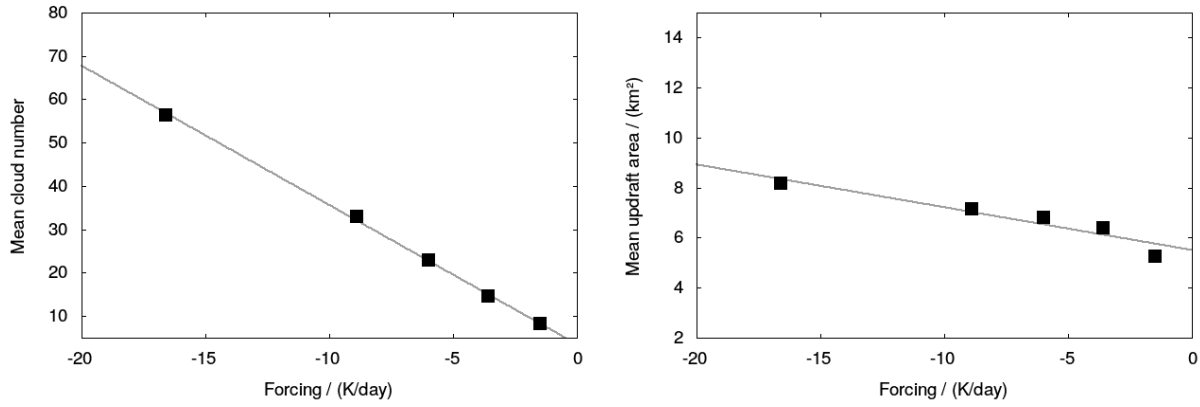


**Figure 3.9:** Influence of the magnitude of the effective forcing ( $Q_{Eff-rad}$ ) on the number of clouds in the domain (left) and average area occupied by convective updrafts (right) at 2.4 km height.

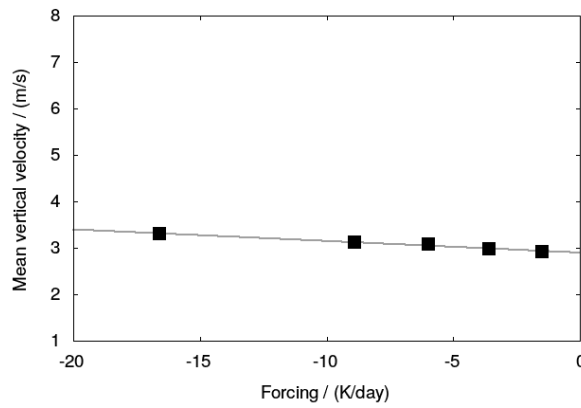


**Figure 3.10:** Influence of the magnitude of the effective forcing ( $Q_{Eff-rad}$ ) on the mean convective updraft velocity at 2.4 km height.



### 3.3.2 Convective variability in statistical equilibrium

Assuming that the forcing of convection does not vary significantly over a specific region and that clouds are sufficiently separated to justify neglecting interactions between neighbouring cells, CC06 derived the vertical cloud mass flux to be distributed exponentially as denoted in Chapter 1, Equation (1.1). To validate this theory, 15-minute data over a period of ten days within the radiative-convective equilibrium state is taken into account. The search algorithm described above is applied at a height of 2.4 km, thereby excluding shallow convection from the cloud ensemble statistics.

#### Cloud mass flux

The theoretical distribution derived in CC06 is validated on the basis of cloud mass flux frequency distributions in the equilibrium state for the 2 km resolution control simulations. For each convective updraft, cloud mass flux  $m_i$  is defined as denoted in Equation (3.4).

$$m_i = \rho \cdot \sigma_i \cdot \overline{w}_i \quad (3.4)$$

In this equation, the variable  $\rho$  denotes the density of air,  $\sigma_i$  gives the area occupied by, and  $\overline{w}_i$  the average vertical velocity within a convective cloud. Clouds are identified by the search algorithm described in section 3.3 and their vertical mass flux is computed over a period of ten consecutive days in the equilibrium state. Figure 3.11 illustrates the frequency distribution of cloud mass flux in the -4 K/day (left) and the -12 K/day (right) control simulations. A bin width of  $4 \cdot 10^6$  kg/s is employed.

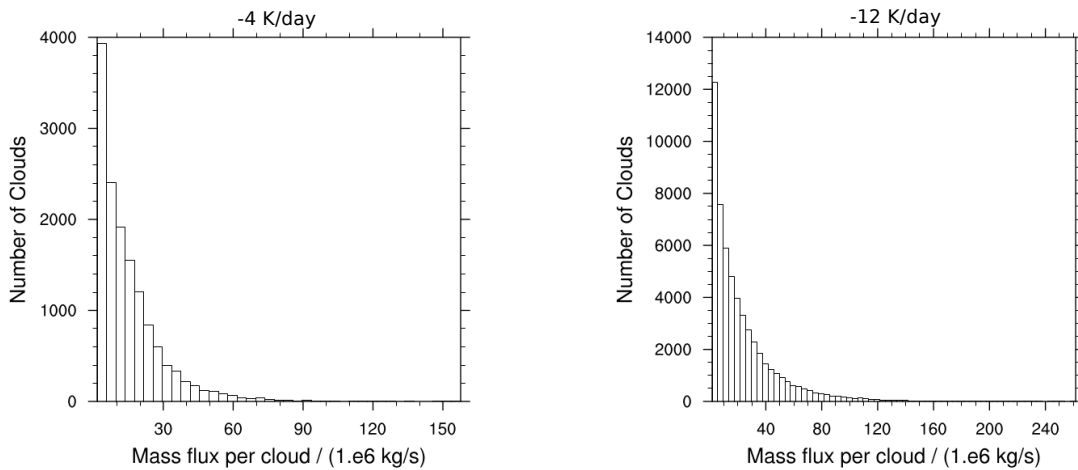


**Figure 3.11:** Histograms of cloud mass flux for the 2 km control simulations at a prescribed forcing of -4 K/day (left) and -12 K/day (right).

Comparing the distributions, a strong increase of the total number of clouds with increasing forcing is observed whereas the general shape of the distribution is not significantly influenced. However, it is evident that the distribution is wider in the higher forced simulations. Values of cloud mass flux  $m_i$  up to  $1.3 \cdot 10^8$  kg/s are observed in the -12 K/day simulations, whereas maximum values of  $0.8 \cdot 10^8$  kg/s are obtained in the -4 K/day run. This observed widening of the distribution raises the question what effect an increase in cooling generally has on the ensemble mean cloud vertical mass flux. Figure 3.12 illustrates the relationship between cloud mass flux and the magnitude of the effective forcing  $Q_{eff-rad}$ . An approximately linear increase of cloud mass flux with increasing strength of the forcing is illustrated in this figure. Values increase from  $1.4 \cdot 10^7$  kg/s in the -2 K/day to  $2.5 \cdot 10^7$  kg/s in the -12 K/day simulation. This increase is accumulated from the small increase of incloud vertical velocity and a slightly more significant increase of cloud sizes as illustrated in Figure 3.9 (right) and Figure 3.10. Deviations of the average cloud mass flux from the linear fit are larger than for cloud size in Figure 3.9, due to the influence of cloud vertical velocity. The increase of cloud mass flux with forcing in this figure, is in agreement with the widening of the distribution illustrated in Figure 3.11.

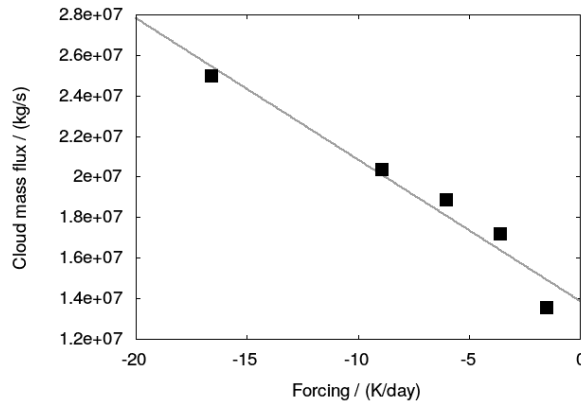


**Figure 3.12:** Influence of the magnitude of the effective forcing ( $Q_{Eff-rad}$ ) on cloud vertical mass flux at 2.4 km height. Grey line denotes the least squares best fit to the data points.

Focusing on the shape of the cloud mass flux distributions in Figure 3.11, both histograms suggest an exponential distribution. In order to evaluate whether these distributions are indeed exponential and to facilitate a comparison with the theoretical distribution, Figure 3.11 is replotted with a logarithmic scaling of the y-axis (Figure 3.13). The theoretical prediction of cloud mass flux (CC06) is denoted by the blue line and corresponds to a maximum entropy fit. A linear least squares best fit to the data is illustrated by the red line.

Figure 3.13 clearly shows that both distributions nicely resemble the expected exponential distribution. The least squares and the maximum entropy fits are almost identical in the -4 K/day simulation (Figure 3.13 left). For the -12 K/day simulation (right) some clouds

exhibit slightly larger mass fluxes than denoted by the maximum entropy fit. However, the least squares best fit being more sensitive to large values, still poses an adequate fit to the distribution.

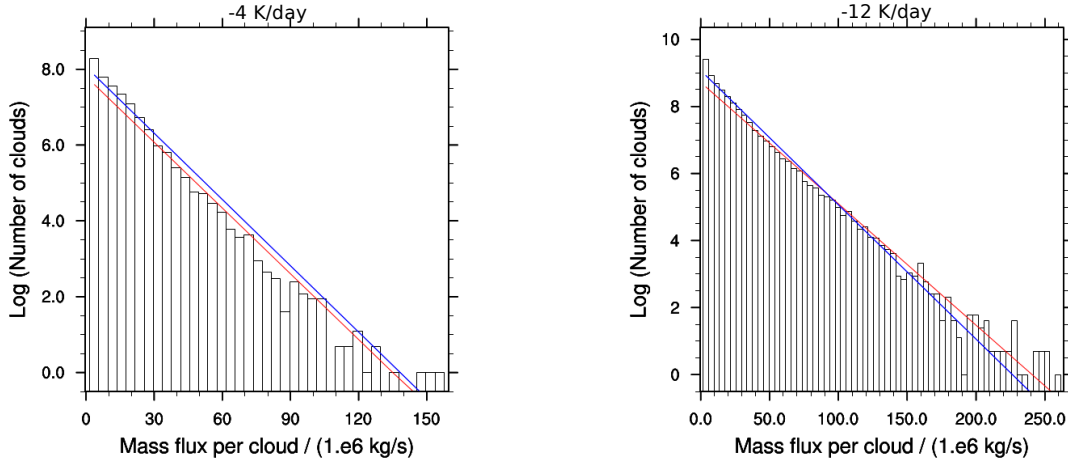


**Figure 3.13:** Same as Figure 3.11 but with logarithmic scaling of the y-axis. Least squares best fit denoted by the red and maximum entropy fit by the blue line.

From Equation (1.1) it can be derived that the slope of the least squares fit (red) in Figure 3.13 relates to the ensemble mean mass flux per cloud  $\langle m \rangle$  and its intercept with the y-axis denotes the average number of clouds in the domain  $\langle N \rangle$ . Table 3.2 gives an overview of  $\langle m \rangle$  and  $\langle N \rangle$  obtained from the cloud-search-algorithm and derived from the least squares best fit (red) of form  $\ln(y) = \ln(a) - x/b$  denoted in Figure 3.13.

$Q_{rad}$	-4 K/day		-12 K/day	
	Model data	Best fit (least squares)	Model data	Best fit (least squares)
$\langle m \rangle$	$1.72 \cdot 10^7$	$1.73 \cdot 10^7$	$2.49 \cdot 10^7$	$2.76 \cdot 10^7$
$\langle N \rangle$	14.6	11.0	56.5	43.5

**Table 3.2:** Values of ensemble average cloud mass flux  $\langle m \rangle$  and ensemble average cloud number  $\langle N \rangle$  diagnosed from the model data and derived from the least squares best fit in Figure 3.13.

This table shows that values of  $\langle m \rangle$  and  $\langle N \rangle$  derived from the model data and the least squares best fit agree nicely for the -4 K/day simulation. Comparably good agreement of  $\langle m \rangle$  and  $\langle N \rangle$  is obtained for the -2 K/day simulation (not shown). Hence, one can conclude that the theory succeeds in predicting the distribution of the cloud properties in weakly forced simulations. In contrast, differences are apparent when comparing  $\langle m \rangle$  and  $\langle N \rangle$

for the -12 K/day simulation. The average cloud mass flux computed from the simulated cloud data is found to be smaller than the value derived from the least squares best fit, whereas the observed number of clouds in the domain is found to be larger than the estimate from the best fit (red). In general, a least squares best fit (red) is more sensitive to large *outliers* of the distribution than a maximum entropy fit (blue). Hence, clouds with a large vertical mass flux contribute more to the least squares best fit leading to increasing differences between the simulated cloud data and the least squares best fit. It is of great interest to analyse whether the tendency towards clouds with larger vertical mass fluxes with increased forcing is sensitive to the grid spacing and to evaluate whether the changes observed are owed to an increase in cloud size or updraft velocity.

### Cloud size and vertical velocity

Regarding the observed trend of larger cloud vertical mass fluxes with increasing forcing, it is of great interest what cloud properties these differences are owed to. Equation (3.4) depicts cloud mass flux to be a product of cloud density, cloud size and the average updraft velocity. Therefore, distributions of cloud size and vertical velocity observed in the equilibrium state are evaluated hereinafter to adress this issue.

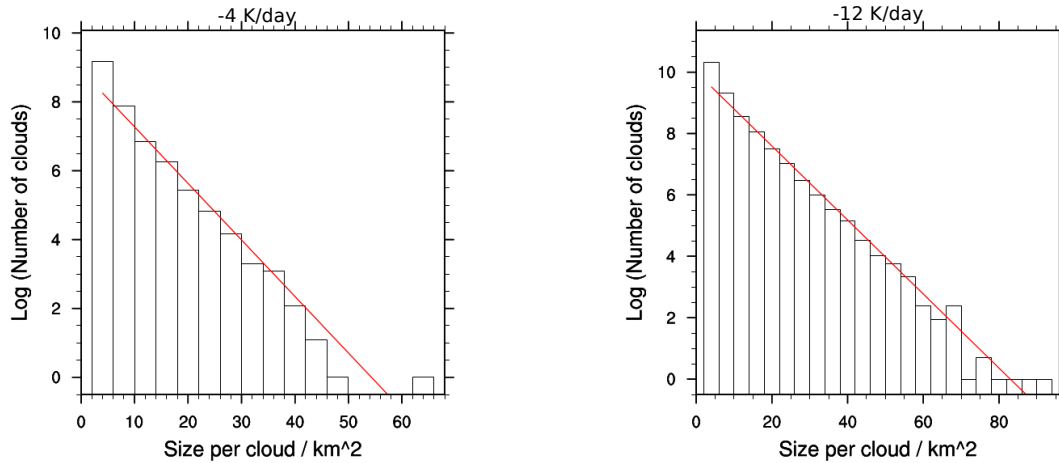


**Figure 3.14:** Distribution of cloud size for -4 K/day (left) and -12 K/day (right) control simulations. Red lines denote least squares best fit to the distribution.

A wide range of possible expectations on the shape of the cloud size frequency distribution is given by literature, ranging from exponential to log-normal to double power law distributions as noted in Chapter 1 (Section 1.2.1). The shape most often observed in cloud size studies of shallow convection however, is a double power law distribution with a distinct scale break at a certain cloud size (Cahalan and Joseph, 1989; Neggers et al.,

2003). Lennard (2004) supports the idea of a double power law with a distinct scale break at a certain cloud size for deep convection as well and argues that observing exponential distributions may be a result of cloud sizes being limited by the grid spacing and falling on one side of the scale break. He proposes a scale break at cloud diameters of approximately 2 km. Figure 3.14 illustrates the distribution of cloud sizes for the -4 K/day and -12 K/day simulations in a log-linear environment. Indeed, the cloud size distributions in the control simulations are found to be exponential over the entire range of prescribed radiative cooling rates. In addition, with increasing strength of the cooling the distribution widens, exhibiting maximum values of  $64 \text{ km}^2$  in the -4 K/day simulation (left) and  $92 \text{ km}^2$  in the -12 K/day simulation (right). The observation of larger cloud sizes with stronger forcing can partially explain the observed increase of cloud vertical mass fluxes in Figure 3.13. However, the widening of the cloud size distributions is not significant enough to account for the entire increase. The second component contributing to cloud mass flux is the average vertical velocity within the convective updrafts.

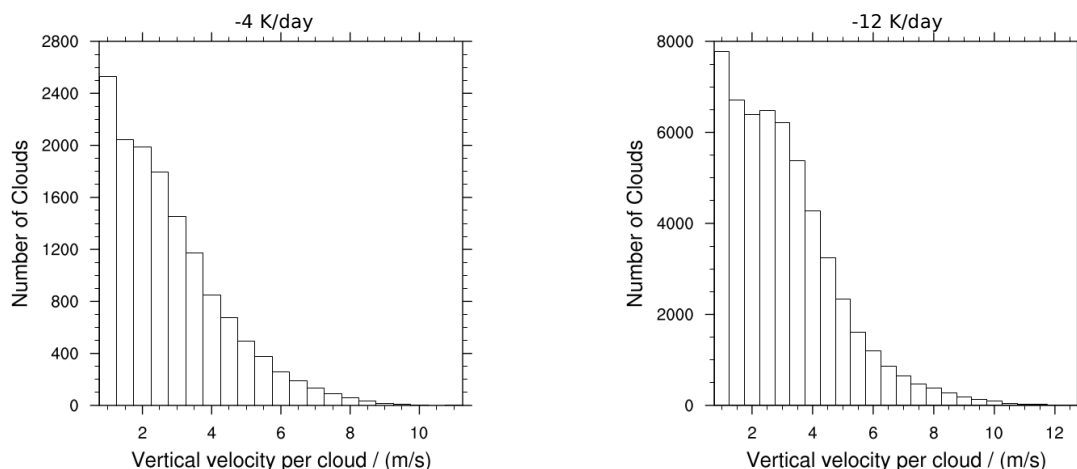


**Figure 3.15:** Distribution of vertical velocity per cloud for -4 K/day (left) and -12 K/day (right) control simulations

Figure 3.15 denotes the distribution of cloud vertical velocity for the -4 K/day (left) and -12 K/day (right) simulations. Updraft velocities in the -4 K/day simulation (left) range from 1 m/s to 9.0 m/s with a distinct maximum at 1 m/s and a high probability for velocities to fall in the range of 1 m/s to 2 m/s. For the -12 K/day simulation (right), the same maximum at 1 m/s is obtained and maximum velocities up to 11 m/s are observed. A wider peak ranging from 1.5 m/s to 3 m/s is observed and the number density of vertical velocity decreases faster than in the -4 K/day simulation. This explains the small increase of mean vertical velocity seen in Figure 3.10.

From these evaluations one can conclude that the observed changes in shape and width

of the cloud mass flux distributions (Figure 3.11 and Figure 3.13) are partially owed to a small increase of cloud sizes with increasing forcing, as well as to a change in the shape of the distribution of vertical velocity and a small but systematic increase of the vertical velocities. Regarding the robustness of the frequency distributions, sensitivity tests for the -12 K/day simulation based on data sets comprising three and ten days are conducted. Distributions are found to be comparable and insensitive to the amount of data used (not shown). We can therefore conclude, that cloud statistics are robust and changes in the shape of the distributions observed with increasing magnitude of the forcing are owed to changes in the cloud properties. Possible changes in the structure of the cloud fields with increasing forcing are evaluated in the next paragraph.

### 3.3.3 Cloud field statistics

One major assumption when deriving the theoretical distribution of cloud mass flux is the clouds to be sufficiently separated from each other and non-interacting (CC06). This assumption allows cloud position in space to be described by a random (Poisson) distribution. However, it is common knowledge from observations that a random distribution may not necessarily be valid in realistic cloud fields.

The presence of clustering or regularity in observed or simulated cloud fields can be determined by evaluating the cloud number density as a function of distance from cloud center. Mean cloud number is calculated in annular regions surrounding each cloud as denoted in the schematic in Figure 3.16. Counting clouds in the environment of a cumulus cloud, one needs to take into account that the horizontal boundary conditions in the computational domain are periodic. This is indicated by the largest annular region crossing the horizontal boundary in schematic 3.16.

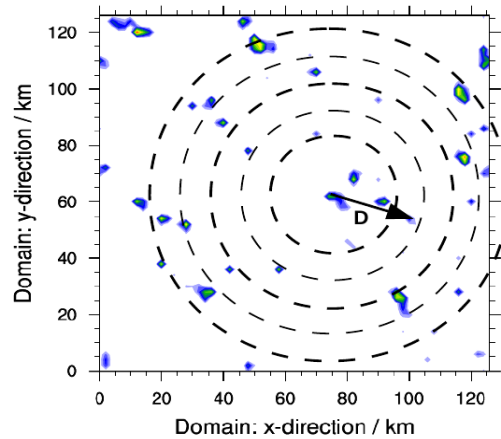


**Figure 3.16:** Schematic of annular regions used to compute mean cloud number density as a function of radius,  $D$ , from cloud center. Periodic boundaries are denoted by the largest circle crossing the right boundary of the computational domain.

Cloud number density is multiplied with the distance to cloud center and weighted with the number of grid points and the size of each annular region. The y-axis is rescaled with the average cloud density over the entire domain. Therefore, a completely random (Poisson) distribution of clouds yields a rescaled value of one at all distances from cloud center. Figure 3.17 (left) illustrates cloud number density as a function of distance from cloud center for the 2 km control simulations. Different colours denote the different magnitudes of the prescribed forcing.

It is clear from this figure that convective activity in the vicinity of each cloud is not random, but depends on the magnitude of the forcing. An increased probability for clouds to develop in the near cloud environment is observed for all magnitudes of forcing (Figure 3.17 left). This clustering tendency is strongest for the -2 K/day (red) simulation and weakens systematically with increasing magnitude of the forcing. Similarly the area around the clouds where clustering occurs is largest in the -2 K/day simulation. The area around a cloud affected by this clustering is significantly smaller for the higher forced simulations than for -2 K/day (red). Furthermore, radiative forcings in the range -4 K/day to -12 K/day exhibit a similarly wide range of clustering around each cumulus cloud.

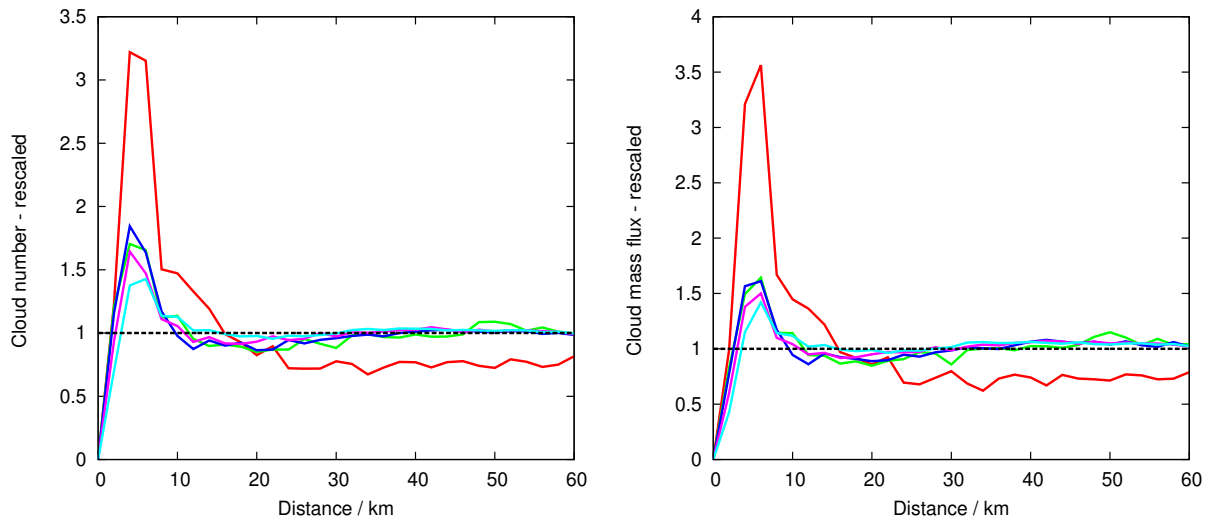


**Figure 3.17:** Rescaled cloud number density (left) and upward mass flux density (right) as a function of distance from cloud center for simulations at 2 km horizontal resolution. Different colours denote prescribed forcings of -2 K/day (red), -4 K/day (green), -6 K/day (blue), -8 K/day (purple) and -12 K/day (light blue) simulations.

A short range inhibition acts to reduce the number of clouds in the range of 10 to 25 km for all stronger forced simulations. At larger distances, these localised effects become negligible though and rescaled cloud number density fluctuates around a value of one, indicating a random distribution of clouds in the domain. This is true for all forcings except for the -2 K/day (red) simulation, exhibiting a small trend towards regularity in the cloud field at larger distances. Comparable behaviour of mass flux density in the near cloud environment is obtained in Figure 3.17 (right). In contrast, CC06 only observed the presence of clouds

in the near cloud environment in the weaker forced simulations. Randomly distributed cloud fields were obtained at distances larger than 20 km for all simulations with a small trend towards regularity in their -2 K/day simulation as well. Furthermore, short range inhibition effects in the higher forced simulations are stronger in CC06 with an additional convective inhibition in the near cloud environment for the stronger forced simulations.

The structure of the cloud fields can be further investigated by computing upward mass flux variance for a range of different sized subdomains within the model domain. Variances are plotted as a function of the inverse average number of clouds within the subregion. Following CC06, the corresponding theoretical prediction, a line with slope  $2^{1/2}$  is included in Figure 3.18 (grey solid). Different colours and point styles denote different magnitudes of the prescribed forcing.

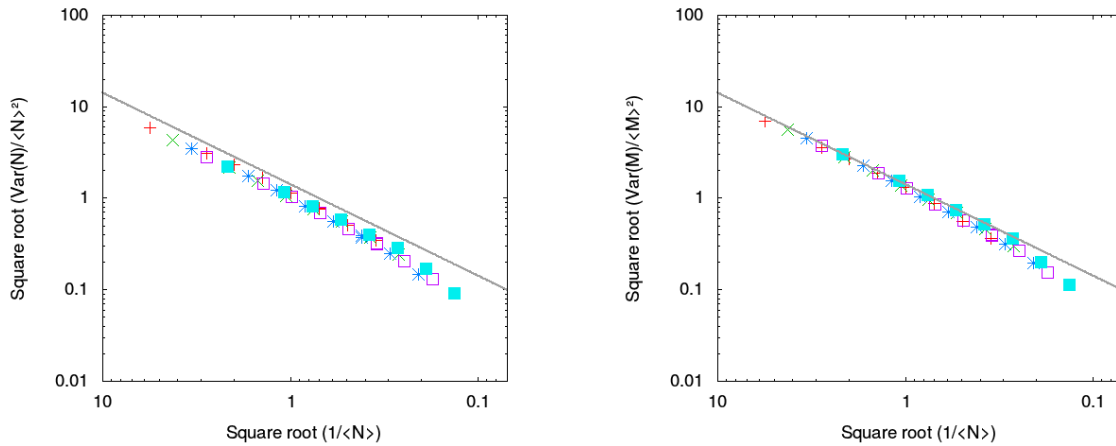


**Figure 3.18:** Variance of cloud number (left) and upward mass flux (right) at 2.4 km height. Colours denote cooling rates of -2 K/day (red cross), -4 K/day (green x), -6 K/day (blue asterisk), -8 K/day (purple box empty) and -12 K/day (light blue box filled).

Domain upward mass flux variance is found to be close to the theoretical random distribution for small and medium sized regions (Figure 3.18 left). Variances are observed to tail off with increasing subdomain size though, indicating the presence of regularity in the simulated cloud fields. Similar behaviour is observed for the variance of cloud number computed for different sized subregions of the domain (Figure 3.18 right). Deviations from the theoretical random distribution are slightly larger than for the mass flux variance, indicating an even larger trend towards regularity in the cloud field. Results obtained from analysing cloud number and cloud mass flux variances compare well to the findings of CC06.

### Concluding remarks

In this chapter the results of CC06 are successfully reproduced with the anelastic, non-hydrostatic fluid solver EULAG. Simulations are performed employing a horizontal resolu-



tion of 2 km and prescribing radiative cooling rates ranging from -2 K/day to -12 K/day. Even though some small differences are apparent, results of the control simulations compare well to the findings of CC06. In line with their results a systematic shift in the simulated atmospheric states with increasing forcing is observed. Domain total temperature and moisture content are found to decrease with increasing resolution analogously to CC06. However, boundary and shallow convective layers are observed to be less developed in this study. This is most likely owed to differences in the vertical resolution, the subgrid schemes and the surface flux parameterisation.

Applying the same criteria for defining a convective updraft, average values of domain upward mass flux and cloud fraction are systematically increasing with increasing forcing in line with CC06. Analysing the relation of upward mass flux and the magnitude of the forcing reveals a curved relationship rather than a linear one. This curvature is found to be owed to decreasing potential temperature lapse rates and increasing deviations from a moist adiabat with increasing forcing. Weighting the prescribed forcing with these stability changes results in the computation of an *effective forcing*. Thereafter analysing the relation between upward mass flux and this effective forcing, a linear relation is obtained as expected from CC06. Comparable scaling is obtained for convective fraction and average cloud size. Vertical velocity per cloud is found to be almost insensitive to the magnitude of the forcing as noted in CC06. Frequency distributions of cloud mass flux are found to be exponential and results compare well to CC06.

A small trend towards regularity is obtained, when analysing the variances of cloud number and upward mass flux, in line with the findings of CC06. However, a small tendency of clouds to develop in the near cloud environment is observed in this study over the entire range of prescribed forcings. In CC06 this mild clustering was only observed in the weakly forced simulations though.

In the next chapter, sensitivity of the 2 km control simulation results to the horizontal grid spacing is investigated. The full set of control simulations, prescribing radiative cooling rates from -2 K/day to -12 K/day, is repeated at horizontal resolutions of 1 km, 500 m, 250 m and 125 m. In addition, the question is addressed what horizontal resolution can be considered cloud-resolving and whether an inertial subrange is present in the high-resolution simulations.



## Chapter 4

# Resolution dependence of equilibrium convection

In the second part of this study, sensitivity of the 2 km control simulation results to horizontal grid spacing is investigated and compared to the results of Cohen and Craig (2006) (CC06). The set of control simulations (2 km) with prescribed cooling rates ranging from -2 K/day to -12 K/day is repeated at horizontal resolutions of 1 km, 500 m, 250 m and 125 m. In contrast to the control simulations, these high-resolution simulations are re-started from the corresponding coarser resolution simulation to shorten the time required for the simulated atmosphere to evolve to its new radiative-convective equilibrium state. For this purpose, the simulated atmospheric state of the coarser resolution simulation is interpolated on to the *new*, high-resolution model grid. The adjustment time needed to evolve to the *new* equilibrium state after such an interpolated re-start is decreased by factor of 3 to 4 in comparison to starting the simulations from a balanced sounding without any convective activity. To be conform with numerical consistency and stability criteria, increasing horizontal resolution requires corresponding refinements in the vertical grid spacing and model time step. Simulations with 125 m horizontal resolution are therefore computed on an isotropic grid with a vertical resolution of 125 m and a time step of 1 s. Coarser resolution simulations are performed with a vertical resolution of 200 m and a time step of 5 s. A Newtonian relaxation of the horizontal wind is applied to prevent spin up of mean model wind and associated wind shear.

In this chapter, first the simulated atmospheric states and their dependence on horizontal resolution are analysed. Thereinafter, the question is addressed whether the resolution is high enough to observe convergence of the results and the resolution dependence of the simulated atmosphere is compared to previous studies. In the second part of this study, cloud properties, cloud statistics and their sensitivity to horizontal resolution are analysed.

## 4.1 Dependence of the simulated atmosphere

### 4.1.1 Equilibrium vertical profiles

Within the radiative-convective equilibrium state the input of energy by surface fluxes of latent and sensible heat provides the amount of energy for the convective ensemble to compensate for the prescribed radiative cooling via subsidence warming (Cohen, 2001). Therefore, a significant dependence of the simulated atmospheric state to the magnitude of the forcing is the natural consequence and observed in the 2 km control simulations in Chapter 3. When increasing horizontal resolution stepwise from 2000 m to 125 m, mixing processes in the boundary layer and at the cloud edges become resolved as the simulations are approaching a large-eddy-resolving regime (LES). In contrast, for the coarser resolution simulations diffusion is the primary transport process in the boundary layer and at the cloud edges. Therefore, simulated atmospheric states are expected to differ from one another with increasing horizontal resolution.

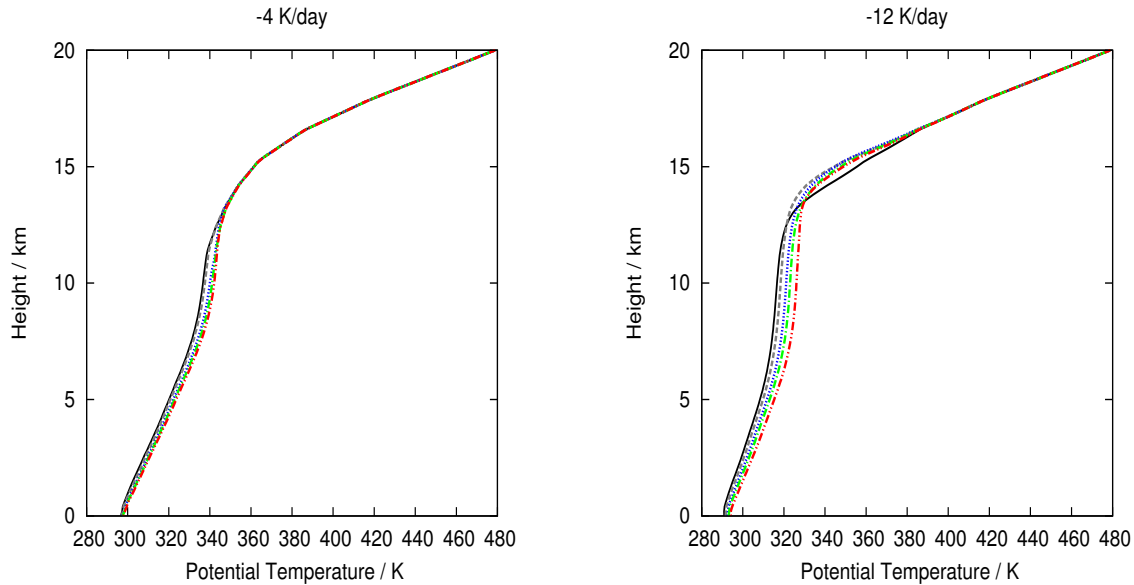


**Figure 4.1:** Vertical profiles of potential temperature for -4 K/day (left) and -12 K/day (right) simulations at different horizontal resolutions. Colours denote resolutions of 2 km (solid black), 1 km (dashed grey), 500 m (dotted blue), 250 m (dashed-dotted green) and 125 m (dashed-dotted-dotted red).

Analogously to analysing the dependence of the simulated model state on the magnitude of the prescribed radiative cooling in Chapter 3, vertical profiles of the horizontally averaged atmospheric properties are compared at constant forcing for different horizontal resolutions hereinafter. Figure 4.1 illustrates the evolution of horizontally averaged potential temperature with increasing resolution for the weakly forced -4 K/day simulations (left) and strongly forced -12 K/day simulations (right). Different line styles and colours denote

different horizontal resolutions. At both forcings, potential temperature in the domain increases slowly with increasing resolution as does the height of the tropopause. The largest increase is observed between the 1000 m (grey) and 500 m (blue) simulation at a forcing of  $-4$  K/day (left), dividing the simulations into coarser resolution and finer resolution simulations. In contrast, in the  $-12$  K/day (right) simulations a steady increase of potential temperature with increasing resolution is observed. Changes between the different resolutions are small compared to changes with increasing magnitude of the prescribed forcing though.

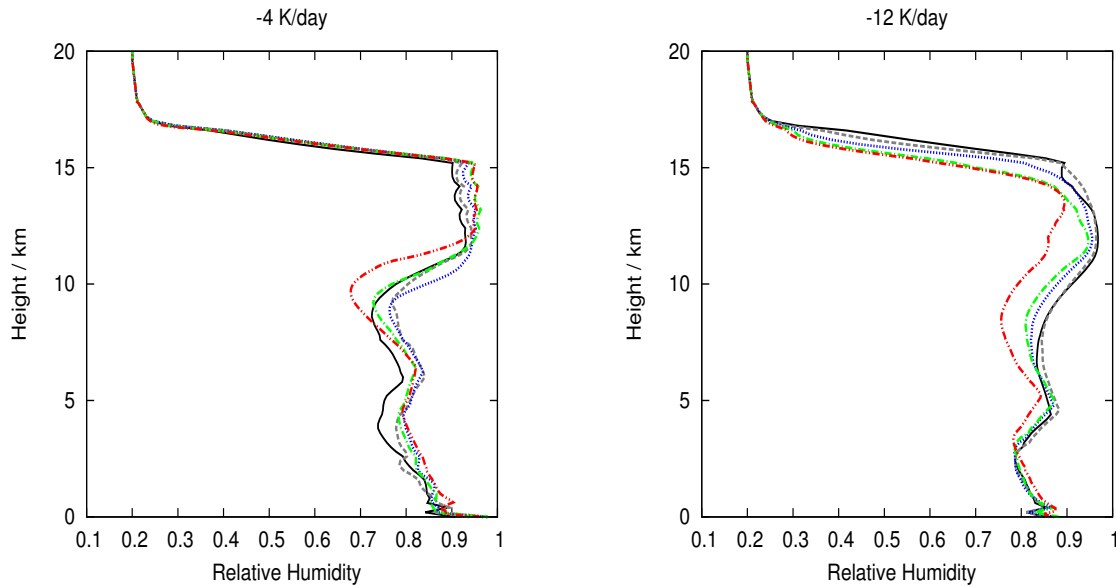


**Figure 4.2:** Vertical profiles of relative humidity for  $-4$  K/day (left) and  $-12$  K/day (right) simulations at different horizontal resolutions. Colours denote resolutions of 2 km (solid black), 1 km (dashed grey), 500 m (dotted blue), 250 m (dashed-dotted green) and 125 m (dashed-dotted-dotted red).

A stronger dependence on horizontal resolution is illustrated in vertical profiles of the relative humidity in Figure 4.2 for  $-4$  K/day (left) and  $-12$  K/day (right) simulations. In general, a tendency towards a drier equilibrium state with increasing resolution can be obtained for both forcings. The atmospheric state is observed to be systematically drier in terms of relative humidity and water vapour mixing ratio with increasing resolution (not shown). Lower tropospheric relative humidity is found to be quite insensitive to changes in resolution, whereas notable drying occurs in the mid- and upper troposphere. Upper tropospheric drying is observed to increase with the magnitude of the forcing. A systematic decrease of relative humidity is observed in all  $-12$  K/day simulations (right), whereas relative humidity at  $-4$  K/day cooling (left) and 2 km resolution (black) actually illustrates a drier atmospheric state than in the 1 km simulation (grey). However, with further increasing resolution the  $-4$  K/day simulations again follow the general drying tendency.

Transport of heat and moisture throughout the atmosphere is dominated by convective updrafts and the associated amount of subsidence warming. Thus, domain upward and downward mass fluxes in the convective atmosphere are constrained by the magnitude of the prescribed radiative cooling. Sensitivity of upward and downward mass flux to horizontal resolution is therefore expected to be small and in line with stability changes in the simulated atmosphere. Vertical profiles of upward and downward mass flux are illustrated in Figure 4.3. In general, upward and downward mass fluxes are found to compare well for all resolutions, even though small changes in the shape of the profiles are apparent.

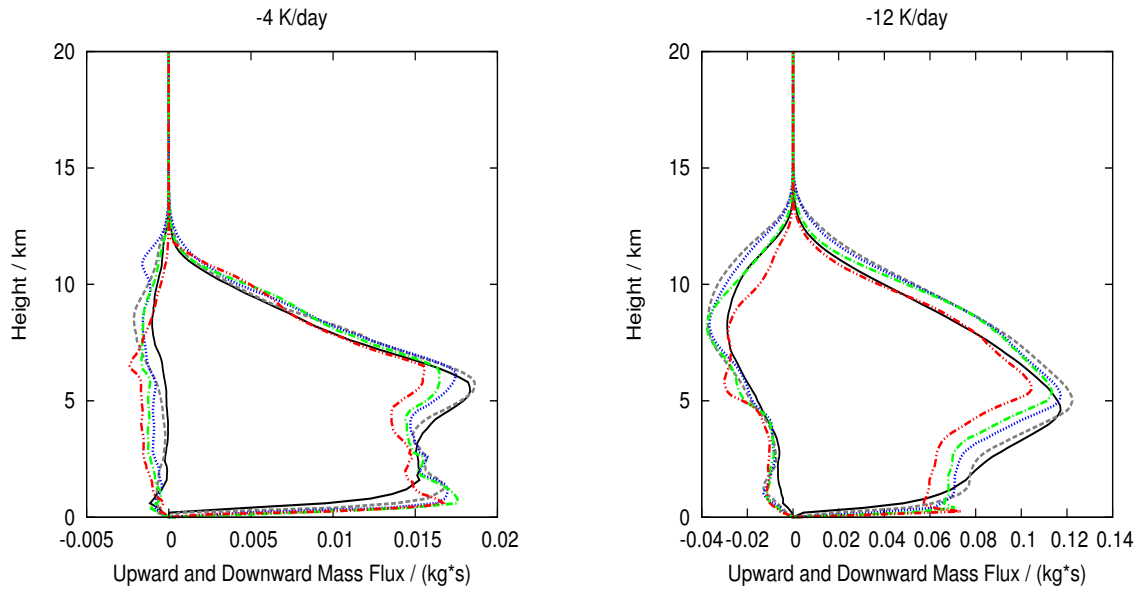


**Figure 4.3:** Vertical profiles of upward and downward mass flux for -4 K/day (left) and -12 K/day (right) simulations at different horizontal resolutions. Colours denote resolutions of 2 km (solid black), 1 km (dashed grey), 500 m (dotted blue), 250 m (dashed-dotted green) and 125 m (dashed-dotted-dotted red).

At both cooling rates, the bimodal shape obtained in the upward mass flux profiles (Figure 4.3) becomes more distinct with increasing resolution as the shallow convective maxima increase due to better resolved boundary layer processes. Meanwhile, the deep convective maxima decrease slightly and downdraft mass fluxes increase to keep the net vertical mass flux constant. Vertical profiles for the 250 m (green) and 125 m (red) simulations illustrate a similar shape of the upward and downward mass flux, with a small decrease of values with increasing resolution. These small changes in the vertical mass flux are in line with observed stability changes of the simulated atmosphere (not shown).

Another quantity closely connected to the magnitude of the radiative cooling is the fractional area of the domain, that is covered by convective updrafts (hereinafter: convective fraction). Vertical profiles of the convective fraction are illustrated in Figure 4.4 analogously to the previous figures. Its dependence on horizontal resolution is found to be more

significant than the dependence obtained for upward and downward mass fluxes. As noted in Figure 4.3 a more intense shallow convective maximum develops with increasing resolution which results in a more distinct bimodal structure in the convective fraction profiles as well. However, in contrast to the upward mass flux profiles, the deep convective maxima in the convective fraction profiles increase systematically with increasing horizontal resolution.

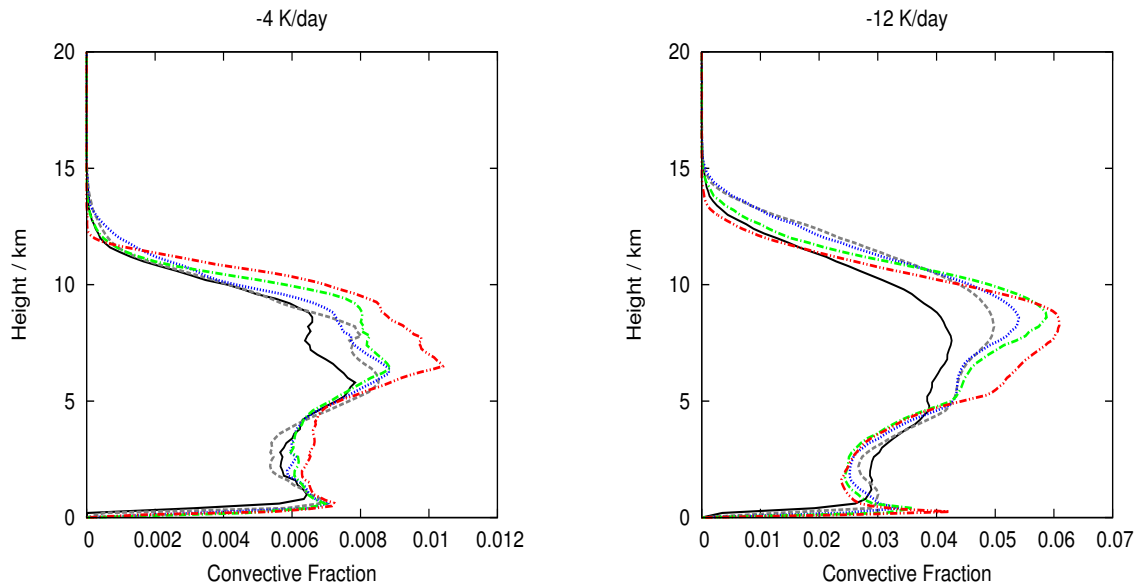


**Figure 4.4:** Vertical profiles of convective fraction for -4 K/day (left) and -12 K/day (right) simulations at different horizontal resolutions. Colours denote resolutions of 2 km (solid black), 1 km (dashed grey), 500 m (dotted blue), 250 m (dashed-dotted green) and 125 m (dashed-dotted-dotted red).

The most significant increase is observed when refining the grid spacing from 250 m (green) to 125 m (red). This may be owed to an additional adaption of the vertical grid spacing when re-starting the 125 m simulations from the 250 m equilibrium state. Better resolving boundary layer and cloud mixing processes are likely to be responsible for the observed increase in convective fraction. However, the observed changes of convective fraction with increasing resolution are small compared to the changes occurring when increasing the magnitude of the prescribed radiative cooling. Changes of the simulated cloud fields with increasing resolution and magnitude of the prescribed forcing are analysed in the next section.

### 4.1.2 Cloud field structure

A general impression of how the cloud fields develop with increasing resolution can be received by analysing horizontal cross-sections of the simulated cloud fields at different resolutions. Figures 4.5 to 4.7 illustrate horizontal cross-sections of the vertical velocity field at a height of 2.4 km at 2 km, 500 m and 125 m horizontal resolution for the -4 K/day (left) and -12 K/day (right) simulations. Blue contours denote the presence of condensed cloud water in the domain. Stepwise increasing horizontal resolution from 2 km to 125 m influences the structure of the cloud fields significantly.

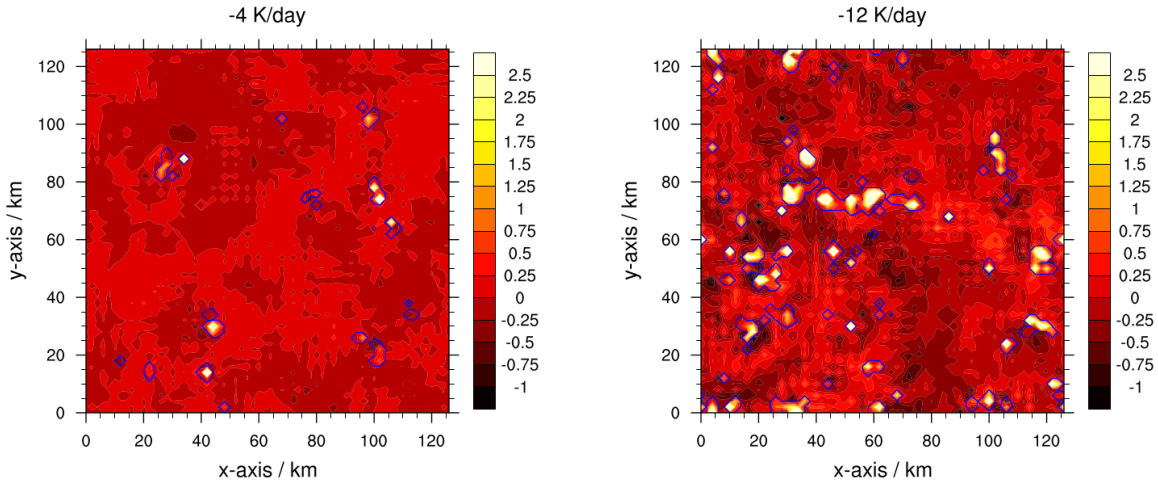


**Figure 4.5:** Horizontal cross-sections of the vertical velocity field in  $m/s$  for -4 K/day (left) and -12 K/day (right) simulations at 2 km horizontal resolution. Blue contours denote the presence of condensed cloud water.

At a horizontal resolution of 2 km convective clouds in the domain are under-resolved with their size being strongly limited by the grid scale. In these simulations, an increase in the magnitude of the prescribed forcing is found to primarily increase the number of clouds in the domain without significantly influencing their properties. This is in line with results of CC06. Convective clouds in the 2 km resolution simulations are randomly distributed throughout the domain. Comparable behaviour is observed in horizontal cross-sections of the 1 km resolution simulations (not shown). However, cloud size is found to decrease with increasing horizontal resolution due to being limited by the grid scale.

First changes in the structure of the cloud fields are observed when increasing horizontal resolution from 1 km to 500 m. Whereas the weaker forced simulations illustrate randomly distributed cloud fields at 500 m resolution (Figure 4.6 left), a trend towards organisation of the convective clouds is visible in the stronger forced simulations (Figure 4.6 right).



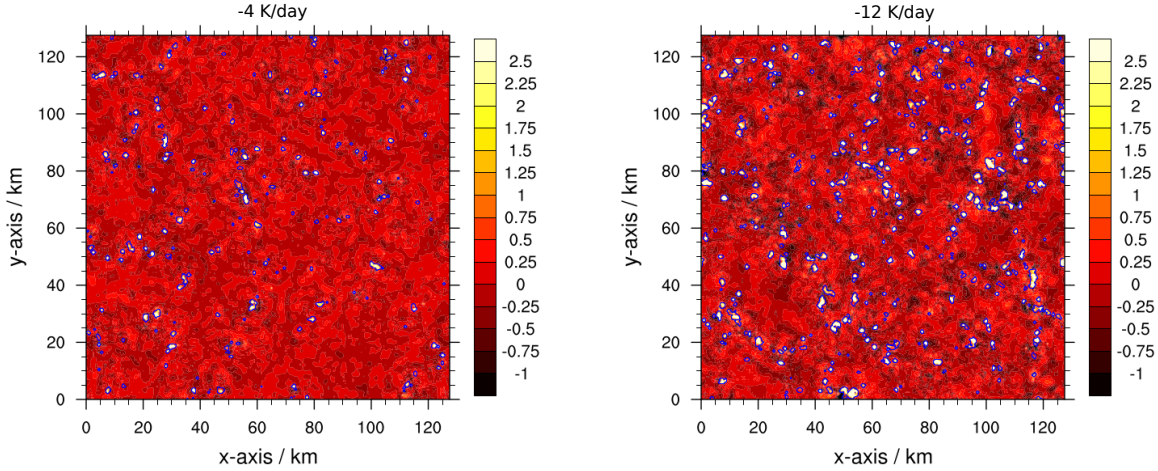


**Figure 4.6:** Horizontal cross-sections of the vertical velocity field for 500 m horizontal resolution as in Figure 4.5.

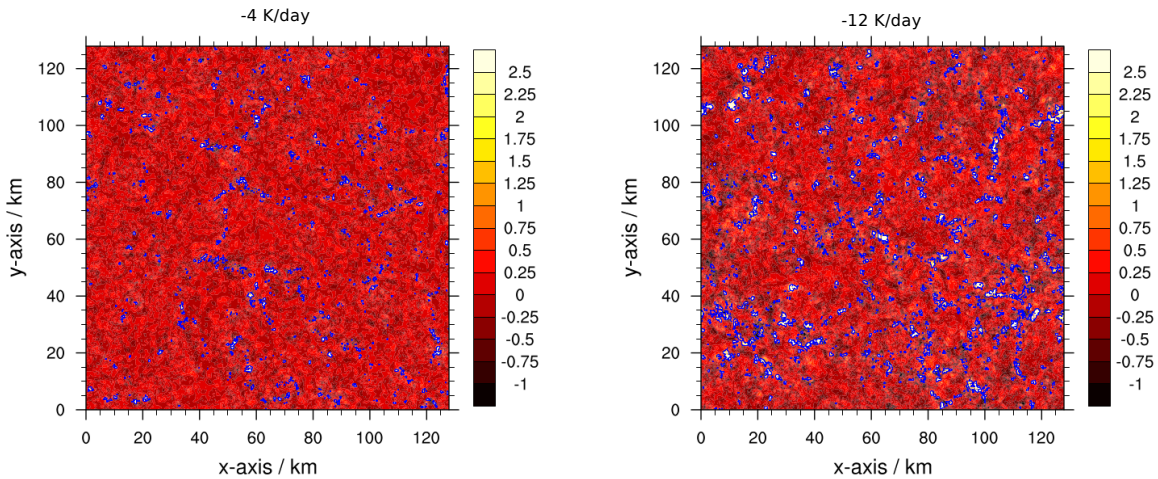


**Figure 4.7:** Horizontal cross-sections of the vertical velocity field for 125 m horizontal resolution as in Figure 4.5.

Cloud size further decreases with increasing resolution and furthermore, a small increase of cloud size with increasing magnitude of the forcing is observed at this resolution. This trend further intensifies in the 250 m simulations (not shown) and is a dominant feature in the 125 m simulations (Figure 4.7). Cloud sizes in the 125 m simulations illustrate a

significant dependence on the magnitude of the radiative cooling, systematically increasing with increasing magnitude of the prescribed forcing. Furthermore, a strong organisation of the convective clouds in the computational domain is obtained in the 125 m simulations. The size of these cloud clusters is increasing with the magnitude of the prescribed forcing and the convective clouds develop in band-like structures around cloud-free areas. These significant changes obtained in the cloud fields with increasing horizontal resolution are owed to better resolving intracloud turbulent processes. It is therefore of interest what grid spacing can be considered *cloud-resolving* and is necessary to observe convergence in cloud properties and statistics. Evaluation of these questions is undertaken in the next section.

### 4.1.3 Convergence of the simulated atmosphere

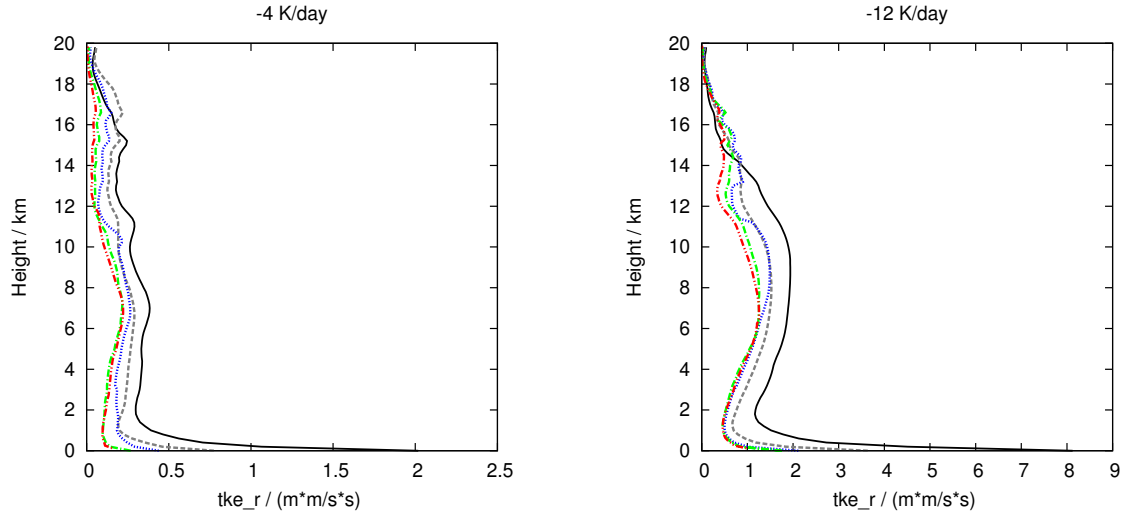
Until recently cloud-resolving simulations with 1 km to 2 km horizontal grid spacing have been considered sufficient when simulating deep convection in the atmosphere (Bryan et al., 2003). However, evaluating vertical profiles of the simulated model state and horizontal cross-sections of the vertical velocity field reveals a significant dependence of the simulated cloud fields on horizontal resolution. The question, what horizontal resolution is indeed cloud-resolving, is essential for assumptions in LES techniques to be valid and has been the motivation behind several recent studies on shallow convection (Bryan et al., 2003).

**Turbulent kinetic energy** A measure commonly used to examine the appropriateness of LES assumptions is the resolved turbulent kinetic energy,  $\langle e^r \rangle$ , the subgrid turbulent kinetic energy,  $\langle e^s \rangle$ , and the ratio of subgrid to total turbulent kinetic energy:

$$e^{ratio} = \frac{\langle e^s \rangle}{\langle e^r \rangle + \langle e^s \rangle} \quad (4.1)$$

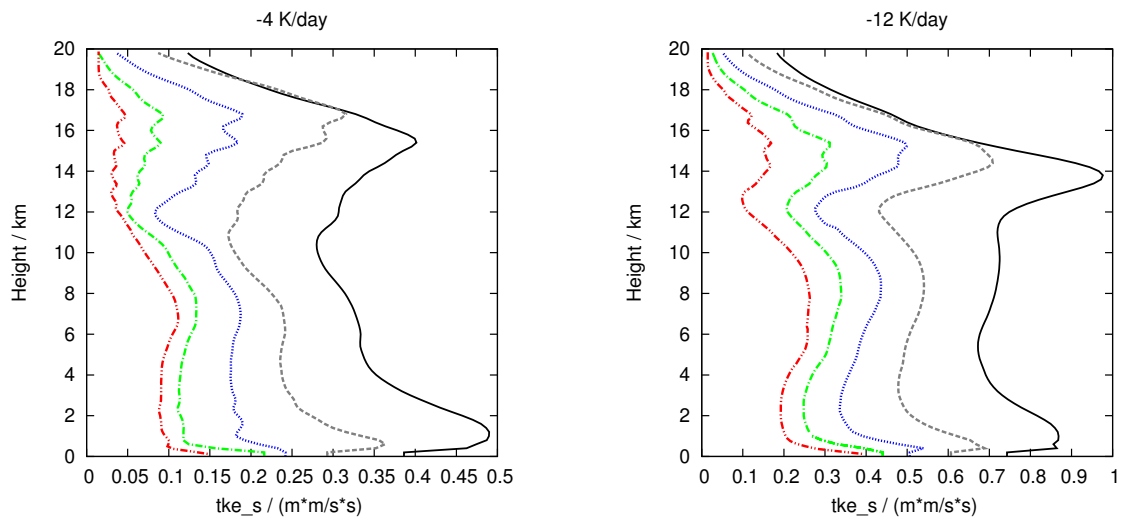
According to Bryan et al. (2003) it is desirable to have a low ratio of subgrid to total turbulent kinetic energy (tke) of approximately 10 % in large-eddy simulations.

Figure 4.8 illustrates horizontally averaged profiles of the resolved turbulent kinetic energy for the -4 K/day (left) and -12 K/day (right) simulations. Different line styles and colours denote different horizontal resolutions. At both forcings a small, systematic decrease of the resolved tke is illustrated in this figure. This small decrease of resolved tke is owed to the Newtonian relaxation of the horizontal wind applied in the simulations to prevent spin up of a mean horizontal wind in the simulations. This relaxation poses a small energy sink in the numerical simulations. The largest differences are obtained between the 2 km (black) and 1 km (grey) resolution simulations. This can be explained by the tendency for a mean wind to spin up is negligible small in the 2 km simulations. However, the differences obtained with increasing horizontal resolution are small compared to the overall changes in resolved tke comparing different magnitudes of the prescribed forcing.



**Figure 4.8:** Resolved turbulent kinetic energy profiles for -4 K/day (left) and -12 K/day (right) simulations. Colours denote resolutions of 2 km (solid black), 1 km (dashed grey), 500 m (dotted blue), 250 m (dashed-dotted green) and 125 m (dashed-dotted-dotted red).

Resolved tke profiles are found to be very similar for the 250 m (green) and 125 m (red) resolution simulations at both forcings. This can be interpreted as a sign of convergence of the simulated atmospheric properties. In terms of the subgrid tke, Figure 4.9 illustrates a general decrease with resolution for all forcings.



**Figure 4.9:** Subgrid turbulent kinetic energy profiles for -4 K/day (left) and -12 K/day (right) simulations. Colours denote resolutions of 2 km (solid black), 1 km (dashed grey), 500 m (dotted blue), 250 m (dashed-dotted green) and 125 m (dashed-dotted-dotted red).

Differences in subgrid tke are largest between the 2 km (black) and 1 km (grey) simulations and smallest between the 250 m (green) and 125 m (red) simulations, again indicating convergence of the simulated model states. The observed decrease of subgrid tke with increasing resolution is owed to resolving turbulent motions and in line with expectations and results of Bryan et al. (2003). Well-resolved turbulent motions are especially important in the boundary layer and at the cloud edges. The influence of explicitly resolving boundary layer eddies compared to a subgrid transport is clearly illustrated in this figure. The shape of the vertical profiles at a height of approximately 1 km (shallow convective maximum) changes significantly between the 1 km (grey) and 500 m (blue) simulations at weaker forcings (left) and between the 500 m (blue) and 250 m (green) simulations at stronger forcings (right). Values of the subgrid tke in the boundary layer are decreasing as the transport is performed by the turbulent eddies rather than the subgrid turbulence scheme.

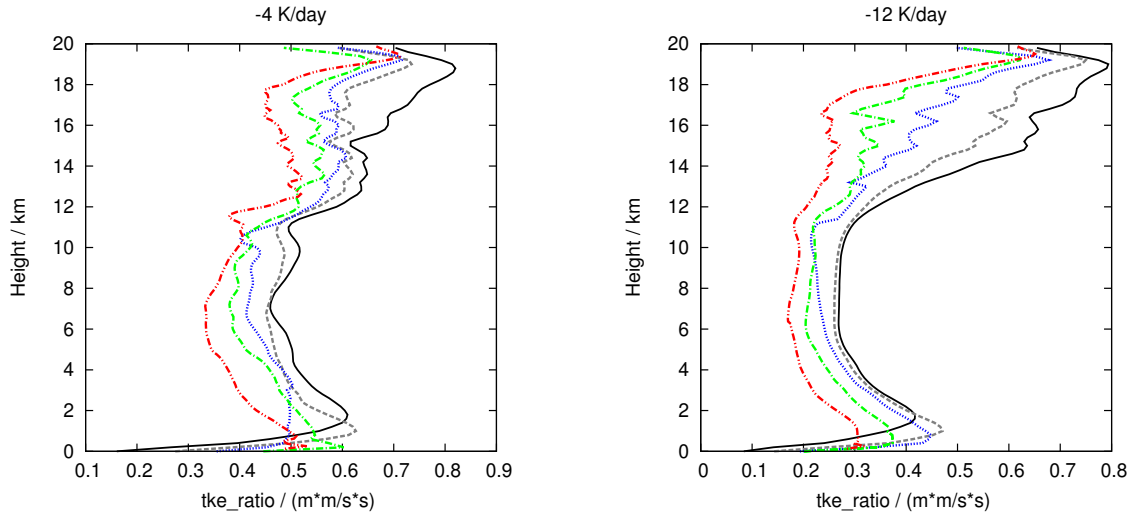


**Figure 4.10:** Ratio of subgrid to total turbulent kinetic energy for -4 K/day (left) and -12 K/day (right) simulations. Colours denote resolutions of 2 km (solid black), 1 km (dashed grey), 500 m (dotted blue), 250 m (dashed-dotted green) and 125 m (dashed-dotted-dotted red).

Bryan et al. (2003) suggested, one expects a decrease of the ratio of subgrid to total turbulent kinetic energy with increasing resolution and the better resolved turbulent motions. He denoted low values of the tke ratio to be essential for the assumptions in LES techniques to be valid. Figure 4.10 illustrates horizontally averaged profiles of the tke-ratio as denoted in Equation (4.1). It is clear from this figure that the ratio of subgrid to total tke decreases systematically with increasing resolution. Values decrease from 0.6 to 0.5 at the height of the shallow convective maximum in the -4 K/day simulations and from 0.45 to 0.3 in the -12 K/day simulations. Minimum values of 0.35 in the -4 K/day and 0.2 in the -12 K/day simulation are obtained at 125 m resolution. These ranges are comparable to the findings of Bryan et al. (2003) in their squall line simulations. Values in the range

of 0.87 in their high-resolution, strong shear simulations to 0.1 in their high-resolution, weak shear simulations were obtained in their study. Bryan et al. (2003) indicates values of approximately 0.1 for LES techniques to work as designed.

**Vertical velocity spectra** Another possibility to make a judgement about the grid spacing required to resolve the large eddies containing most of the kinetic energy and flux in the turbulent flow, is to evaluate one-dimensional vertical velocity spectra. In order for the traditional LES closures to be appropriate, one expects an inertial subrange present in the simulations. Hence, the spectra are anticipated to decrease with increasing wavenumber as  $\kappa^{-5/3}$  beyond the energy containing range (Moeng, 1984; Bryan et al., 2003). Figure 4.11 illustrates the one-dimensional vertical velocity spectra at a height of 2.4 km for the -4 K/day (left) and -12 K/day (right) simulations. Colours denote resolutions of 2 km (solid black), 1 km (dashed grey), 500 m (dotted blue), 250 m (dashed-dotted green) and 125 m (dashed-dotted-dotted red).

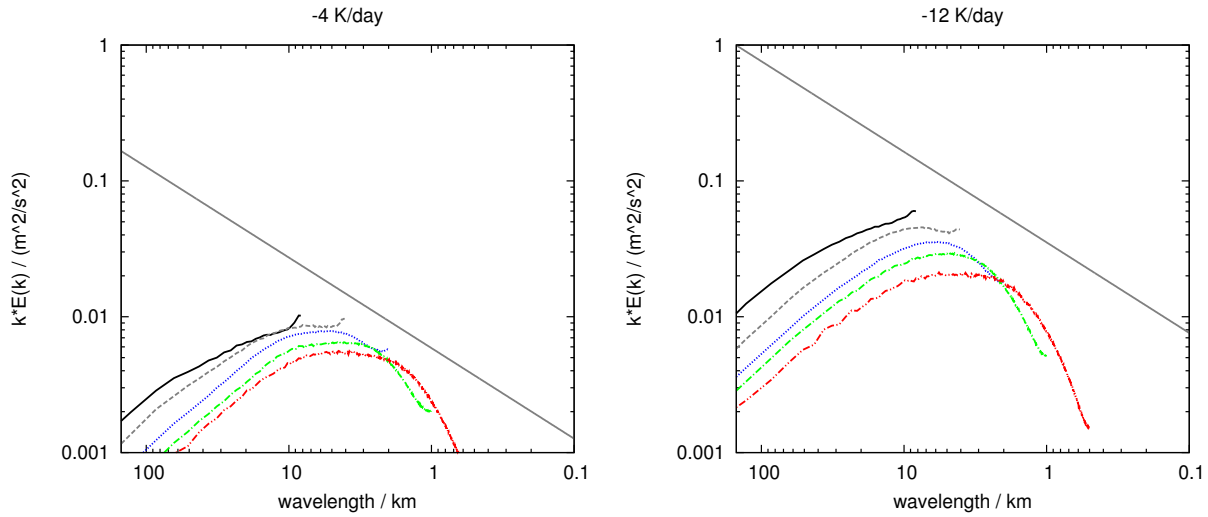


**Figure 4.11:** One-dimensional vertical velocity spectra at 2.4 km height for -4 K/day (left) and -12 K/day (right) simulations. Colours denote resolutions of 2 km (solid black), 1 km (dashed grey), 500 m (dotted blue), 250 m (dashed-dotted green) and 125 m (dashed-dotted-dotted red).

It is illustrated in this figure that for resolutions of 500 m (blue) and higher (green and red), the one-dimensional vertical velocity spectra decrease with increasing wavenumber beyond the energy containing range. However, the spectra are found to be slightly shallower than  $\kappa^{-5/3}$ . With increasing magnitude of the prescribed forcing the amplitude of the energy spectra increases systematically. Analogously to findings of Bryan et al. (2003) in their squall line simulations, the amplitude and wavelength of the energy peak systematically vary with increasing resolution. The location of the maximum shifts to smaller scales with increasing resolution in line with findings of Bryan et al. (2003). However, the magnitude of the peak in this study decreases, whereas it increases in Bryan et al. (2003). This decrease however, follows the decrease of the resolved  $\tau_{ke}$  observed in Figure 4.8. Even though the magnitude of the vertical velocity spectra maxima decreases with increasing resolution, differences between the 250 m (green) and 125 m (red) spectra are found to be

significantly smaller than for the coarser resolution simulations. In addition, the position of the maxima is comparable for simulations performed at 250 m and 125 m resolution. One can interpret this as another sign of converging atmospheric model states. Overall it has been shown in this section that changes of the atmospheric properties with increasing resolution are for the most part consistent with results of previous studies. The most significant systematic changes observed with increasing resolution are an increasing number of clouds in the domain and a decreasing cloud size with increasing horizontal resolution. Evaluation of the resolved and subgrid components of the turbulent kinetic energy and the analysis of vertical velocity spectra indicates an approach towards a LES regime exhibiting first signs of a convergence in the high-resolution simulations. Resolving boundary layer turbulence and cloud edge mixing processes is suspected to cause the observed changes in the fractional area of the domain covered by convection as well as the clustering obtained in the cloud fields. The effect of these changes on the cloud properties and statistics are analysed in the following part of this study.

## 4.2 Sensitivity of equilibrium convective ensemble statistics

Evaluating the dependence of the mean model state on horizontal resolution has revealed changes in cloud size, cloud number and the shape of the cloud field. In this section, these changes are analysed statistically. First, the distribution of cloud size is evaluated as it is of great interest to the scientific community due to its importance in numerical simulations and parameterisations. Second, the distribution of cloud mass flux derived to be exponential in CC06 is evaluated with increasing horizontal resolution. Furthermore, it is analysed how cloud properties in high-resolution simulations evolve with increasing magnitude of the prescribed forcing. Third, the clustering tendencies observed in the cloud fields at high-resolution are analysed and underlying processes are investigated.

### 4.2.1 Distribution of cloud size

Cumulus cloud sizes and their distribution have been of interest to the meteorological community ever since the first measurements over cloudy regions were taken by airplanes (Plank, 1969). A theoretical distribution of cumulus cloud size was first included in a parameterisation scheme by Arakawa and Schubert (1974) and up to now, the question of how the cloud size distribution is shaped is an ongoing topic of research. Early studies argue the distribution to be exponential, log-normal or power law, others to resemble a double power law with a distinct scale break at cloud diameters in the range 400 m to 1000 m. In this section, the distribution of cloud size and its sensitivity to horizontal resolution is analysed for an ensemble of deep convective cumulus clouds in a state of radiative-convective equilibrium. Individual cloud statistics are computed as denoted in Chapter 3 (control simulations). Grid points are defined to be cloudy if their vertical

velocity exceeds a threshold of 1 m/s and their condensed cloud water mixing content is non-zero. A simple and efficient search algorithm defines all connected cloudy grid points as clouds and computes cloud size, vertical velocity and cloud mass flux. Figure 4.12 depicts histograms of the cloud size frequency distribution in log-linear space for a forcing of -4 K/day (top) and -12 K/day (bottom) at 2 km resolution (left) and 125 m resolution (right).

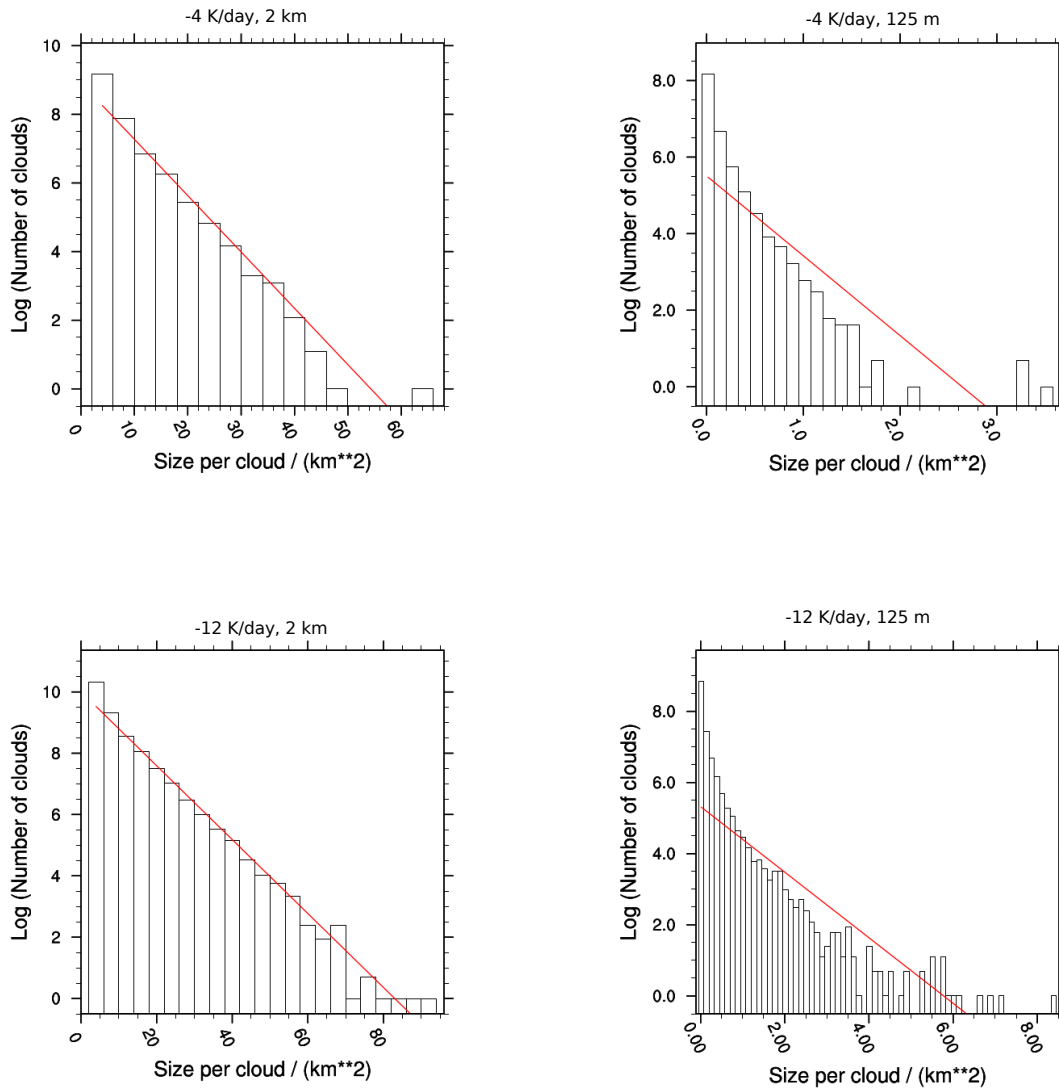


**Figure 4.12:** Histograms of the cloud size frequency distribution in log-linear space for -4 K/day (top) and -12 K/day (bottom) simulations at 2 km (left) and 125 m resolution (right). Red lines denote least squares best fits to the cloud data in log-linear space.



A least squares best fit to the observed frequencies is plotted in each of the histograms. Regarding the general evolution of cloud size with increasing resolution, a systematic decrease by a factor of ten is obtained increasing horizontal resolution from 2 km to 125 m. This is in line with the observations made when comparing horizontal cross-sections of the vertical velocity field at different resolutions (Figure 4.5 to 4.7).

As pointed out in Chapter 3, the cloud size distribution in the 2 km resolution simulations strongly resembles an exponential at all magnitudes of the prescribed forcing. This follows the suggestion of Lennard (2004). He assumes an exponential distribution of cloud size to be apparent if the entire cloud ensemble falls to the right hand side of the proposed scale break in the double power law distribution. In this study, with increasing resolution, cloud size distributions are found to deviate strongly from the exponential distribution. A significant number of large clouds are observed, inducing a tail on the right side of the cloud size distribution. These deviations from the exponential distribution are larger at high-resolutions with a wider tail on the right hand side. Furthermore, they are found to be more distinct in simulations with stronger radiative forcing than in the weakly forced simulations.

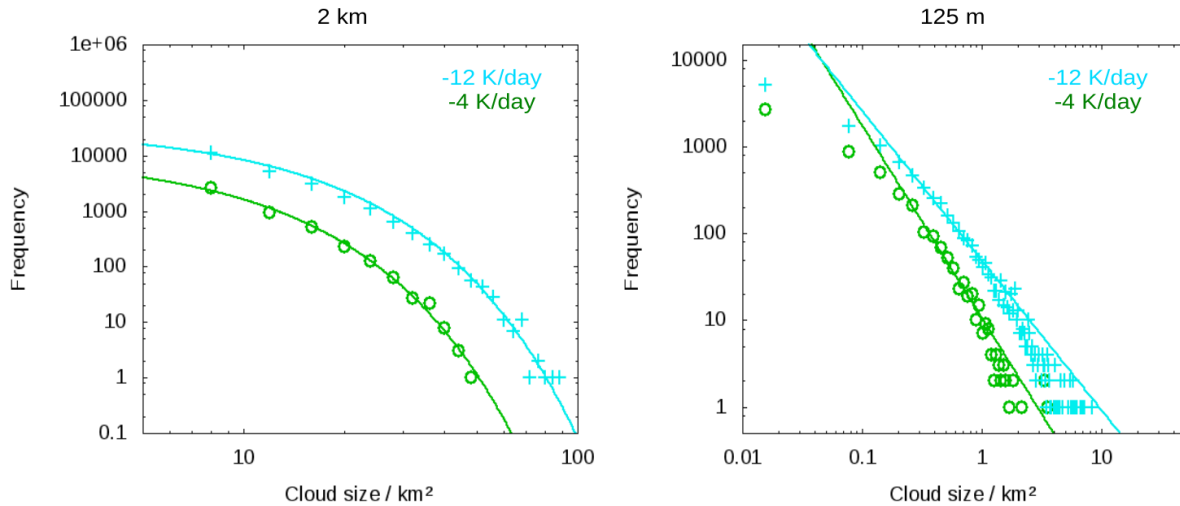


**Figure 4.13:** Frequency distribution of cloud size in log-log space for -4 K/day (green) and -12 K/day (blue) simulations at 2 km (left) and 125 m resolution (right). Lines denote an exponential at 2 km resolution (left) and a power law fit to part of the data at 125 m resolution (right).

A double power law distribution of cloud size with a distinct scale break between 400 m and 1 km has been proposed in earlier studies (Sengupta et al., 1990; Neggers et al., 2003; Lennard, 2004). The question, whether a power law or double power law poses an adequate fit to the observed size distribution in the high-resolution simulations is investigated in Figure 4.13. Cloud size distributions are replotted in log-log space for the -4 K/day (green) and -12 K/day (blue) simulations at 2 km resolution (left) and 125 m resolution



(right). Lines denote an exponential fit to the data at 2 km resolution and a power law fit is computed in the 125 m resolution simulations. It is evident that an exponential is indeed the best fit to the observed cloud size distributions in the 2 km control simulations and all data points compare well to the exponential fit (Figure 4.13 left). In contrast, a power law fits well in the 125 m simulations neglecting cloud sizes smaller than  $0.5 \text{ km}^2$  (Figure 4.13 right). However, the number of clouds exhibiting a size smaller than  $0.5 \text{ km}^2$  is large. This raises the questions of the appropriateness of fitting a power law distribution to the 125 m simulation results.

One can conclude from Figure 4.13 that with increasing horizontal resolution, the cloud size distributions are developing from an exponential at 2 km to resembling a power law-like distribution at 125 m. Similar cloud size distributions were obtained in Heus and Seifert (2013) in their high-resolution simulations of shallow convection. However, one needs to point out that the power law only fits well neglecting cloud sizes smaller than 500 m and a different fit needs to be found for smaller clouds. One may propose that the distribution of cloud size is evolving from an exponential towards a double power with a scale break at approximately 500 m. Simulation results have not converged at 125 m resolution though. It is of great interest to analyse what effect these changes in cloud size distribution have on the distribution of cloud mass flux, predicted to be exponential in CC06.

### 4.2.2 Distribution of cloud mass flux

Vertical transport in convective clouds is an important quantity often used in parameterisations of convective processes. The probability density function for cloud mass flux has been derived to be exponential by Craig and Cohen (2006) and validated in 2 km resolution simulations in Cohen and Craig (2006). In this study, the exponential distribution of cloud mass flux is successfully reproduced in 2 km control simulations with the numerical flow solver EULAG. Sensitivity of these results on horizontal resolution is evaluated. Analysing the resolution dependence of cloud size earlier in this section the distributions of cloud size are found to evolve from an exponential at 2 km resolution to a power law at 125 m resolution with a possible scale break at 500 m. It is therefore questionable whether the exponential distribution of cloud mass flux CC06 is indeed valid in high-resolution, cloud-resolving simulations.

Figure 4.14 depicts histograms of cloud mass flux for  $-4 \text{ K/day}$  (top) and  $-12 \text{ K/day}$  (bottom) simulations at 2 km (left) and 125 m resolution (right) in a log-linear environment. A least squares best fit to the data is denoted by a red line and a maximum entropy fit is illustrated by a blue line for each simulation. As noted in Chapter 3 the theoretical distribution denoted in Equation (1.1) corresponds to a maximum entropy fit which is not as sensitive to outliers of the frequency distribution as a least squares fit. It is clear from this figure that the distribution of cloud mass flux does deviate away from an exponential with increasing horizontal resolution. Distributions are observed to be exponential at 2 km resolution with close agreement of the least squares and maximum entropy best

fits. Stepwise increasing horizontal resolution however, generally decreases cloud mass flux values in the domain and significantly changes the shape of the distribution. An excess of high mass flux clouds develops for all magnitudes of the prescribed radiative cooling in the high-resolution simulations. This excess of clouds, depicted in the tail on the right hand side of the cloud mass flux distribution, is more distinct for high-resolutions and larger magnitudes of the prescribed forcing.

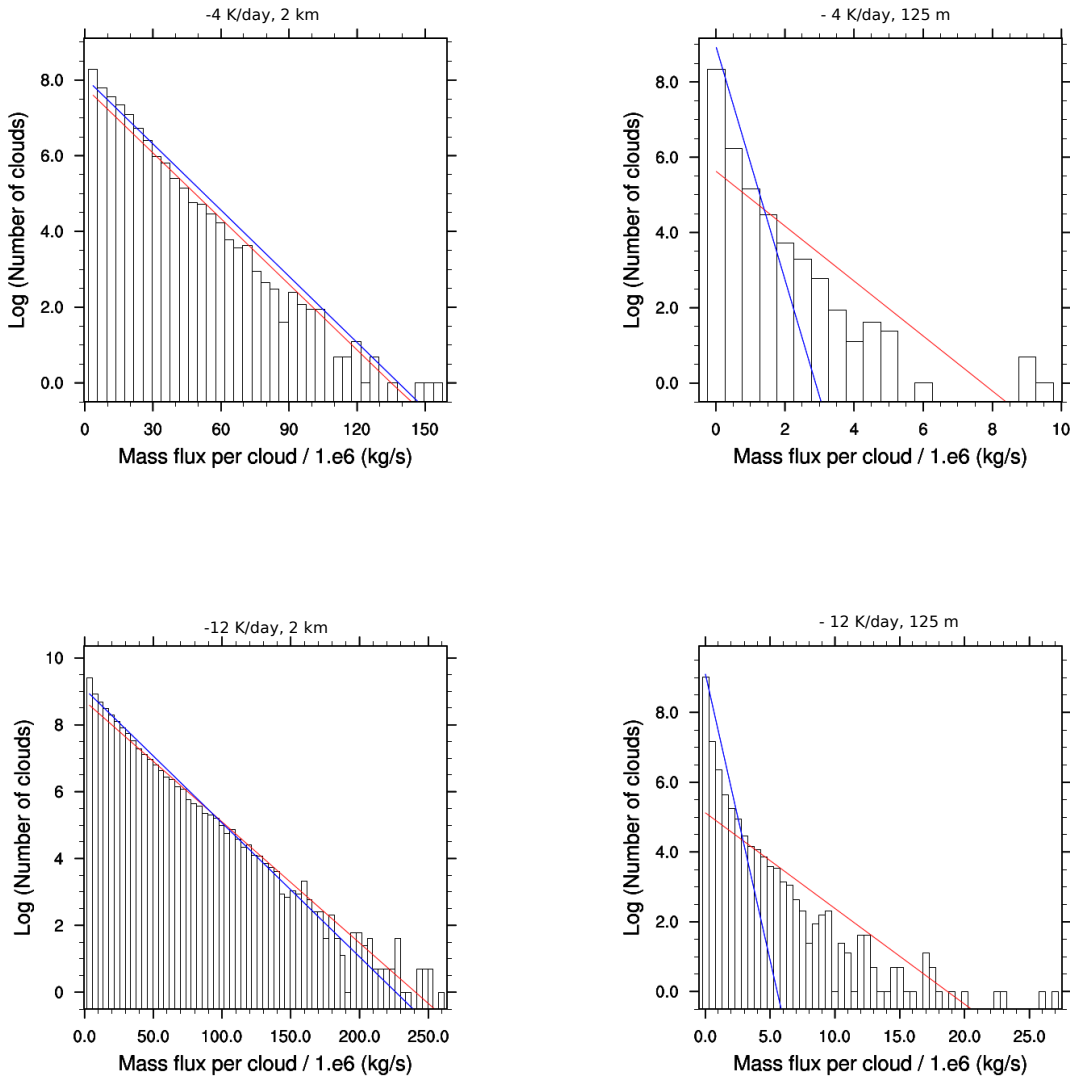


**Figure 4.14:** Cloud mass flux distribution for -4 K/day (top) and -12 K/day (bottom) simulations at 2 km (left) and 125 m resolution (right). Least squares best fit denoted by the red and maximum entropy fit by the blue line.

For the high-resolution simulations the maximum entropy fit does not account for the excess of large mass flux clouds, whereas the least squares best fit does not include the large number of small mass flux clouds. It is therefore important to gain knowledge about the underlying processes and structures in the cloud field responsible for this excess of large mass flux clouds in the high-resolution simulations. Comparing the distributions of cloud size and cloud mass flux, a similar change in the shape of the distributions with increasing resolution is obtained. Furthermore, a general decrease of cloud size and cloud mass flux values is observed. However, changes in the cloud vertical velocity may also play a role in the changes of the cloud mass flux distributions.

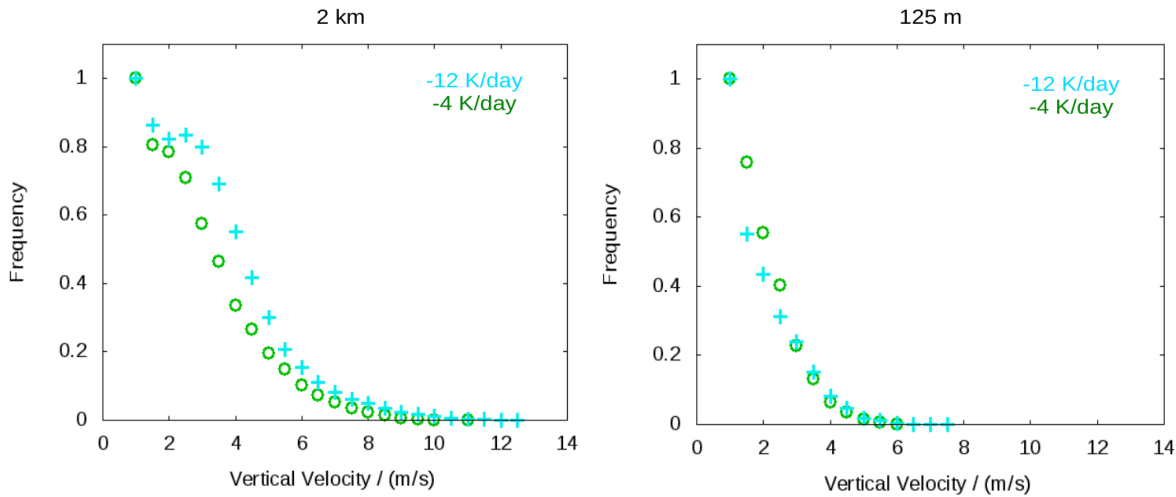


**Figure 4.15:** Vertical velocity per cloud for -4 K/day (green) and -12 K/day (blue) radiative cooling at 2 km (left) and 125 m (right).

The normalised frequency distribution of vertical velocity per cloud is illustrated in Figure 4.15. Vertical velocities obtained in the 2 km control simulations (left) are compared to results of the 125 m simulations (right) at radiative cooling rates of -4 K/day (green) and -12 K/day (blue). In contrast to cloud size and cloud mass flux, the general shape of these frequency distributions is comparable at all forcings and resolutions. The highest frequency values are observed for the smallest velocity possible (1 m/s) in all simulations and frequency decreases systematically with increasing vertical velocity. At 2 km resolution (left), the stronger forced simulations exhibit slightly larger velocities than the weaker ones. More clouds with velocities in the range 3 m/s to 5 m/s are observed and maximum velocities are slightly larger in the strong forcing simulations than in the weaker ones. However, with increasing horizontal resolution this small dependence of vertical velocity on the magnitude of the forcing becomes negligible. Distributions at 125 m (right) agree well for -4 K/day (green) and -12 K/day (blue) with slightly larger frequencies observed in the -4 K/day simulation in the range of 2 m/s and 3 m/s. Furthermore, larger velocities are obtained on the right hand side of the distribution for the -12 K/day simulation than

for  $-4$  K/day. In addition, a small change in the shape of the distribution is apparent when increasing resolution from 2 km to 125 m. With increasing resolution the distribution of cloud vertical velocity evolves to be steeper at 125 m resolution and flattens out at smaller velocities. In the  $-4$  K/day simulation maximum vertical velocities of approximately 11 m/s at 2 km resolution decrease to 6 m/s in the 125 m simulation. Therefore, one might expect a small decrease of the ensemble-average vertical velocity per cloud with increasing horizontal resolution. The general shape of the distribution however, is found to be insensitive to changes in the magnitude of the prescribed forcing and horizontal resolution. In addition, changes observed in vertical velocity with increasing resolution are small compared to changes in the cloud size distributions though.

From analysing the distributions of cloud size, cloud mass flux and vertical velocity, one can conclude that the significant changes observed in cloud mass flux distribution with increasing horizontal resolution are for the most part owed to changes of cloud size. Changes observed in vertical velocity per cloud are small compared to the overall decrease of cloud size with decreasing grid spacing. It is therefore important to gain more knowledge about the underlying processes responsible for the changes observed in the cloud size and hence, the cloud mass flux distributions. The observed changes in the shape and size of the convective clouds are analysed in the following section.

### The issue of “How to define a cloud”

A convectionally used, simple cloud definition has been applied in this study to reproduce results of CC06 at 2 km horizontal resolution and to investigate the dependence of results on increasing resolution. A grid point is defined to be cloudy if its vertical velocity exceeds 1 m/s and its condensed cloud water content is non-zero. Directly connected cloudy grid points (4-connected method) are then designated to belong to the same cloud. Evaluating the sensitivity of cloud properties to horizontal resolution has revealed an increasing trend of cloud size and cloud mass flux to decrease with resolution and forcing. Furthermore, a tendency of convective clustering is observed with increasing resolution. Studies by Dawe and Austin (2012) and Heus and Seifert (2013) have noted a common issue in the tracking of convective cumulus clouds, the problem of overly connected clouds. A cloud is a process not an object, subject to condensation, evaporation, merging and splitting. They interact with other clouds, briefly connecting in space and time while mainly keeping their own properties. Hence, one can conclude that connecting these clouds into large cloud system is what happens when all adjacent cloudy grid points are denoted to be part of one cloud.

In order to analyse this assumption Figure 4.16 illustrates a random snapshot of the cloudy grid points at 2.4 km height in a 500 m resolution simulation at  $-12$  K/day cooling. At this resolution, first signs of clustering in the cloud fields are obtained and a couple of large cloud systems are observed.

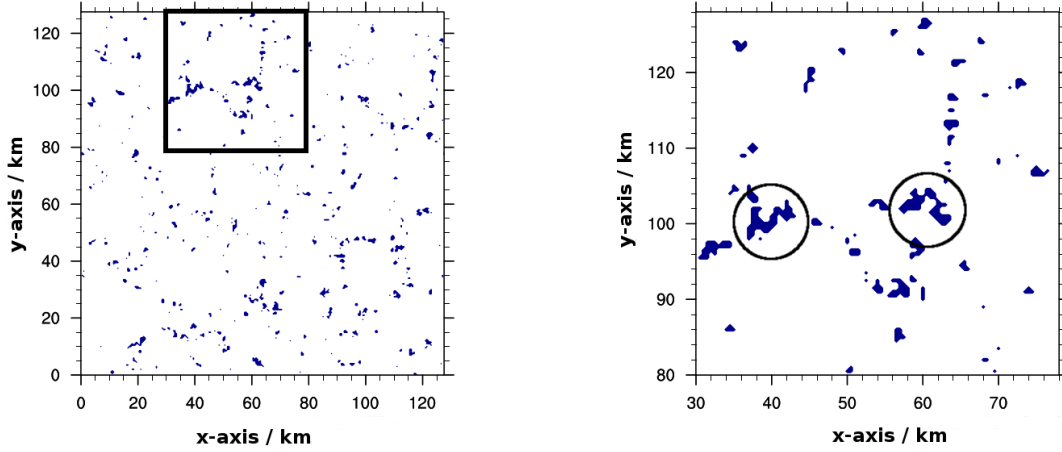


**Figure 4.16:** Snapshot of the cloud field at 2.4 km height (left) as identified by the search algorithm in a 500 m resolution simulation at -12 K/day cooling. Black box denotes the subdomain replotted and enlarged on the right side of the figure. Black circles denote two of the large clouds detected by the search algorithm.

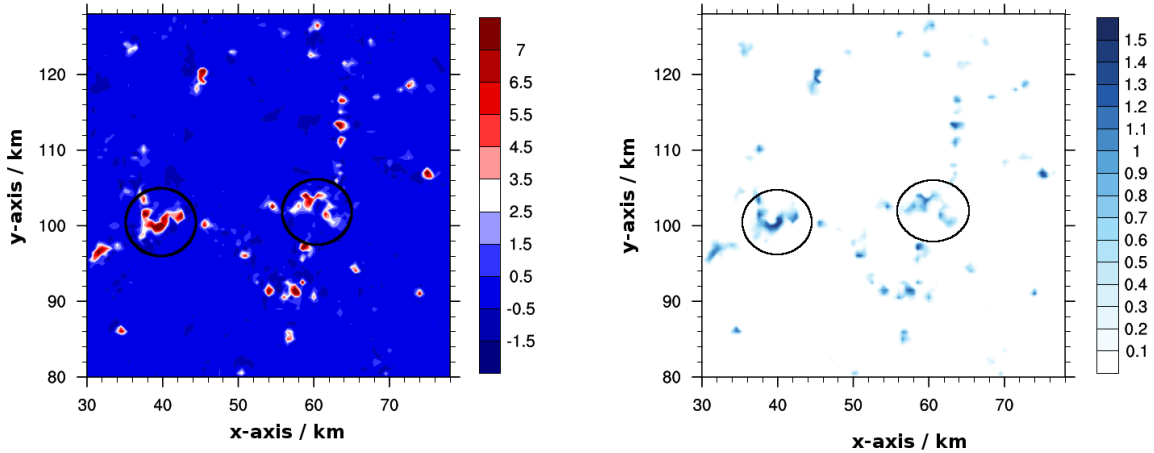


**Figure 4.17:** Snapshots of the vertical velocity field in  $m/s$  (left) and condensed cloud water mixing ratio field in  $g/kg$  (right) at same time and height as Figure 4.16.

The black box in Figure 4.16 (left) denotes the subdomain of the cloud field enlarged and replotted on the right hand side of the figure. Within this subdomain the trend towards

clustering is clearly visible as well and two large cloud systems are observed (black circles). In comparison to the other clouds in the subdomain these cloud systems are not only significantly larger in size, but also have an usual shape. The traditional cloud search algorithm, as applied in CC06 and used previously in this study, identifies these connected cloudy points to be part of one cloud. Figure 4.17 illustrates the vertical velocity field (left) and cloud condensed water field (right) used for computing the cloud field in Figure 4.16 with the traditional cloud search algorithm. Examining the two encircled large clouds in these figures, several local maxima in the vertical velocity and cloud water fields are apparent within each “large” cloud. By eye, the cloud in the left circle depicts at least four local maxima in the vertical velocity field and three in the condensed cloud water field. The bigger cloudlet in the middle is briefly connected to the smaller ones on its left and right side. However, analysing the bigger cloudlet in the middle, one may assume this bigger cloudlet consists of two cores as well. The cloud in the right circle exhibits an even stronger partitioning. In the vertical velocity field, three distinct cloudlets are observed, connected by grid points barely exceeding the vertical velocity threshold. Similar structures are observed in the cloud water field, however, the separation of the middle and right cloudlet is more distinct than of the left and middle ones.

From these figures and studies of shallow cumulus convection (Siebesma and Cuijpers, 1995; Dawe and Austin, 2012; Heus and Seifert, 2013) it is clear that clouds are separate processes for all purposes. However, these clouds can be spatially connected to each other at some point in time during their life cycles, which has to be considered when defining a convective cloud. In the tracking of shallow convection the problem of overly connected clouds is solved by partitioning cloud systems into their separate cloudlets. Each cloudlet is formed around a cloud core possibly connected to one or more adjacent cloudlets. Merging and splitting in these studies only takes place if two or more cloud cores connect with or separate from one another. The methodologies for defining the cloud cores and cloudlets in previous studies however, differ slightly from one to the other. Adopting this way of thinking, a new search algorithm is developed and applied in this study hereinafter called the *local-maximum method*.

**The local-maximum method** is strongly motivated by the cloud tracking algorithms applied in Dawe and Austin (2012) and Heus and Seifert (2013). However, no cloud tracking is performed in this study and the large number of grid points in the high-resolution computational domains requires a search algorithm to be computationally efficient. Within the local-maximum method a search algorithm as described in Chapter 3 (Hoshen and Kopelman, 1976; Dahl, 2010) is used to identify local maxima in the vertical velocity field. A local maximum grid point is defined if its vertical velocity is larger than or equal to the velocities at its directly neighbouring grid points and if its condensed cloud water content is non-zero. This way of defining a cloud core is different to Heus and Seifert (2013) and Dawe and Austin (2012) as no cloud tracking is performed in this study.

In the next step of the local-maximum method, the cloudlets are grown around each *cloud core* following the region growing process described in Heus and Seifert (2013). This region growing process is illustrated schematically in Figure 4.18 (panel a) - d)). Panel a) in Figure 4.18 illustrates a schematic of a subregion of the computational domain with blue boxes illustrating cloudy points ( $w > 1$  m/s, cloud water content non-zero). Red and green boxes denote “cloud cores” identified when searching for local maxima grid points in the vertical velocity field. The first step of the region growing process is illustrated in panel b), where all grid points directly connected to the “cloud core” are marked as cloud/cloudlet with the ID of the associated core points. In panel c) and d) the following region growing process steps are depicted. In each region growing step, all cloudy grid points directly connected to the already labelled cloud points are added to this cloud. The region growing step is repeated until all cloudy grid points connected to a “cloud core” are claimed.

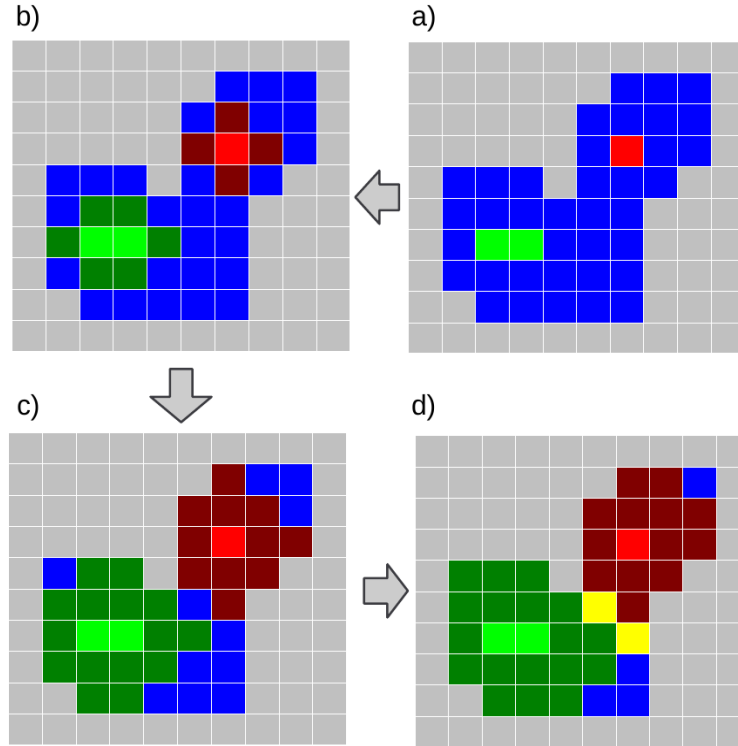


**Figure 4.18:** This schematic illustrates the region growing process applied in the local-maximum method for identifying clouds and cloudlets.

Partitioning large cloud systems into their cloudlets requires all cloudy grid points connected to several cloudlets to be associated with a cloud core. Yellow boxes in Figure 4.18 panel d) illustrate grid points claimed by two or more “cloud cores” within the region growing. To decide which “cloud core” is associated with the cloudy grid point, distances of this grid point to the adjacent cores are computed and weighted with the potential of the cloud cores. The cloudy grid point is then designated to the cloud with the smallest potential weighted distance.

Therefore, applying the local-maximum method partitions large cloud systems into “cloud cores” and their surrounding cloudlets. It is of great interest to gain knowledge how the properties of these cloudlets are distributed in the radiative-convective equilibrium state and whether the tails observed in the distributions are in fact a result of assigning overly connected cloud processes to be one cloud.

### New cloud statistics

Identifying clouds in the computational domain via a simple threshold criterium and assigning all adjacent cloudy grid points to the same cloud, brings forth the risk of artificially merging spatially connected cloud processes with separate cores (cloudlets). With the local-maximum method, cloud cores are identified and the clouds are grown around each core thereby partitioning these large cloud systems into their separate convective processes. The effect of this partitioning on the cloud properties is evaluated hereinafter. Figure 4.19 illustrates the distribution of cloud mass flux derived with the local-maximum method for -4 K/day (top) and -12 K/day (bottom) simulations at 2 km resolution (left) and 125 m resolution (right). Analogously to Figure 4.14, red lines denote least squares best fits and blue lines the maximum entropy fits to the data. It is clear from Figure 4.19 that the distribution resembles an exponential at all resolutions and forcings. Distributions compare well with the exponential fit (red) for the high-resolution simulations over the entire range of radiative cooling rates. The small excess of cloud mass flux observed in the high-resolution simulations compares well to the small excess apparent in the strongly forced 2 km control simulations and results of CC06.

The shape of the distributions at 2 km resolution (left) also compare well with an exponential after applying the local-maximum method. However, a small trend towards weaker and smaller clouds is illustrated in the control simulations. At both forcings the maximum entropy fit slightly overpredicts the large mass flux clouds in the domain. This is due to the local-maximum method separating clouds into their subcloud turbulent processes, not considered deriving the exponential probability density function in CC06. Moreover, clouds were assumed to be non-interacting and sufficiently separated.

In order to gain some further insight on the effect of this partitioning, Figure 4.20 illustrates the “new” distributions of cloud size derived with the local-maximum method analogously to Figure 4.19. It is clear from this figure, that the distribution of cloud size is indeed exponential for all magnitudes of the prescribed cooling and all horizontal resolutions. The exponential least squares fits (red lines) compare very well to the distribution of cloud size at all resolutions and magnitudes of the prescribed forcing. Merely the -12 K/day simulation at 125 m resolution (bottom right) exhibits a very small excess of small clouds. One may assume from this that the exponential is actually a better fit to the cloud size distribution than to the cloud mass flux distribution in these high-resolution simulations after applying the local-maximum method of cloud definition.



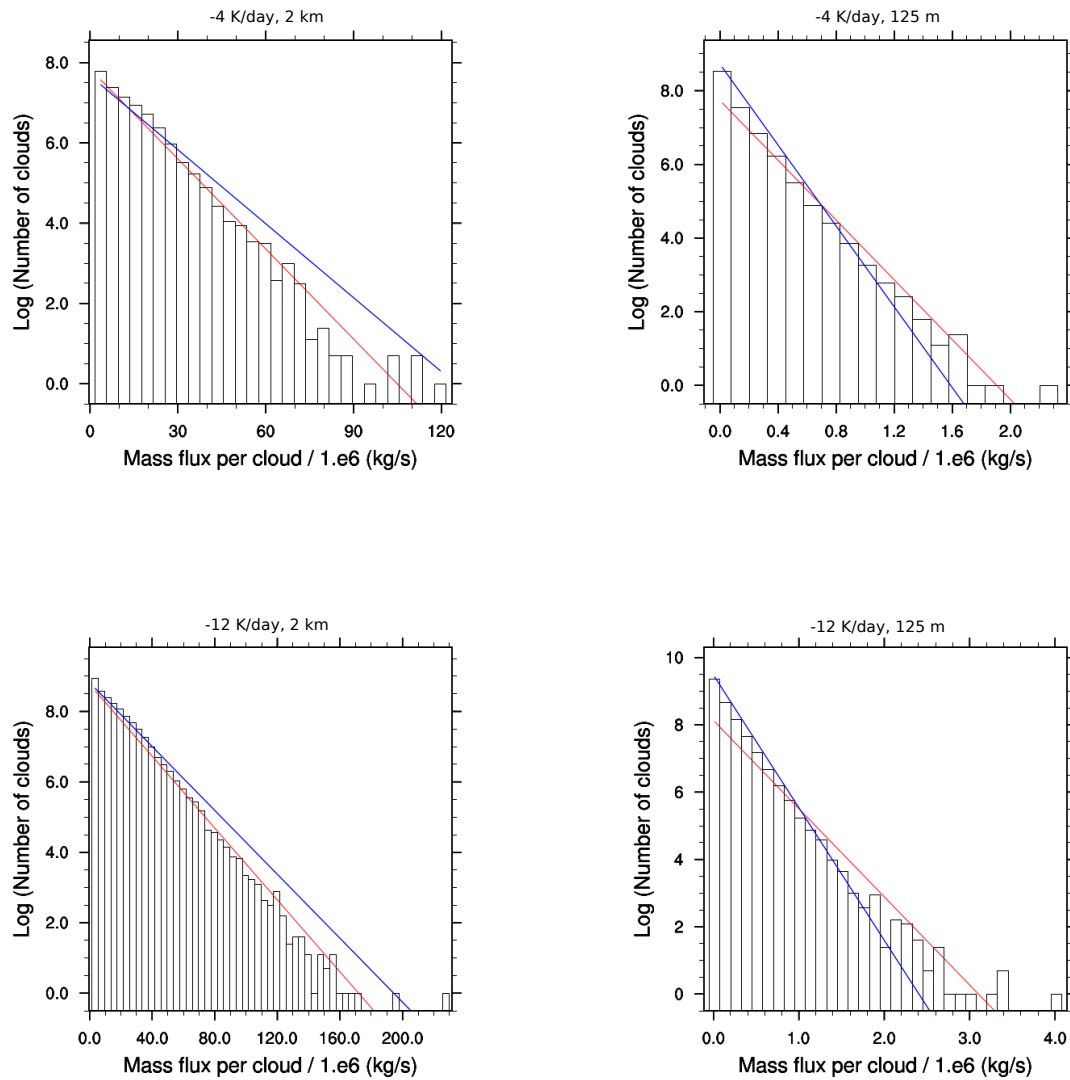


**Figure 4.19:** "New" cloud mass flux distribution for -4 K/day (top) and -12 K/day (bottom) simulations at 2 km (left) and 125 m resolution (right) applying the local-maximum method. Least squares best fit denoted by the red and maximum entropy fit by the blue line.

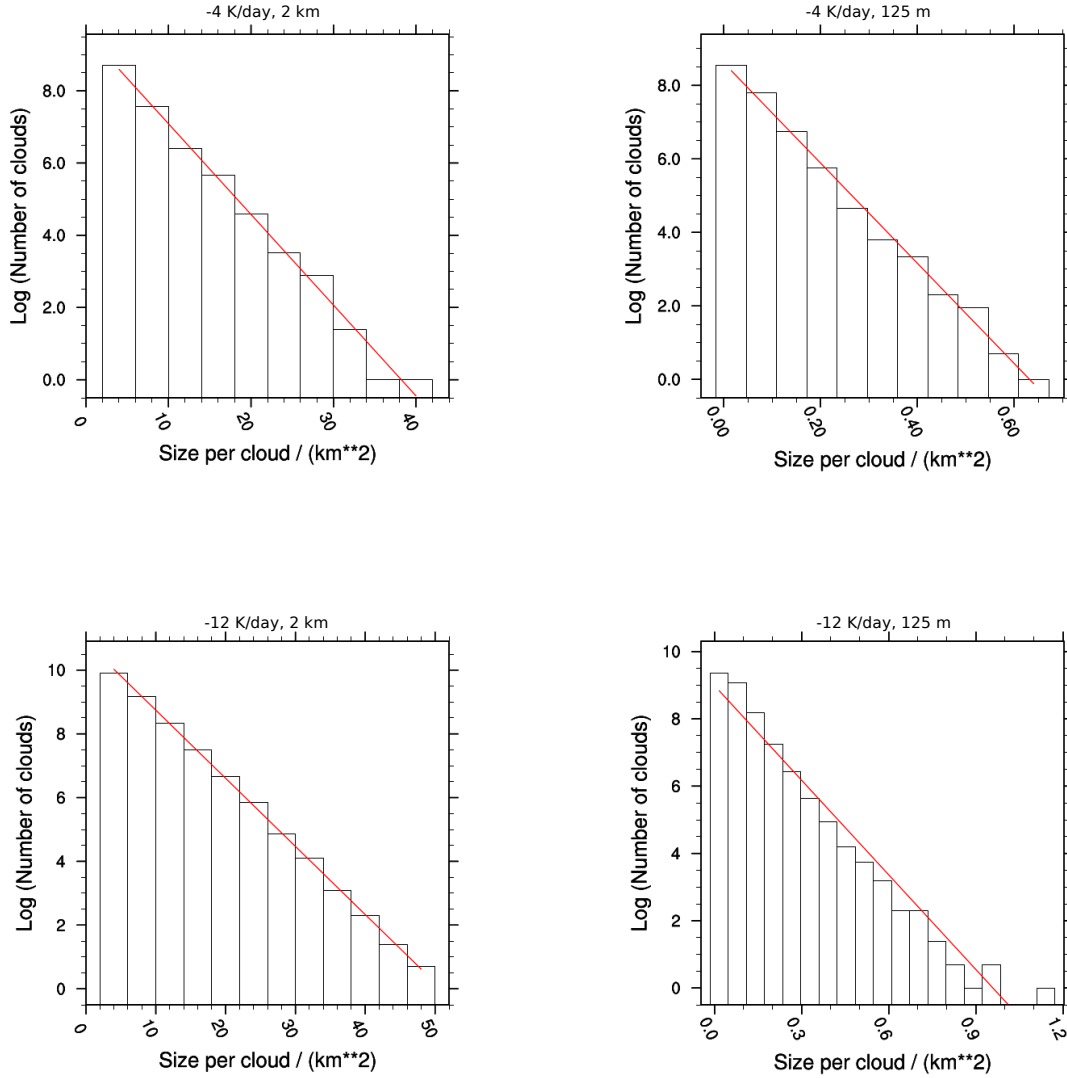


**Figure 4.20:** "New" cloud size distribution for -4 K/day (top) and -12 K/day (bottom) simulations at 2 km (left) and 125 m resolution (right) applying the local-maximum method. Least squares best fit denoted by the red and maximum entropy fit by the blue line.

A strong dependence of cloud statistics on the method of cloud definition for the high-resolutions is observed from Figure 4.19 and 4.20 in this section. To complete the picture, Figure 4.21 illustrates the normalized frequency distribution of cloud vertical velocity derived with the local-maximum method.

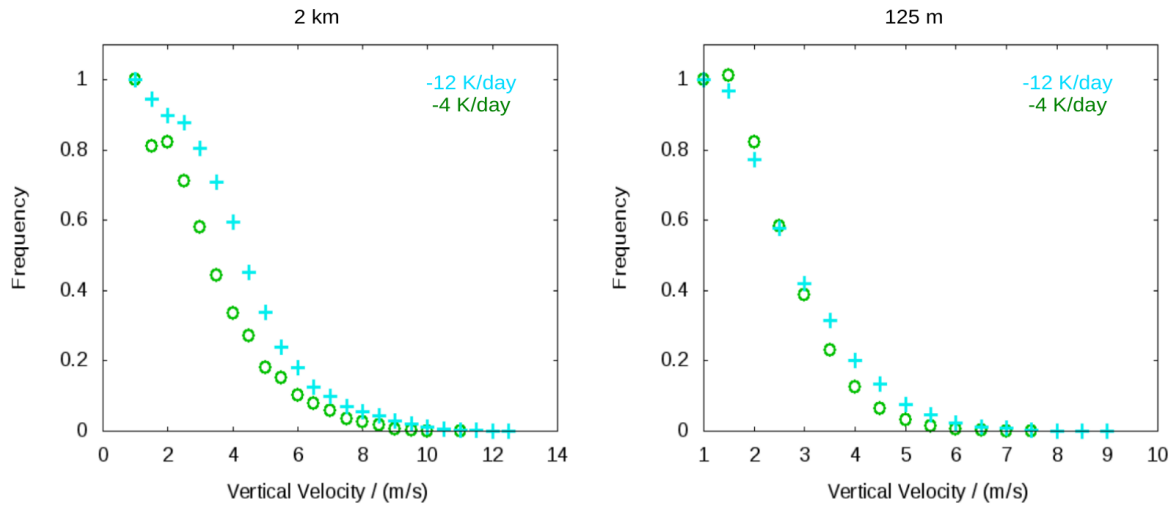


**Figure 4.21:** Vertical velocity per cloud for -4 K/day (green) and -12 K/day (blue) simulation at 2 km (left) and 125 m resolution (right)

First, in comparison to the observed changes in cloud size and cloud mass flux, the general shape of the vertical velocity distribution for the high-resolution simulations, is not significantly affected by differences in the cloud search algorithm. In general the shape of the vertical velocity distributions is comparable for all forcings and resolutions. The coarse resolution, 2 km simulations (left) illustrate slightly larger velocities for the stronger forced simulations than for the weaker ones and a small increase in the width of the distribution with forcing. In contrast, distributions at 125 m resolution (right) compare well at both magnitudes of the prescribed forcing. The width of the distribution however, is found to decrease with increasing resolution resulting in a steeper curve. Furthermore, this figure illustrates the high-resolution probability density maximum at -4 K/day (green) to be located at 1.5 m/s, whereas the maximum is located at 1.0 m/s in lower resolution or stronger forced simulations.

Frequency distributions derived with the local-maximum method compare well to result of the traditional cloud search algorithm (Figure 4.15). Changes occurring with increased resolution or forcing are small compared to changes in cloud size and cloud mass flux. Comparing results for the traditional cloud search algorithm and the local-maximum method, the significant excess of large clouds can be explained by the development of large cloud systems consisting of spatially connected cloudlets with separate cloud cores. Partitioning these cloud systems into their separate, subcloud processes re-established the exponential distributions of cloud size and cloud mass flux. However, when increasing horizontal res-

olution in the simulations from 2 km to 125 m, an increasing dependence of cloud size on the magnitude of the forcing is obtained (widening of the distributions). It is therefore of interest to analyse how cloud properties in general are influenced by the magnitude of the prescribed forcing and whether this scaling is sensitive to changes in the horizontal resolution.

### 4.2.3 Properties of the convective ensemble

#### Sensitivity to horizontal resolution

Analysis of cloud properties earlier in this study, has revealed a strong dependence of the shape of the distributions of cloud size and cloud mass flux on horizontal resolution. This section aims to quantify the sensitivity of cloud and cloud ensemble properties on horizontal resolution and the magnitude of the prescribed forcing. Average cloud and ensemble properties are computed for each magnitude of the forcing and their sensitivity to the horizontal resolution is analysed. Figure 4.22 illustrates the evolution of domain upward mass flux (left) and cloud mass flux (right) with increasing horizontal resolution. Different colours denote different magnitudes of the prescribed forcing. Values are derived with the local-maximum method, however, domain upward mass flux is insensitive to the method of cloud definition and results for the cloud mass flux are comparable (not shown).

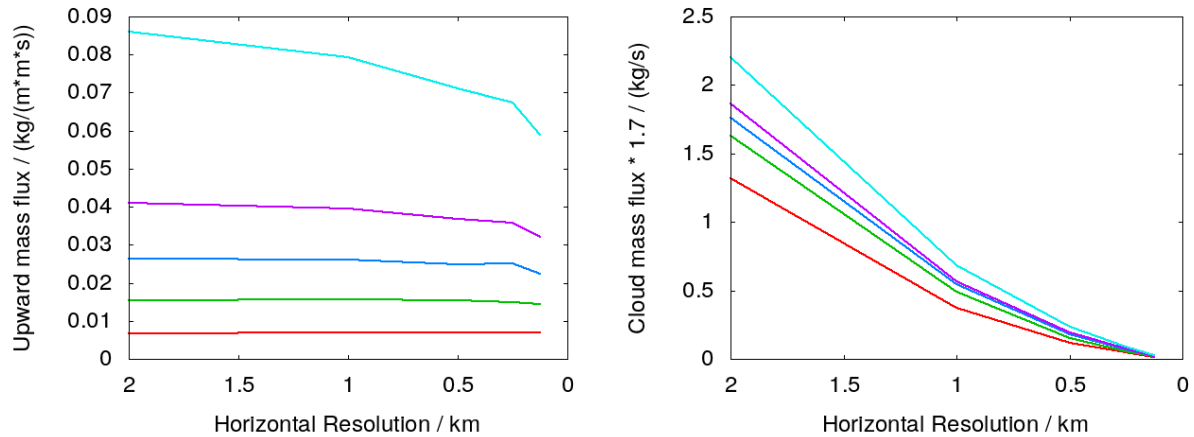


**Figure 4.22:** Domain upward mass flux (left) and cloud mass flux (right) with horizontal resolution for -2 K/day (red), -4 K/day (green), -6 K/day (blue), -8 K/day (purple) and -12 K/day (light blue) simulations, applying the local-maximum method.

As expected from theory and earlier studies, domain upward mass flux is constraint by the magnitude of the prescribed radiative cooling. An insignificant dependence on resolution for the weaker forced simulations is obtained. The -12 K/day (light blue) simulations however, illustrate a decrease of domain upward mass flux with increasing horizontal resolution.

In Chapter 3, evaluating the dependence of upward mass flux on the magnitude of the forcing revealed a decrease of potential temperature lapse rate with increasing forcing for the 2 km control simulations. These changes in stability motivated the computation of an *effective forcing* taking into account the subsequent changes in the stability of the simulated atmosphere. With increasing resolution these deviations of potential temperature lapse rate with increasing forcing are significantly decreasing. Changes in potential temperature lapse rate are directly connected to a change of subsidence warming in the simulated atmosphere. This explains the observed decrease of upward mass flux in Figure 4.22 with increasing horizontal resolution. Thereinafter the originally prescribed magnitude of the radiative forcing is used in this study to evaluate the dependence of cloud and cloud ensemble properties on the magnitude of the forcing. Similar observations are made evaluating the evolution of convective fraction with increasing resolution (not shown).

In contrast to Figure 4.22 (left) and in line with earlier analysis, a significant sensitivity of cloud mass flux to horizontal resolution is depicted in Figure 4.22 (right). Cloud mass flux decreases systematically with increasing resolution for all magnitudes of the prescribed forcing. A stronger decrease is obtained for the stronger forced simulations and a weaker decrease for the weaker ones. At 125 m resolution, cloud mass flux values for the different magnitudes of forcing appear to be converging. Comparable results are obtained for the evolution of cloud size with increasing horizontal resolution (not shown).

With cloud mass flux systematically decreasing and the upward mass flux being constraint by the magnitude of the prescribed forcing, the number of clouds observed in the computational domain is expected to increase significantly to account for the general decrease of cloud mass flux. Figure 4.23 (left) illustrates the number of clouds observed in the domain computed with the traditional method of cloud definition. A strong increase of the number of cloud systems with increasing resolution is obtained for all magnitudes of the prescribed forcing. In addition, one can conclude from the diverging lines that the increase of clouds in the domain is stronger for larger radiative cooling rates than for the smaller ones. Similar results exhibiting a significantly larger number of clouds in each simulation though, are obtained for the local-maximum method of cloud definition (not shown).

As the local-maximum method partitions overly connected clouds into their underlying convective processes, it is of interest whether the number of these subclouds processes increases with increasing resolution as well. Figure 4.23 (right) illustrates the ratio of cloudlets to cloud systems for each radiative cooling rate with increasing horizontal resolution. It is observed in this figure that the ratio of subcloud processes to cloud system compares well for 2 km and 1 km resolution simulations at weaker forcings, whereas a small increase in the number of cloudlets for the -12 K/day simulation (light blue) is depicted. At high-resolutions however, a strong increase of cloudlets compared to the number of cloud systems is observed for all radiative cooling rates. Hence, one can conclude that when applying grid spacings smaller than 1 km more clouds develop in the near cloud environment leading to an increase in overly connected clouds and convective processes clustering in large cloud systems. This tendency grows stronger with further refinement of

the grid spacing and increasing magnitude of the radiative forcing, exhibiting no sign of convergence.

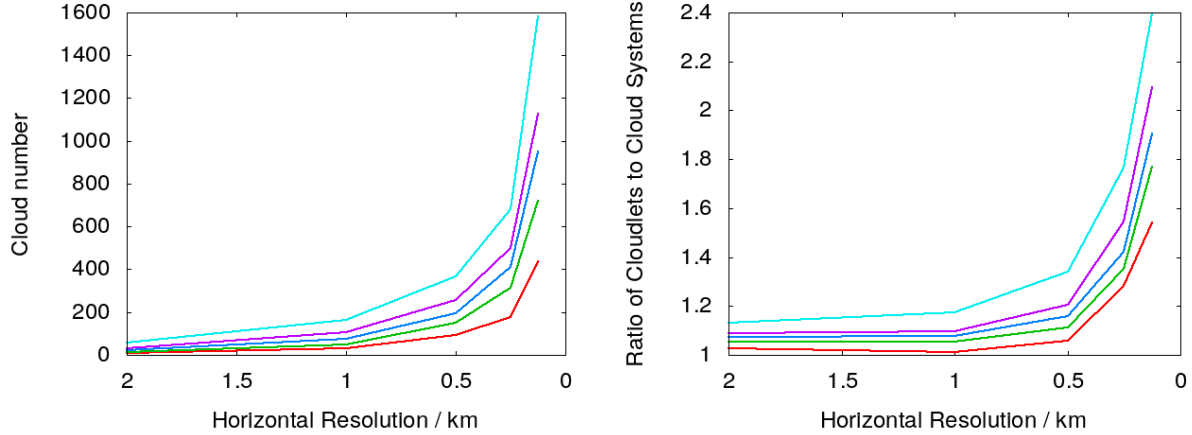


**Figure 4.23:** Number of cloud systems (left - traditional method) and ratio of number of cloudlets to cloud systems (right - ratio of local-maximum to traditional method) with horizontal resolution for -2 K/day (red), -4 K/day (green), -6 K/day (blue), -8 K/day (purple) and -12 K/day (light blue) simulations.

The main limitation when validating the theoretical distribution of cloud mass flux with 2 km horizontal resolution is that the size of the simulated clouds is strongly limited by the grid scale. When analysing resolution dependence of cloud properties, a tendency for cloud and cloudlet size to generally decrease with increasing resolution but increase with the magnitude of the prescribed forcing is observed. To quantify to what extent the size of the grid boxes constraints the observed cloud sizes in the high-resolution simulations, the average number of grid points per cloudlet (local-maximum method) is depicted in Figure 4.24 (left). No significant increase in the number of grid points per cloudlet is illustrated in the coarse resolution, weakly forced simulations. This agrees well with the shape of the cloud size distributions resembling an exponential in the 2 km and 1 km simulations. However, further increasing horizontal resolution results in a significant increase of the number of grid points per cloudlet. This increase of grid points per cloud, combined with the increasing ratio of cloudlets to cloud systems, leads to the impression of well-resolving convective clouds and approaching a large-eddy simulation regime.

Hence, the question is raised how in-cloud properties are affected by better resolving cloud and subcloud processes. Figure 4.24 (right) illustrates the evolution of cloud vertical velocity in the convective updrafts with increasing horizontal resolution (local-maximum method). In general, vertical velocity is found to be rather insensitive to horizontal resolution as well as to the magnitude of the radiative forcing. This observed insensitivity of cloud vertical velocity to the magnitude of forcing is in line with the findings of CC06. Overall cloud average vertical velocities range from 2.5 m/s to 1.5 m/s with maximum values obtained in the 1 km resolution simulations. This maximum is most distinct in the

weaker forced simulations. Exhibiting maximum vertical velocities at 1 km resolution is in line with the findings of Bryan et al. (2003). In addition, the observed vertical velocity maximum at a resolution of 1 km is consistent with first resolving the energy maximum in the vertical velocity spectra (Figure 4.11). Further increasing horizontal resolution then merely adds smaller, less energetic wavelengths to the energy spectrum.

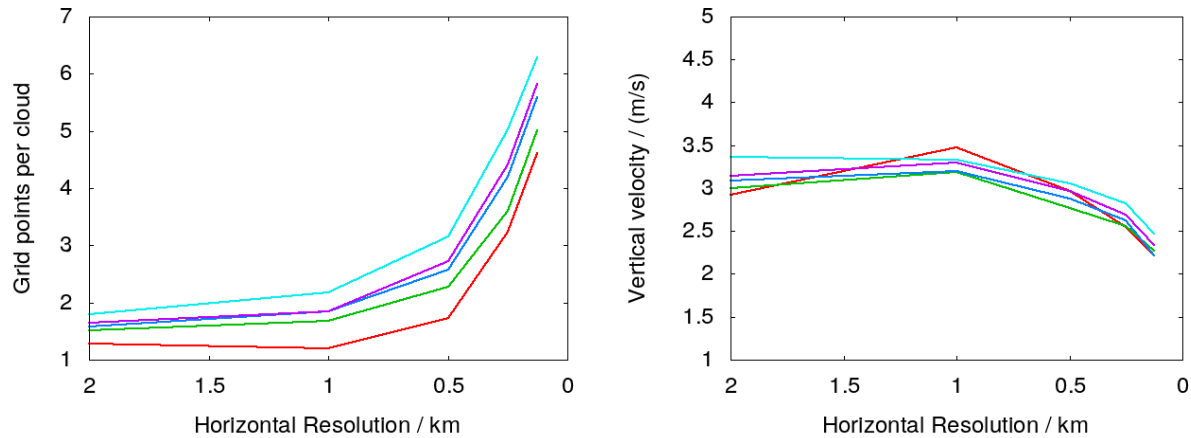


**Figure 4.24:** Average number of grid points per cloud/cloudlet (left) and cloud vertical velocity (right) with horizontal resolution for -2 K/day (red), -4 K/day (green), -6 K/day (blue), -8 K/day (purple) and -12 K/day (light blue) simulations. Results are derived with the local-maximum method.

In general slightly smaller velocities are obtained for the weaker forced simulations than for the stronger forced ones and a small decrease of velocities with increasing horizontal resolution is apparent. However, changes in vertical velocity are small compared to changes in cloud size and cloud mass flux.

### Sensitivity to radiative cooling

In addition to the dependence of clouds and cloud ensembles on the horizontal resolution, the preceding analysis has revealed a dependence of cloud and ensemble properties on the magnitude of the prescribed forcing. This is in line with expectations from theory, earlier studies (CC06) and the control simulation results (Chapter 3). To complete the picture, this section evaluates the scaling of cloud and ensemble properties with the prescribed forcing and how this scaling depends on the grid spacing.

Figure 4.25 illustrates dependence of the domain upward mass flux (left) and convective fraction (right) on the magnitude of the forcing at different horizontal resolutions. Different colours and point styles denote different resolutions. Linear best fits are computed for each grid spacing (lines). Linear scaling of upward mass flux with radiative cooling is expected as the amount of convective transport in the domain is constrained by the amount of subsidence warming and thereby directly linked to the magnitude of the forcing. Analysing the 2 km control simulations in Chapter 3, the potential temperature lapse rate in the

atmosphere is found to change with respect to a moist adiabat with increasing magnitude of the radiative cooling rate. It is clear from this figure that the curvature obtained in the 2 km control simulations (Chapter 3) is vanishing with increasing horizontal resolution. In the high-resolution simulations, domain upward mass flux does indeed scale linearly with the magnitude of the prescribed forcing. Similar observations are made for the scaling of convective fraction with the prescribed radiative forcing (Figure 4.25 right).

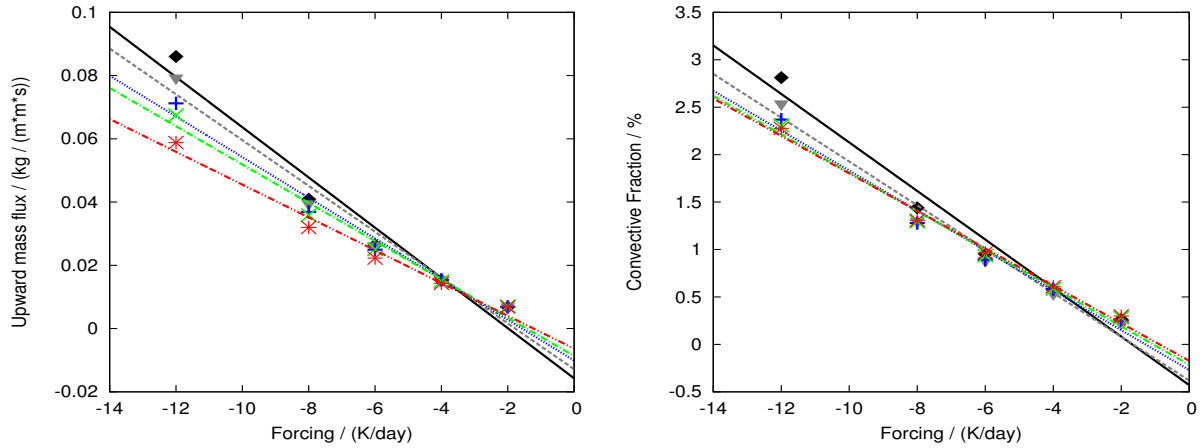


**Figure 4.25:** Scaling of domain upward mass flux (left) and convective fraction (right) with radiative cooling. Lines denote the best fit to the data points for each resolution. Colours denote resolutions of 2 km (solid black), 1 km (dashed grey), 500 m (dotted blue), 250 m (dashed-dotted green) and 125 m (dashed-dotted-dotted red). Results are derived with the local-maximum method.

Good agreement of the convective fraction is obtained between the 250 m and 125 m simulations in this figure, whereas the domain upward mass flux is found to decrease slightly from 250 m to 125 m in the strongly forced simulations. Changes of upward mass flux and convective fraction with resolution are small compared to changes with increasing magnitude of the prescribed forcing though.

Different behaviour is expected from the evolution of cloud number with increasing resolution. Previous analysis of horizontal cross-sections of the convective cloud field has already revealed an increasing number of clouds with increasing resolution due to the limitation of cloud size by the grid scale. Scaling of the average cloud number with the magnitude of the forcing is illustrated in Figure 4.26 derived with the traditional method (left) and the local-maximum method (right). Both methods illustrate a strong increase of cloud and cloudlet number in the domain with increasing forcing and horizontal resolution. Scaling of cloud number with the magnitude of the forcing is linear for all grid spacings. This is in line with the control simulation results (Chapter 3) and previous studies (CC06). The increase of cloud number with increasing magnitude of the prescribed forcing is intensifying with increasing horizontal resolution. This is obtained from the increasing slope of the best fit lines with increasing resolution in Figure 4.26.



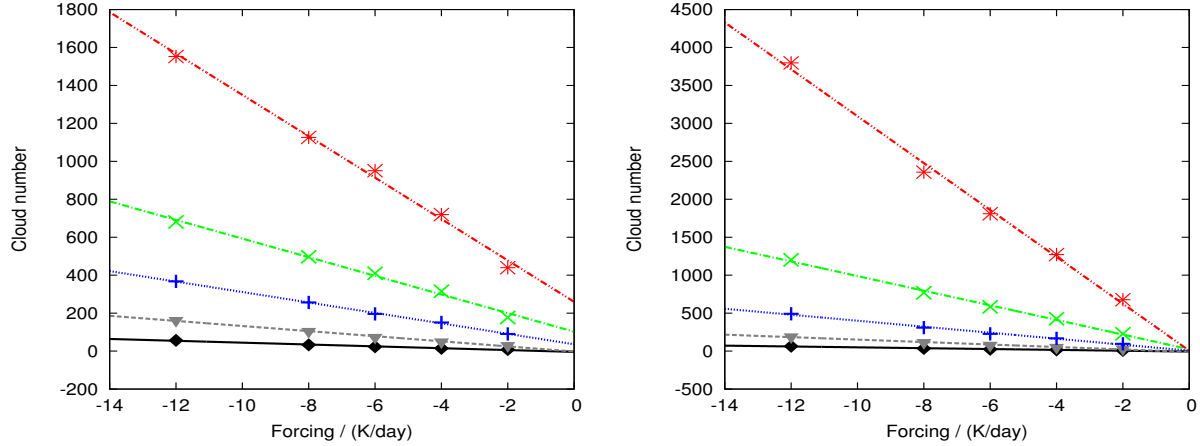


**Figure 4.26:** Average number of clouds in the domain for traditional method (left) and local-maximum method (right) scaling with radiative forcing. Lines denote the best fit to the data points. Colours denote resolutions of 2 km (solid black), 1 km (dashed grey), 500 m (dotted blue), 250 m (dashed-dotted green) and 125 m (dashed-dotted-dotted red).

Comparing results of the two methods of cloud definition, the number of cloudlets (right) exhibits an even stronger dependence on horizontal resolution and magnitude of the forcing than the number of cloud systems (left). Hence, one can conclude that the number of resolved, subcloud processes within the large cloud systems is increasing when refining the grid spacing and hereby better resolving the turbulent mixing. Further analysis of cloud and cloud ensemble properties with horizontal resolution are undertaken by applying the local-maximum method. Results derived with the traditional search algorithm compare well to the local-maximum method results, even though absolute values of the ensemble-average properties differ in a direct comparison.

Figure 4.27 depicts the relationship between the forcing, cloud size (left) and the number of grid points per cloud (right) derived with the local-maximum method. Cloud size systematically decreases with increasing resolution and approximately linear with the magnitude of the prescribed forcing. The largest decrease in cloud size is obtained when increasing horizontal resolution from 2 km to 1 km. Cloud sizes appear to be converging at high-resolutions. It has been obtained in the previous section that even though cloud size systematically decreases, the number of grid points per cloud systematically increases with resolution (see Figure 4.24 left). Scaling of the number of grid points per cloud with the magnitude of the prescribed forcing is denoted in Figure 4.27 (right) and found to be approximately linear at all resolutions. However, some changes with resolution are apparent.

Increasing horizontal resolution from 2 km to 500 m increases the number of grid points per cloud and in addition, increases the slope of the best fit lines. In contrast, 250 m and 125 m simulations exhibit comparable slopes. Hence, scaling of the number of grid points

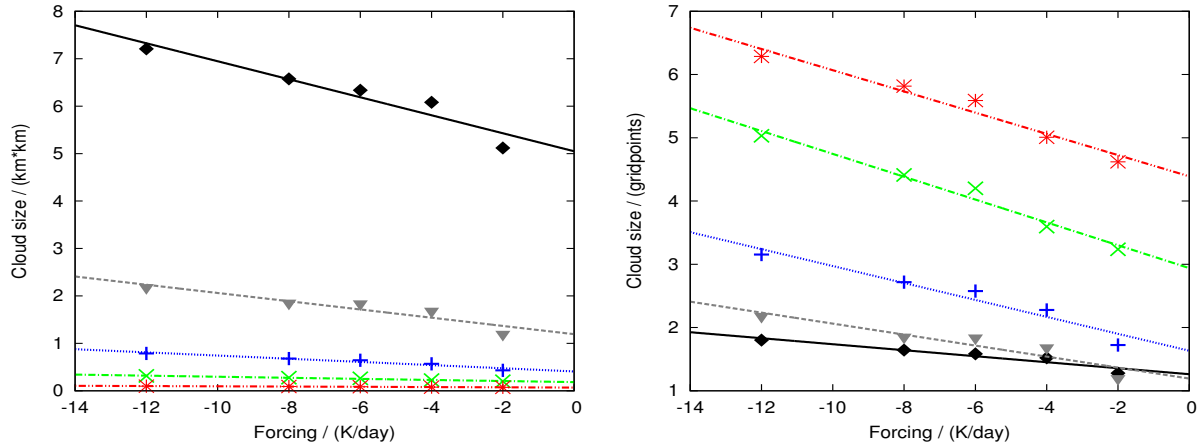


**Figure 4.27:** Average cloud size (left) and number of grid points per cloud (right) scaling with radiative forcing. Lines denote the best fit to the data points. Colours denote resolutions of 2 km (solid black), 1 km (dashed grey), 500 m (dotted blue), 250 m (dashed-dotted green) and 125 m (dashed-dotted-dotted red). Results are derived with the local-maximum method.

per cloud with the forcing does in fact depend on the horizontal resolution. Convergence of the slopes of the best fits can be observed in the high-resolution simulations. The increase of the number of grid points per cloud is owed to better resolving in-cloud turbulent processes at high-horizontal resolutions. Similar to cloud sizes in Figure 4.27 a decrease of cloud mass flux with increasing magnitude of the prescribed forcing and horizontal resolution is illustrated in Figure 4.28 (left). Scaling of cloud mass flux with the magnitude of the forcing is found to be approximately linear at all horizontal resolutions. It is apparent that the fluctuations of the cloud size and cloud mass flux values around their best fits are comparable (Figure 4.27 left, Figure 4.28 left).

One can therefore conclude that changes in cloud mass flux with increasing resolution are primarily constrained by changes in the size of the clouds. Vertical velocity per cloud in contrast, is expected to be rather insensitive to changes in the magnitude of the prescribed forcing (Figure 4.28 right). Indeed, it is clear from this figure that cloud vertical velocity is quite independent of the forcing. In line with the analysis of Figure 4.21 earlier in this chapter, a small trend towards lower vertical velocities with increasing resolution is obtained from this figure. However, these changes are small compared to changes in cloud size and cloud mass flux with increasing horizontal resolution.

From this analysis it can be concluded that the scaling of cloud properties with the magnitude of the prescribed forcing is approximately linear regardless of the horizontal resolution. A strong dependence of cloud size, cloud mass flux and the number of clouds on the horizontal grid spacing and the magnitude of the prescribed forcing is obtained. The strength of the convective clouds however, in terms of updraft vertical velocity, is not significantly influenced by neither the magnitude of the forcing nor the grid spacing.

In previous analysis of horizontal cross-sections of the vertical velocity field a tendency of

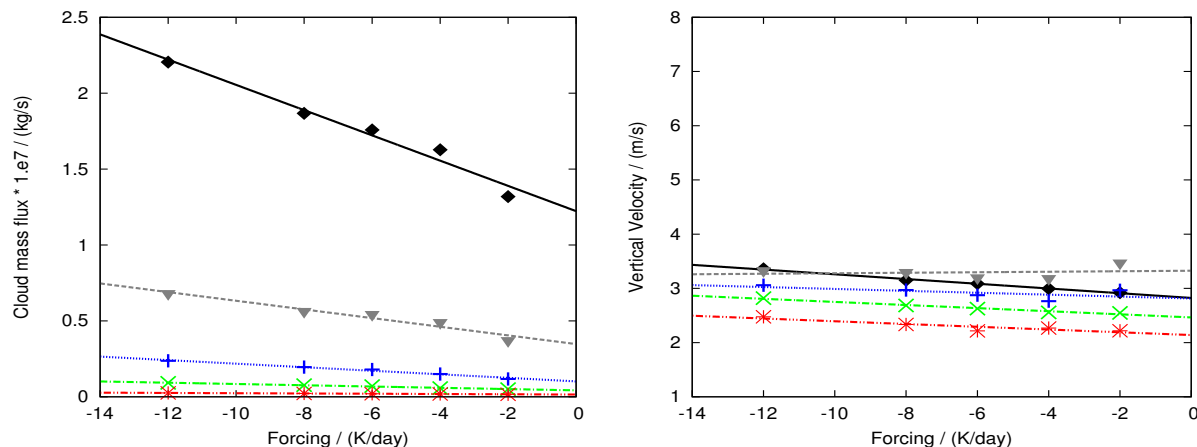


**Figure 4.28:** Cloud mass flux (left) and vertical velocity per cloud (right) scaling with radiative forcing. Lines denote the best fit to the data points. Colours denote resolutions of 2 km (solid black), 1 km (dashed grey), 500 m (dotted blue), 250 m (dashed-dotted green) and 125 m (dashed-dotted-dotted red). Results are derived with the local-maximum method.

convective clouds to appear in large cloud clusters is observed. Further evaluation of this change in the structure of the cloud field is undertaken in the next section.

## 4.3 Resolution dependence of the cloud field

### 4.3.1 Cloud number and mass flux density

Previous analysis in this chapter illustrated cloud size to systematically decrease with increasing resolution. The number of grid points per cloud however, was found to increase with increasing horizontal resolution. In addition, spatial clustering of the convective clouds in the domain develops with increasing horizontal resolution. In the high-resolution simulations small convective clouds are found to organise in band-like structures around cloud-free areas. The tendency of convective clouds to organise in these cloud clusters and the dependence on the magnitude of the prescribed forcing and horizontal resolution is analysed hereinafter. Cloud number densities and cloud mass flux densities are evaluated as a function of distance to cloud center analogously to the computations for (Figure 3.17) in Chapter 3 (control simulations). Mean cloud number is calculated in annular regions surrounding each cloud as denoted in the schematic of Figure 3.16 (Chapter 3). Cloud number is multiplied with the distance to cloud center and weighted with the number of grid points and the size of each annular region. Rescaled cloud number density and its sensitivity to grid spacing and the magnitude of the prescribed forcing is illustrated in Figure 4.29 for -4 K/day (top) and -12 K/day simulations (bottom). Analogously, Figure 4.30 denotes the rescaled upward mass flux density with distance to cloud center. Cloud number and upward mass flux densities derived with the traditional search algorithm are denoted in the left panels (TR) and results of the local-maximum method are illustrated in the right

panels (LM). Different line styles and colours denote the different horizontal resolutions.

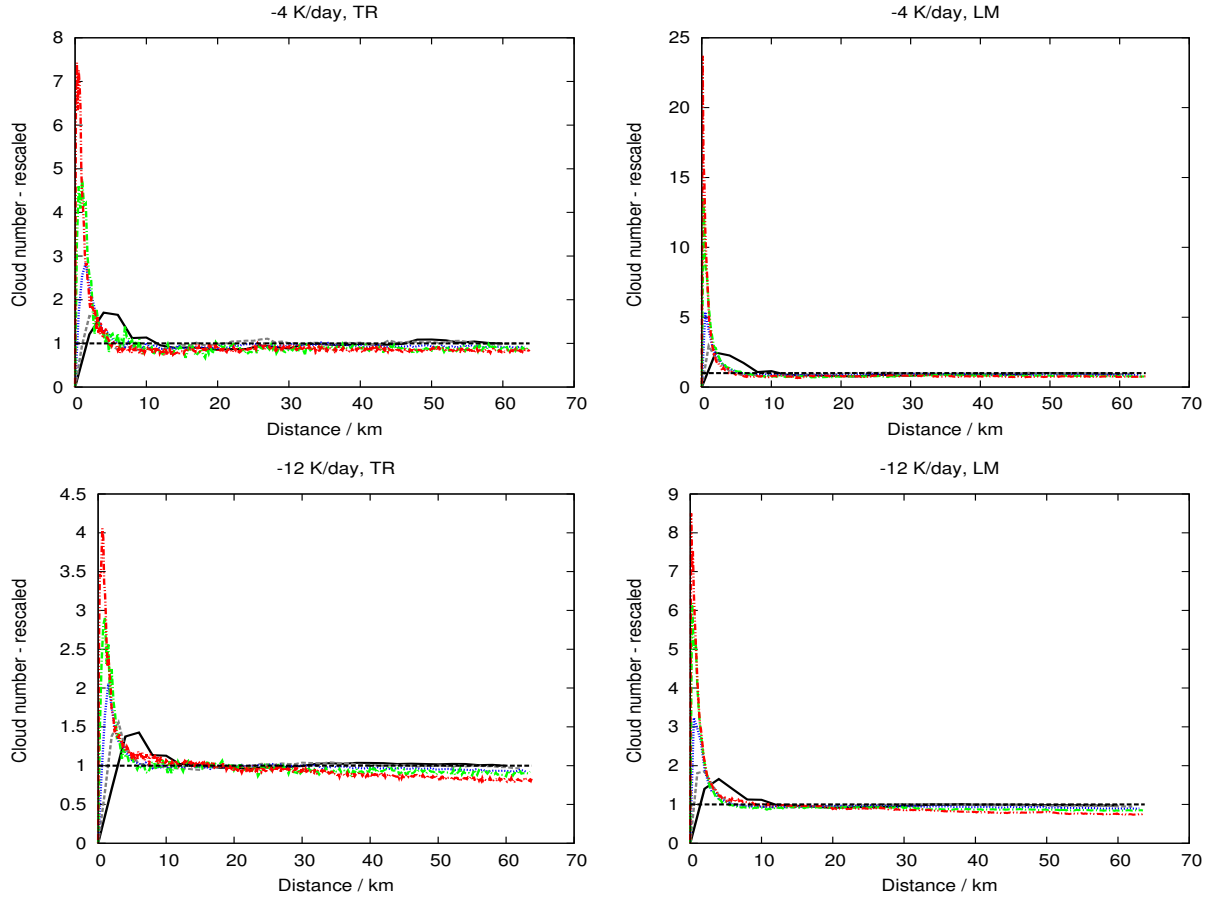


**Figure 4.29:** Rescaled cloud number density for -4 K/day (top) and -12 K/day simulations (bottom) with the traditional cloud search algorithm (TR) and the local-maximum method (LM). Colours denote resolutions of 2 km (solid black), 1 km (dashed grey), 500 m (dotted blue), 250 m (dashed-dotted green) and 125 m (dashed-dotted-dotted red).

Both figures reveal that clustering in the near cloud environment increases systematically with increasing horizontal resolution as the magnitude of the density maxima increases with increasing resolution. This is observed over the entire range of the prescribed forcings and for both methods of cloud definition. In contrast, a similar position and comparable width of the density maxima is obtained for all grid spacings finer than 2 km (black). Significant differences are apparent comparing high-resolution cloud number and mass flux densities to the results of the 2 km control simulations. Cloud number densities in the 2 km simulations (black) are significantly smaller and the density maxima are wider and occur at a greater distance from cloud center. A convective inhibition range is obtained at distances between 10 km and 25 km in these coarse resolution simulations. This is in line with the findings of CC06.

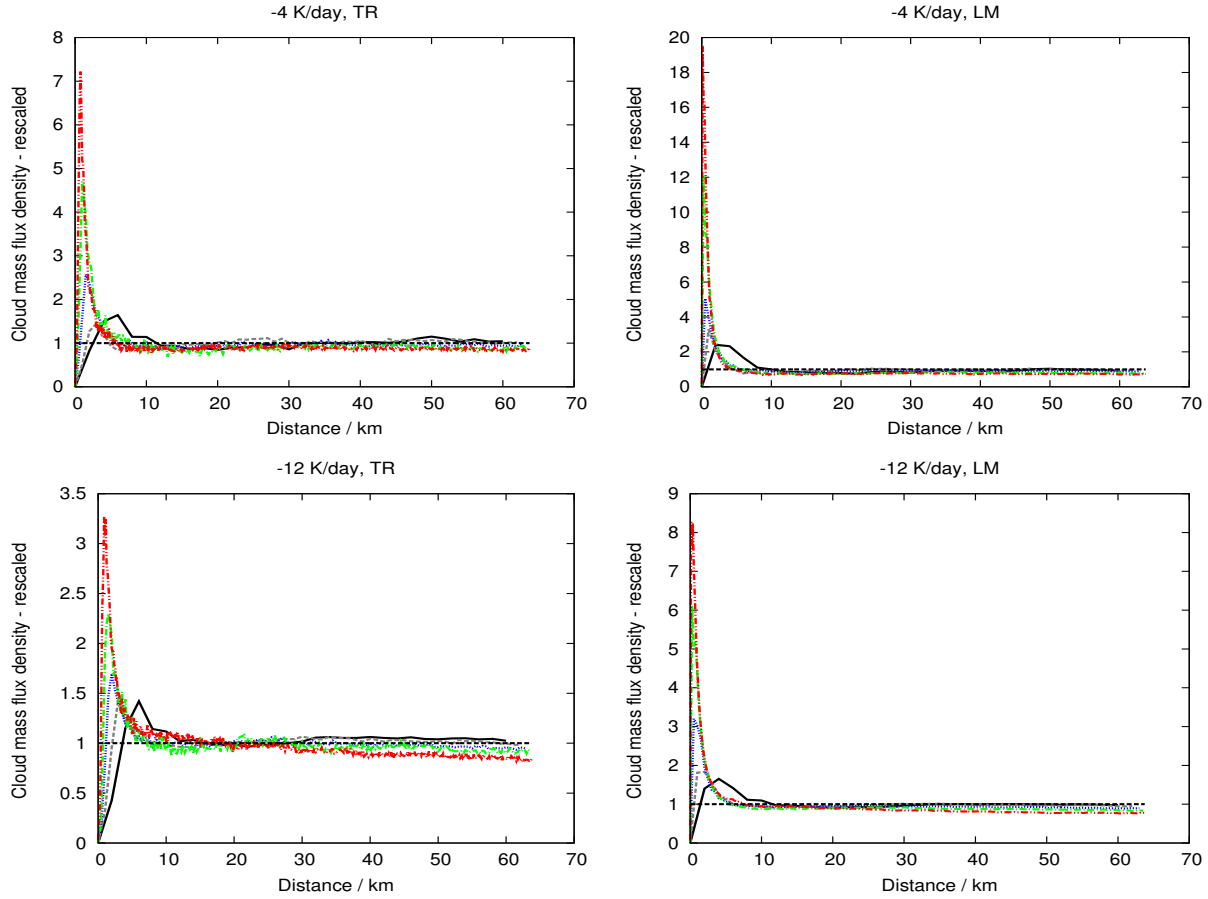


**Figure 4.30:** Rescaled mass flux density for -4 K/day (top) and -12 K/day simulations (bottom) for the traditional cloud search algorithm (TR) and the local-maximum method (LM). Colours denote resolutions of 2 km (solid black), 1 km (dashed grey), 500 m (dotted blue), 250 m (dashed-dotted green) and 125 m (dashed-dotted-dotted red).

In the 1 km resolution simulations (grey), the position of the observed density maximum moves closer towards the cloud center and is comparable to the density maxima observed in the high-resolution simulations. The magnitude of the 1 km density maximum however, is still comparable to the 2 km results (black). A convective inhibition range is apparent in the 1 km cloud number and mass flux densities analogously to the 2 km control simulations (black). At distances greater than 20 km from cloud center these coarse resolution simulations reveal a randomly distributed cloud field, indicated by the rescaled density values fluctuating around a value of one.

Further increasing horizontal resolution reveals a systematic increase of the maximum density values with increasing horizontal resolution. In the -4 K/day simulations (top) the width of the density maxima is comparable at higher resolutions and for both methods of cloud definition. Similar observations are made at 500 m (blue) and 250 m resolution (green) in the -12 K/day simulations (bottom). However, the high-resolution, 125 m sim-

ulation (red) for the stronger forced simulations (bottom) reveals the width of the density maximum to be slightly larger than in the coarser resolution or weaker forced simulations. At distances greater than 20 km from cloud center, these localised clustering effects then turn into an increasing trend of spatial regularity in the cloud field.

In general this tendency of spatial regularity was obtained in the coarse resolution simulations as well and increases with increasing horizontal resolution in Figure 4.29 and Figure 4.30 for the entire range of prescribed forcings and both methods of cloud definition. Comparing different magnitudes of the prescribed forcing, both figures reveal a decreasing magnitude of the rescaled cloud number and mass flux densities with increasing magnitude of the prescribed forcing. This may be owed to cloud sizes generally increasing with the magnitude of the prescribed forcing and hereby partially accounting for the increasing size of the cloud clusters. Rescaled densities of cloud number and cloud mass flux derived with the traditional search algorithm and the local-maximum method of cloud definition are comparable in terms of shape and position of the density maxima. However, total values of the rescaled cloud number and mass flux densities are larger for the local-maximum method due to the partitioning of large clouds into their single updrafts. Further analysis of the structure of the cloud fields is undertaken in the next section.

### 4.3.2 Cloud number and mass flux variance

Further knowledge about the structure of the cloud field can be gained by analysing variances of cloud number and the upward mass flux as a function of the inverse number of clouds in the domain. As described in Chapter 3, variances are derived partitioning the domain into differently sized subdomains. Cloud number and mass flux variances are computed within these subdomains and plotted as functions of the associated inverse number of clouds in the domain. Figure 4.31 illustrates variances of cloud number in the -4 K/day simulations (top) and -12 K/day simulations (bottom) derived with the traditional method (TR) of cloud definition (left) and the local-maximum (LM) method (right). Figure 4.32 analogously to Figure 4.31 exhibits the variances of upward mass flux as a function of the inverse cloud number in the subdomains. Different point styles and colours denote different horizontal resolutions in both figures. The corresponding theoretical predictions of a randomly distributed cloud field are denoted by the grey lines with a slope of  $2^{1/2}$ .

Keeping in mind that higher values of the inverse number of clouds ( $\sqrt{1/\langle N \rangle}$ ) correspond to fewer clouds in the subdomain, these figures illustrate a development of cloud clustering in the computational domain with increasing horizontal resolution. Signs of convective organisation are apparent for both methods of cloud definition and all magnitudes of the prescribed radiative cooling. Variances of cloud number and mass flux are comparable. The tendency of convective clouds to organise in clusters is found to increase strongly with increasing resolution and magnitude of the prescribed forcing. For the coarser resolution simulations all variances are located below the dotted line representing a randomly distributed cloud field as assumed in deriving the theory. A small trend of spatial regularity in these coarse resolution cloud fields is obtained, increasing systematically with the

size of the subdomain.

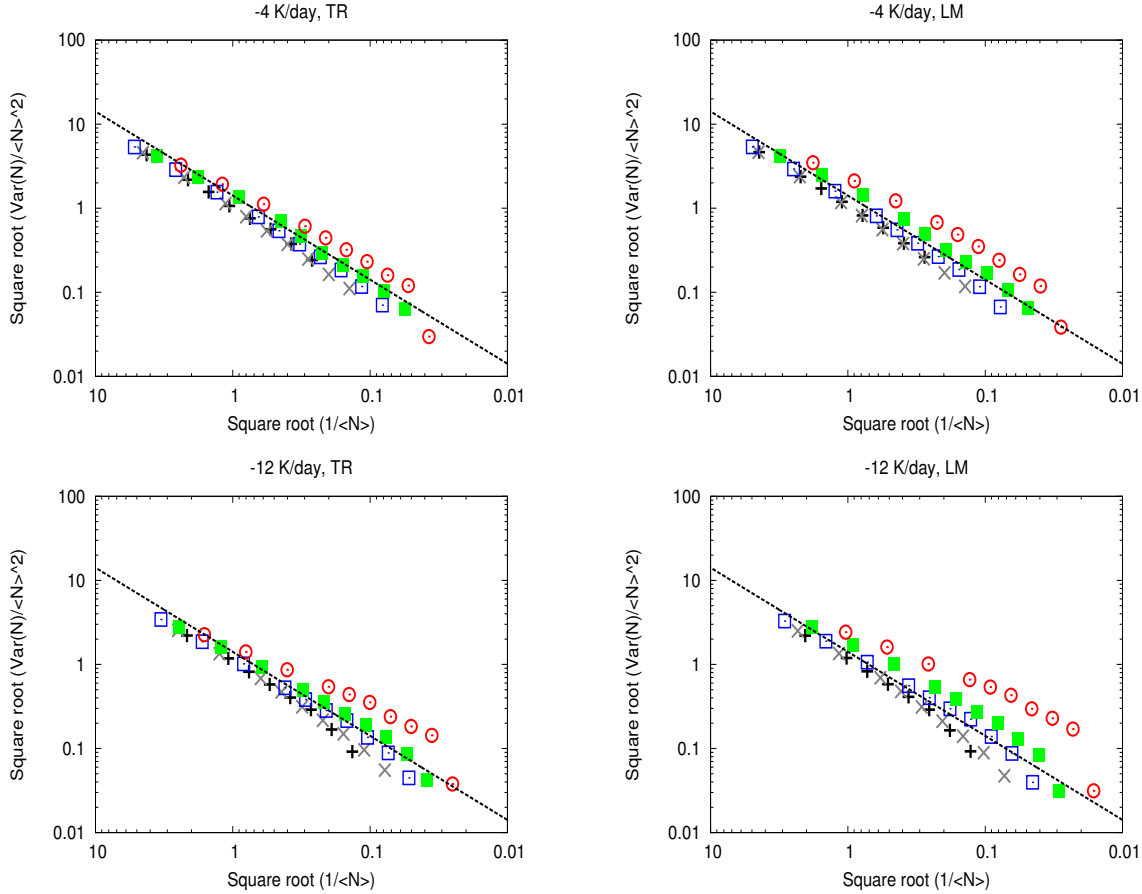


**Figure 4.31:** Variances of cloud number for -4 K/day (top) and -12 K/day simulations (bottom) for the traditional search algorithm (left) and the local-maximum method (right). Colours denote horizontal resolutions of 2 km (black cross), 1 km (grey x), 500 m (blue box empty), 250 m (green box full) and 125 m (red circle).

With increasing resolution, cloud number and mass flux variances then exhibit a clear trend towards clustering. Whereas the 500 m simulations (blue boxes) yield variances slightly smaller than the random distribution for the weaker forced simulations and slightly larger for the stronger forced ones, results of the 250 m simulations (green boxes) denote a clear sign of clustering in the domain. Variances at a grid spacing of 125 m (red circles) are located above the random distribution line for almost all subdomain sizes, exhibiting significantly larger variances than a random distribution would.

In general cloud number and cloud mass flux variances are found to increase with the size of the subdomain and decrease again for the largest subdomains. This behaviour is most significant in the high-resolution, 125 m simulations (red circles). Cloud number and mass flux variances increase approximately linearly with increasing size of the subdomains in the high-resolution simulations. However, significantly lower values are obtained comput-

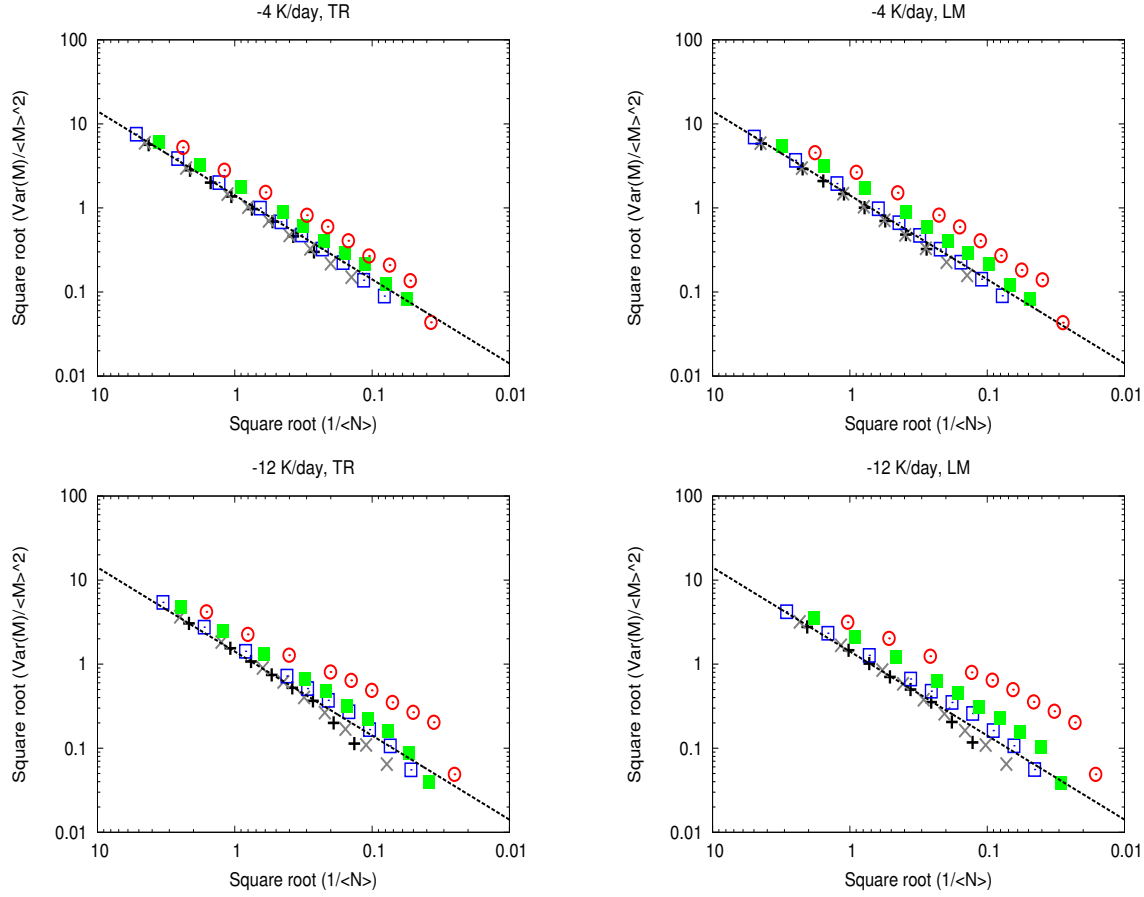


**Figure 4.32:** Variances of upward mass flux for -4 K/day (top) and -12 K/day simulations (bottom) for the traditional search algorithm (TR) and the local-maximum method (LM). Colours denote horizontal resolutions of 2 km (black cross), 1 km (grey X), 500 m (blue box empty), 250 m (green box full) and 125 m (red circle).

ing cloud number and upward mass flux variances over the entire computational domain. Comparing the two methods of cloud definition, variances based on the local-maximum method (LM) generally exhibit larger values due to the partitioning of clouds and cloud systems into their underlying convective processes. These findings are in line with observations made in the analysis of cloud number and mass flux densities in Figure 4.29 and Figure 4.30.

**Concluding remarks** In this chapter, evaluating the sensitivity of cloud-resolving simulations to the grid spacing reveals a strong sensitivity of cloud properties and the structure of the cloud field on the horizontal resolution. Cloud sizes and cloud mass fluxes decrease systematically with increasing horizontal resolution. In contrast, the number of clouds in the domain increases with resolution for all magnitudes of the prescribed forcing. Clustering tendencies in the cloud fields are increasing with the magnitude of the prescribed



forcing as well as the horizontal resolution. However, the area surrounding a cloud affected by this clustering is independent of changes in resolution and forcing. In the next chapter, results will be discussed in detail and compared to the theoretical expectations and results of earlier studies. Limitations of this work will be described and an outlook of further work will be given.



# Chapter 5

## Summary and discussion

Correctly representing interactions and effects of deep moist convection in the earth's atmosphere is a key issue in numerical simulations with meteorological applications. The goal of this thesis is to evaluate whether a theoretical model describing the convective variability within a cumulus cloud ensemble is valid at high horizontal resolutions. This theoretical model, describing the frequency distribution of cloud vertical mass flux was derived in Craig and Cohen (2006) (CC06 a) and validated in 2 km resolution simulations in Cohen and Craig (2006) (CC06 b). In the first part of this study, results of CC06 (b) are reproduced applying a grid spacing of 2 km in three-dimensional simulations of a cloud ensemble in a state of radiative-convective equilibrium (control simulations). Sensitivity of the simulated cloud ensemble to the magnitude of the prescribed forcing is evaluated following CC06 (b). Five different radiative cooling rates are applied to analyse the dependence of cloud and ensemble properties on the magnitude of the prescribed forcing. In the second part of this study the set of control simulations is repeated, stepwise refining the horizontal resolution from 2 km to 125 m in steps of 1 km, 500 m and 250 m. Dependence of the variability within the convective cloud ensembles on the grid spacing is analysed and sensitivity of cloud and ensemble properties to the grid spacing and magnitude of the prescribed forcing is evaluated in these high-resolution simulations.

**Reproducing results of CC06** In the first part of this study a set of simulations at a horizontal resolution of 2 km is performed to validate the exponential probability density function of cloud mass flux predicted in the theoretical model of CC06 (a) and to reproduce the results of the 2 km resolution simulations in CC06 (b). Cloud size and cloud mass flux probability density functions are found to compare well to the theoretical predictions of CC06 (a) as well as to results of the 2 km resolution simulations of CC06 (b). Hence, the expected, exponential distribution of cloud size and vertical mass flux is successfully reproduced over a wide range of forcings and height levels in the 2 km resolution control simulations though. In line with the findings of CC06 (b) increasing the magnitude of the prescribed forcing significantly increases the number of clouds in the domain, whereas cloud properties like size and updraft velocity are found to be rather insensitive to changes of the prescribed forcing.

A linear increase of the domain upward mass flux with the magnitude of the prescribed forcing was observed in CC06 (b), however domain upward mass flux is not found to scale linearly in the 2 km control simulations. As noted in Chapter 3 (Equation 3.2) the radiative cooling in the domain is balanced by adiabatic warming associated with subsidence in the cloud-free areas. Due to continuity the subsidence mass flux then determines the total upward mass flux in the clouds and the upward mass flux is linearly proportional to the prescribed cooling if the potential temperature lapse rate is insensitive to changes in the prescribed forcing, as was the case in CC06 (b). Evaluating the relationship between domain upward mass flux and the radiative forcing reveals a stronger increase than the expected linear one with increasing magnitude of the forcing. Associated with this, a decreasing potential temperature lapse rate is observed. An effective forcing is computed by weighting the prescribed forcing with the decreasing potential temperature lapse rate. Domain upward mass flux is found to increase linearly with this effective forcing, demonstrating that the physical basis for control of the mass flux remains unchanged although the linear relationship is not found.

One can therefore conclude that the results of CC06 (b) are successfully reproduced with the numerical fluid solver EULAG at a grid spacing of 2 km. Small differences between this study and CC06 (b) are owed to the decreasing stability with increasing magnitude of the prescribed forcing within the 2 km control simulations.

## Stepwise increasing horizontal resolution

In the second part of this study, sensitivity of the 2 km control simulation results to the grid spacing is evaluated over the full range of prescribed radiative cooling rates. Overall, a small but systematic shift of the simulated equilibrium states is observed when stepwise increasing horizontal resolution. First, the simulated atmospheric states develop to be drier and warmer for higher resolutions. Second, increasing horizontal resolution and thereby better resolving turbulent structures leads to a better resolved boundary layer and a stronger shallow convective layer. Observed changes of the mean atmospheric states with increasing horizontal resolution are small though, compared to the systematic shift obtained when increasing the magnitude of the prescribed forcing.

**Response to changes in the magnitude of the forcing** In this paragraph the influence of the prescribed forcing on the simulated cumulus clouds and cloud ensembles is discussed. Linear scaling of cloud and ensemble averaged properties is obtained in the 2 km control simulations after the computation of an *effective forcing* motivated by increasing deviations from a moist adiabat. These stability differences within the 2 km control simulations are found to decrease systematically with increasing horizontal resolution. The computation of an *effective forcing* is therefore not necessary in the high-resolution simulations in this study. Scaling of cloud and ensemble averaged properties with the magnitude of the prescribed forcing is discussed hereinafter. As expected from theory and the 2 km

control simulations, an increase in the magnitude of the prescribed forcing primarily increases the number of clouds in the domain without significantly changing the average cloud properties. The linear scaling of cloud number with the magnitude of the forcing is found to be robust over the entire range of grid spacings applied in this resolution sensitivity study. The slope of the best fit lines when analysing this scaling however, steepens with increasing horizontal resolution. This indicates a stronger dependence of cloud number on the magnitude of the prescribed forcing with increasing resolution. Analogously, the size of the simulated clouds scales linearly with the magnitude of the prescribed forcing and the number of grid points per cloud increases linearly with the forcing as well. In contrast, average vertical velocity within the cumulus clouds is found to be quite insensitive to changes in the magnitude of the prescribed forcing. This insensitivity has been observed in earlier studies and is found to be robust over the full range of horizontal resolutions applied in this study.

From this analysis, one can conclude that scaling of cloud and ensemble averaged properties with the magnitude of the forcing observed in the 2 km control simulations is insensitive to changes in the grid spacing. A linear increase of cloud number and cloud size with the forcing is obtained for all grid spacings, whereas cloud vertical velocity is found to be insensitive to changes in forcing. Therefore, it can be concluded, that the expectation that an increase in the magnitude of the forcing primarily increases the number of clouds in the domain without significantly influencing the strength of the clouds, is true in these high-resolution simulations.

**Structure of the simulated cloud fields** Regarding the structure of the simulated cloud fields two significant changes are apparent when increasing horizontal resolution. First, the number of clouds in the domain increases with increasing resolution as the size of the simulated cumulus clouds decreases systematically. This decrease of cloud size is expected as the size of the simulated clouds is strongly limited by the grid scale in the coarse resolution simulations. As the total amount of upward mass flux is constrained by the magnitude of the forcing, it is a natural consequence for the number of clouds in the domain to increase to account for the decreasing cloud size. Convergence of the simulated cloud sizes in the cumulus ensemble was anticipated at high-resolution, but is not seen in the 125 m simulations. Results are in accord with the findings of Craig and Dörnbrack (2008) indicating a grid spacing of 50 m necessary for simulation results to converge. Second, significant changes in the structure of the simulated cloud fields occur with increasing horizontal resolution. Randomly distributed cloud fields are observed in the 2 km resolution control simulations and similar observations are made in the 1 km simulations. However, further increasing horizontal resolution reveals a tendency of the convective clouds to cluster in the simulated domain (500 m resolution simulations). This trend of clustering in the cloud fields further increases with increasing horizontal resolution. In contrast to the randomly distributed cloud fields in the 2 km control simulations, convective clouds are found to cluster in band-like structures around cloud-free areas in the high-resolution, 125 m simulations. This trend of spatial organisation in the high-resolution simulations is

unexpected and likely to influence the shape of the cloud mass flux distributions.

**Validity of the exponential distribution** One main goal of this study is the validation of a theoretical model describing the convective variability within a cumulus cloud ensemble. In this theory, the probability density function of cloud mass flux was predicted to be exponential (CC06 a). Results of the 2 km control simulations compare well to this theoretical prediction over the entire range of prescribed radiative cooling rates. However, when increasing horizontal resolution significant deviations from the theoretical exponential distribution are observed. Stepwise refining the grid spacing increases the number of clouds in the domain, that exhibit larger mass fluxes than predicted by theory. First signs of these deviations are apparent in the 500 m resolution simulations. This is in line with first observing signs of convective clustering in the simulated cloud fields. The deviations from the theoretical exponential distribution increase with increasing resolution and are more distinct when applying a stronger forcing. It is clear from this analysis, that the predicted exponential distribution of cloud mass flux is not valid in high-resolution simulations at a grid spacing of 500 m or smaller. However, after intensively reviewing previous studies, Lennard (2004) indicated that the functional form fitted to a distribution may occasionally be ambiguous. He pointed out, that variations in the distributions of cloud properties may sometimes simply be due to differences in the data analysis techniques, e.g. the distribution may fall to one side of a possible scale break simulating or observing only large clouds.

To facilitate a comparison with the results of CC06 (b) a simple cloud search algorithm is applied in this study. Cloudy grid points are defined if their vertical velocity exceeds a threshold of 1 m/s and condensed cloud water is present in the grid box. Directly connected cloudy grid points are then assigned to the same cloud and cloud properties are computed. Closely evaluating the shape and subcloud structure of the large clouds and cloud systems in this study reveals an interesting fact. Large cloud systems in the high-resolution simulations are found to consist of multiple convective updrafts. These findings are in line with results of Dawe and Austin (2012) and Heus and Seifert (2013). They noted that a common issue in the tracking of shallow cumulus clouds is the problem of overly connected clouds. A cloud in general is not an object but a process, interacting with other clouds (Heus and Seifert, 2013). In cloud tracking studies single clouds are often found to briefly connect in time and space, while mainly keeping their own properties.

Taking the problem of these overly connected clouds into account, motivates the development of a new cloud search algorithm (local-maximum method). This method applies the traditional search algorithm described in Chapter 3 to search the domain for local maxima in the vertical velocity fields. Thereafter, a region growing process is applied following Heus and Seifert (2013) growing a cloud around each cloud core. Application of this local-maximum method on the cloud field partitions the large cloud systems into the single convective updrafts. Mass flux and size probability density functions of the single updrafts compare well to the predicted exponential distribution of CC06 (a). One can conclude that

even though the theoretical, exponential distribution fails to describe the distributions of cloud mass flux in the high-resolution simulations, it is in fact valid if investigating the distribution of mass flux in terms of the single, spatially connected updrafts.

**Presence of a power law distribution** Analogously to the frequency distribution of cloud mass flux, the size distribution of the simulated cumulus clouds is analysed in this resolution sensitivity study. Up to today, no general agreement on a universal functional form of the particular size distribution in a cumulus cloud field has been reached in the scientific community. The shape most often suggested for shallow convective cloud size distribution was a double power law with a distinct scale break at cloud sizes between 400 m and 1 km (Neggers et al., 2003; Dawe and Austin, 2012; Heus and Seifert, 2013). Furthermore, Cahalan and Joseph (1989) noted the size of the scale break to be equal to the size of the largest individual cloud and any cloud larger than this size to actually consist of several smaller, spatially connected clouds. Evaluation of the cloud size distributions in this study reveals a similar development with increasing resolution as observed for the distribution of cloud mass flux. Whereas the distribution is found to strongly resemble an exponential in the 2 km control simulations, a power law-like distribution is obtained in the high-resolution simulations. The power law in the high-resolution simulations however, only poses an adequate fit to cloud sizes larger than 500 m. The large amount of smaller clouds in the domain however, does not compare well to a power law distribution. In fact, the distribution of cloud sizes smaller than 500 m strongly resembles an exponential. Application of the local-maximum method on the cloud fields restores the exponential distribution in terms of the single updrafts in the high-resolution simulations.

Hence, findings of this study do not compare well to the double power law distributions obtained in earlier studies of shallow convection (Cahalan and Joseph, 1989; Neggers et al., 2003; Dawe and Austin, 2012; Heus and Seifert, 2013). In contrast to the double power law with a distinct scale break at a certain cloud size, in this study an exponential distribution up to a cloud size of 500 m with a power law tail for cloud sizes larger than 500 m is found. Furthermore, partitioning the large clouds into their spatially connected, single updrafts restores the exponential distribution. It can hence be concluded that the size of the largest individual updraft determines up to which cloud size the exponential distribution is valid. Clouds larger than this size will then be part of the power law tail of the distribution as they are made up of several of the spatially connected, single updrafts.

**Convergence of simulation results** Recent studies have shown a horizontal grid spacing of order 1 km to be inadequate for resolving subcloud turbulent processes, merely capturing the basic structures of convective clouds. Grid spacings of order 100 m were suggested for traditional large-eddy techniques to perform appropriately to their design and to derive meaningful statistics of a simulated cloud ensemble by accurately resolving important subcloud processes in (Bryan et al., 2003). In contrast, results of Craig and Dörnbrack (2008) indicated a grid spacing of approximately 50 m is necessary to explicitly resolve warm, moist bubble dynamics in the convective atmosphere and for simulation re-

sults to converge.

Evaluating the resolution dependence of the simulated atmosphere in this study does not reveal a clear sign of converging results. However, analysing vertical profiles of the resolved and subgrid turbulent kinetic energy indicates decreasing values of the subgrid turbulent kinetic energy and comparable values of resolved turbulent kinetic energy in the 250 m and 125 m simulations. The ratio of subgrid to total turbulent kinetic energy is found to be approximately 20 % in the high-resolution, strongly forced simulations. However, Bryan et al. (2003) suggested values of 10 % for the traditional large-eddy closures to perform as designed. One-dimensional vertical velocity spectra show comparable positions of the energy peak in the 250 m simulations and the 125 m simulations, which can be interpreted as a sign of convergence. However, the spectra are slightly shallower than  $\kappa^{-5/3}$  beyond the energy containing range. One can assume from this analysis that numerical simulations of deep convection with a horizontal resolution of 125 m are approaching a large-eddy resolving regime. The larger subcloud turbulent processes are resolved, but the simulated large-scale properties have not converged yet.

**Limitations** High-resolution simulations of an ensemble of cumulus clouds in a state of radiative-convective equilibrium are performed in this study. The paradigm of moist convection in a state of radiative-convective equilibrium is highly idealised. This idealised state however, has been useful for understanding many aspects of deep convection in previous studies (Held et al., 1993; Tompkins and Craig, 1998a; Robe and Emanuel, 2001). Several assumptions were made in CC06 (a), deriving the theoretical model that describes convective variability within a cumulus cloud ensemble. First, the simulated domain is large enough to contain many clouds. Second, the large-scale forcing of the convective ensemble varies slowly enough to assume a scale separation in space and time. Third, the convective clouds are randomly distributed throughout the domain and sufficiently separated from one another to neglect cloud-to-cloud interactions.

To facilitate a comparison with their results, the setup of the numerical fluid solver EULAG in this study is undertaken in close agreement to the setup of the cloud-resolving model in CC06 (b). The simulated domain in the 2 km control simulations encompasses  $64 \times 64$  horizontal grid points and is therefore equal in size to the domain of CC06 (b). It is furthermore larger than the minimum domain size denoted in Tompkins and Craig (1998a) and large enough to contain many clouds. However, Cohen and Craig (2006) obtained finite domain effects comparing their  $64 \times 64$  grid point domain with an expanded domain of  $128 \times 128$  grid points. Hence, finite domain effects are expected to be present in this study as well.

Within these simulations, the atmosphere is rendered unstable by applying a horizontally uniform radiative cooling. This homogeneous forcing constitutes a significant simplification as it neglects all cloud-radiative feedbacks. However, applying this uniform forcing fulfills the assumption that the large-scale forcing varies slowly in time and space, and is computationally efficient compared to implementing an interactive radiative scheme. A wide range of magnitudes of the radiative forcing is prescribed in this study, values ranging



from commonly observed -2 K/day to -12 K/day. Prescribed cooling rates of -8 K/day and -12 K/day are much larger than the weak forcing of -1 K/day to -2 K/day that is typically observed over tropical oceans though. These high values of a prescribed forcing are more likely to be associated with cold air outbreaks or large-scale ascent due to topography or approaching fronts. However, applying a strong, horizontally uniform forcing is a very idealised way of investigating cloud development in one of these atmospheric conditions. In contrast to the coarse resolution simulations performed in CC06 (b) and the 2 km simulations in this study, a strong tendency for clouds to develop in the near cloud environment is obtained with increasing horizontal resolution. In the high-resolution simulations, convective clouds are observed to cluster in band-like structures around cloud-free areas. Subsequent changes in the probability density functions of cloud mass flux and cloud size are expected and observed with increasing horizontal resolution. These deviations are directly related to the clustering of convective clouds in the simulated domain. Furthermore, the finite domain size most likely influences the simulated clustering of convective clouds in band-like structures around cloud-free areas.

Other weaknesses in the setup of the numerical model include the application of a very simple one-moment microphysical scheme. More realistic cloud structures and in-cloud properties may be obtained by using a more sophisticated, two-moment microphysical scheme taking into account varying particle number concentrations and different classes of frozen water. This can for example lead to a better representation of the ice microphysical processes in anvil clouds.

In order to prevent the spinup of a mean horizontal wind in the simulations, a Newtonian relaxation of model wind is applied in this study. The subsequent small energy sink in the numerical simulations is responsible for the unexpected decrease of resolved turbulent kinetic energy and the amplitude of the vertical velocity spectra that is observed with increasing horizontal resolution.

First signs of simulation results to converge have been obtained in this study in line with expectations of Bryan et al. (2003). However, Craig and Dörnbrack (2008) indicated convergence of warm moist bubble simulations requires a grid spacing of order 50 m. Further refinement of the grid spacing may hence be necessary, to achieve convergence of the results in this study. With the buoyancy length scale being the most likely candidate for determining the resolution requirement for large-eddy simulations of cumulus clouds, another issue needs to be pointed out. As the buoyancy length scale  $L_{buoy}$  strongly depends on the stratification, values of  $L_{buoy}$  are larger in less stable environments. Considering the trend of decreasing potential temperature lapse rate with increasing magnitude of the prescribed forcing, a dependence of the grid spacing necessary for convergence on the magnitude of the forcing may be the natural consequence.

### Concluding remarks

It can be concluded from this resolution sensitivity study, that the turbulent structures within the cumulus cloud fields become better resolved with increasing horizontal resolution. This facilitates the explicit simulation of turbulent subcloud processes in the high-resolution simulations. As a consequence, the distributions of cloud mass flux and cloud size fail to resemble the predicted exponential in the high-resolution simulations. However, a power law is found to compare well to cloud sizes larger than 500 m. Partitioning the simulated clouds into their single updrafts is found to restore the exponential distribution of size and mass flux. This is an unexpected result, as a main assumption made when deriving the theoretical distribution in CC06 (a), is the clouds to be sufficiently separated from each other to be considered non-interacting. One can conclude from these findings that when increasing horizontal resolution, boundary layer processes like the development of cold pools and moist patches become resolved. Convective clouds are known to develop on top of the moist patches in the boundary layer though. Resolving these boundary layer processes is hence assumed to trigger the clustering of convective clouds in the boundary layer. However, the clouds are found to primarily keep their own properties even though they are spatially connected at upper levels.

### Future work

Evaluating the sensitivity of cumulus cloud properties to the grid spacing has revealed the cloud size distributions to resemble a power law. However, a power law distribution is not a valid fit for cloud sizes smaller than 500 m in the 125 m resolution simulations. A grid spacing of order 50 m was denoted in Craig and Dörnbrack (2008) to explicitly resolve the rising of a warm and moist buoyant bubble in the atmosphere. Performing cloud-resolving simulations of a cumulus cloud ensemble with a grid spacing of order 50 m in future work is therefore desirable to achieve convergence of the results.

Due to boundary layer processes, clouds are found to develop in the near-cloud environment in the high-resolution simulations which causes them to connect and overlap in space and time. However, even though they are connected they primarily keep their own properties in line with findings of Dawe and Austin (2012) and Heus and Seifert (2013). It is observed in this study that these spatially connected and overlapping clouds result in power law-like distributions of cloud size, whereas an exponential is a valid fit for the single, convective updrafts. Further evaluating the effect of connected and overlapping clouds on the shape of the cloud size and mass flux distributions in the context of percolation (Grimmett, 1999) will be a task for future studies.

Regarding the fact, that the exponential is a valid fit to the distribution of the single clouds after partitioning, adapting the theoretical model (CC06 a) to account for the increased clustering of clouds in the domain would be of great interest as well. Furthermore, gaining more knowledge about the underlying processes responsible for the band-like structures observed in the cloud fields is important for understanding cumulus cloud behaviour. Evaluating the connection between the accumulation of moisture around the edges of the

spreading cold pools in the boundary layer and the organisation of convective clouds around cloud-free areas in the troposphere may be a first step in this investigation. In this context, the question is also raised, whether the cloud size at the scale break of cloud size distribution is possibly connected to a length scale of the cold pool structures in the boundary layer.



## List of abbreviations and symbols

CC06	Craig and Cohen (2006) & Cohen and Craig (2006)
CC06 a	Craig and Cohen (2006)
CC06 b	Cohen and Craig (2006)
TR	Traditional Search Algorithm
LM	Local-Maximum Search Algorithm
PDF	Probability Density Function
LES	Large-Eddy Simulation
SGS	Subgrid Scale model
RCE	Radiative-Convective Equilibrium
SST	Sea Surface Temperature
tk <sub>e</sub>	Turbulent Kinetic Energy
m <sub>se</sub>	Moist Static Energy
$L_{buoy}$	Buoyancy length scale
EULAG	EUlerian/semi-LAGrangian fluid solver
MPDATA	Multidimensional Positive Definite Advection Transport Algorithm
NFT	Nonoscillatory Forward-in-Time approach
MPI	Message Passing Interface
NPE	Optimal Number of Processors for domain decomposition
n, m	Number of grid points in x- and y-direction
$q_v$	Water vapour mixing ratio
$q_c$	Cloud condensed water mixing ratio
$q_r$	Rain water mixing ratio

---

$\bar{\mathbf{u}}$	Three-dimensional velocity vector
$\theta'$	Deviation of potential temperature from the ambient model state
$H_D$	Damping layer height scale
$z_D$	Height of the lowest model layer where damping is applied
$\tau_{damp}$	Damping coefficient
$\tau_{relax}$	Newtonian relaxation time scale
$T_{surf}$	Temperature at lowest model layer, taken to be equal to the sea surface temperature
$Q_{rad}$	Prescribed radiative cooling rate
$Q_{rad-eff}$	Effective radiative cooling rate
$d\theta/dz$	Potential temperature lapse rate
$w_i$	Vertical velocity in a cloud
$\sigma_i$	Size of a cloud
$\rho$	Density of air
$m_i$	Vertical mass flux in a cloud
$\langle m \rangle$	Ensemble average cloud mass flux
$\langle N \rangle$	Average number of clouds in the domain

# Bibliography

- Adlerman, E. J. and Droegemeier, K. K. 2002. The sensitivity of numerically simulated cyclic mesocyclogenesis to variations in model physical and computational parameters. *Monthly Weather Review*, 130:2671–2691.
- Arakawa, A. 2004. The cumulus parameterisation problem: Past, present and future. *Journal of Climate*, 17:2493–2525.
- Arakawa, A. and Schubert, W. H. 1974. Interaction of a cumulus cloud ensemble with the large-scale environment, Part I. *Journal of the Atmospheric Sciences*, 31:674–701.
- Asai, T. and Najasuji, I. 1977. On the preferred mode of cumulus convection in a conditionally unstable atmosphere. *Journal of the Meteorological Society of Japan*, 55:151–167.
- Berry, E. X. Modification of the warm rain process. In *Pp. 81-85 in Proceedings of the 1st National conference of weather modification*.
- Betts, A. K. 1986. A new convective adjustment scheme. Part I: Observational and theoretical basis. *Quarterly Journal of the Royal Meteorological Society*, 112:677–692.
- Betts, A. K. and Miller, M. J. 1986. A new convective adjustment scheme. Part II: Single column tests using GATE wave, BOMEX, ATEX, and arctic air-mass data sets. *Quarterly Journal of the Royal Meteorological Society*, 112:693–710.
- Boing, S. J., Jonker, H. J. J., Siebesma, A. P., and Grabowski, W. W. 2012. Influence of the subcloud layer on the development of a deep convective ensemble. *Journal of the Atmospheric Sciences*, 69:2682–2698.
- Bright, D. R. and Mullen, S. L. 2002. Short-range ensemble forecasts of precipitation during the southwest monsoon. *Weather and Forecasting*, 17:1080–1100.
- Bryan, G. H., Wyngaard, J. C., and Fritsch, M. J. 2003. Resolution requirements for the simulation of deep moist convection. *Monthly Weather Review*, 131:2394–2416.
- Buizza, R., Miller, M., and Palmer, T. N. 1999. Stochastic representation of model uncertainties in the ECMWF ensemble prediction system. *Quarterly Journal of the Royal Meteorological Society*, 125:2887–2908.

- Cahalan, R. F. and Joseph, J. H. 1989. Fractal statistics of cloud fields. *Monthly Weather Review*, 117:261–272.
- Clark, T. L. 1977. A small-scale dynamic model using a terrain-following coordinate transformation. *Journal of Computational Physics*, 24:186–214.
- Clark, T. L. 1979. Numerical simulations with a three-dimensional cloud model: Lateral boundary condition experiments and multicellular severe storm simulations. *Journal of Atmospheric Sciences*, 36:2191–2215.
- Cohen, B. G. 2001. Fluctuations in an ensemble of cumulus clouds. *Ph.D. Thesis, University of Reading*.
- Cohen, B. G. and Craig, G. C. 2006. Fluctuations in an equilibrium convective ensemble. Part II: Numerical experiments. *Journal of the Atmospheric Sciences*, 63:2005–2015.
- Craig, G. C. and Cohen, B. G. 2006. Fluctuations in an equilibrium convective ensemble. Part I: Theoretical formulation. *Journal of the Atmospheric Sciences*, 63:1996–2004.
- Craig, G. C. and Dörnbrack, A. 2008. Entrainment in cumulus clouds: What resolution is cloud-resolving. *Journal of the Atmospheric Sciences*, 65:3978–3988.
- Dahl, J. M. L. 2010. The development of a new lightning-frequency parameterisation and its implementation in a weather prediction model. *Ph. D. Thesis, Ludwig-Maximilians University, Munich*.
- Dawe, J. T. and Austin, P. H. 2012. Statistical analysis of a LES shallow cumulus cloud ensemble using a cloud tracking algorithm. *Atmospheric Chemistry and Physics*, 12:1101–1119.
- Deardorff, J. W. 1973. The use of subgrid transport equations in a three-dimensional model of atmospheric turbulence. *Journal of Fluids Engineering*, 95:429–438.
- Droegemeier, K. K., Richardson, Y. P., Bassett, G. M., and Marroquin, A. 1997. Three-dimensional numerical simulations of turbulence generated in the near-environment of deep convective storms. *Seventh Conference on Aviation, Range and Aerospace Meteorology*, Long Beach, CA, American Meteorological Society:169–174.
- Emanuel, K. A. 1994. *Atmospheric convection*, chapter 1–3. Oxford University Press.
- Emanuel, K. A. and Rothman, M. Z. 1999. Development and evaluation of a convection scheme for use in climate models. *Journal of the Atmospheric Sciences*, 56:1766–1782.
- Fritsch, J. M. and Chappell, C. F. 1980. Numerical prediction of convectively driven mesoscale pressure systems. Part I: Convective parameterisation. *Journal of the Atmospheric Sciences*, 37:1722–1733.



- Grabowski, W. W. 1988. On the bulk parameterisation of snow and its application to the quantitative studies of precipitation growth. *Pure and Applied Geophysics*, 122:79–92.
- Grabowski, W. W. 1998. Toward cloud resolving modeling of large-scale tropical circulations: A simple cloud microphysics parameterisation. *Journal of the Atmospheric Sciences*, 55:3283–3298.
- Grabowski, W. W. and Morrison, H. 2008. Toward the mitigation of spurious cloud-edge supersaturation in cloud models. *Monthly Weather Review*, 136:1224–1234.
- Grabowski, W. W. and Smolarkiewicz, P. K. 1990. Monotone finite-difference approximations to the advection-condensation problem. *Monthly Weather Review*, 118:2082–2097.
- Grabowski, W. W. and Smolarkiewicz, P. K. 2002. A multiscale anelastic model for meteorological research. *Monthly Weather Review*, 130:939–956.
- Grell, G. 1993. Prognostic evaluation of assumptions used by cumulus parameterisations. *Monthly Weather Review*, 121:764–787.
- Grimmett, G. 1999. *Percolation: What is Percolation*, pages 1–31. Springer Verlag Berlin Heidelberg.
- Held, I. M., Hemler, R. S., and Ramaswamy, V. 1993. Radiative-convective equilibrium with explicit two-dimensional moist convection. *Journal of the Atmospheric Sciences*, 50:3909–3927.
- Heus and Seifert 2013. Automated tracking of shallow cumulus clouds in large domain, long duration large eddy simulations. *Geoscientific Model Development*, 6:1261–1273.
- Hoshen, J. and Kopelman, R. 1976. Percolation and cluster distribution. I. Cluster multiple labeling technique and critical concentration algorithm. *Physical Review B*, 14:3438–3445.
- Hozumi, K., Harimaya, T., and Magono, C. 1982. The size distribution of cumulus clouds as a function of cloud amount. *Journal of the Meteorological Society of Japan*, 60:691–699.
- Hsie, E. Y., Farley, R. D., and Orville, H. D. 1980. Numerical simulation of ice phase convective cloud seeding. *Journal of Applied Meteorology*, 19:950–977.
- Islam, S., Bras, R. L., and Emanuel, K. A. 1993. Predictability of mesoscale rainfall in the tropics. *Journal of Applied Meteorology*, 32:297–310.
- Johnson, R. H., Rickenbach, T. M., Rutledge, S. A., Ciesielski, P. E., and Schubert, W. H. 1999. Trimodal characteristics of tropical convection. *Journal of Climate*, 12:2397–2418.
- Jonas, P. R. 1990. Observations of cumulus cloud entrainment. *Atmospheric Research*, 25:105–127.

- Jordan, C. L. 1958. Mean soundings for the West Indies area. *Journal of Meteorology*, 15:91–97.
- Kain, J. S. and Fritsch, J. M. 1993. Convective parameterisation for mesoscale models: The Kain-Fritsch scheme. The representation of cumulus convection in numerical models. *Meteorological Monographs*, 24:165–170.
- Kessler, E. 1969. On the distribution and continuity of water substance in atmospheric circulations. *Meteorological Monographs*, 10(32).
- Khairoutdinov, M. F., Krueger, S. K., Moeng, C., Bogenschutz, P. A., and Randall, D. A. 2009. Large-eddy simulation of maritime deep tropical convection. *Journal of Advances in Modeling Earth Systems*, 1(15):1–13.
- Khouider, B., Majda, A. J., and Katsoulakis, A. 2003. Coarse grained stochastic models for tropical convection and climate. *Proceedings of the National Academy of Sciences USA*, 100:11941–11946.
- Kolmogorov, A. N. 1941. The local structure of turbulence in incompressible viscous fluid for very large Reynolds numbers. *Doklady Akademii Nauk*, 30:299–303.
- Kuo, K. S., Welch, R. M., Weger, R. C., Engelstad, M. A., and Sengupta, S. K. 1993. The three-dimensional structure of cumulus clouds over the ocean: 1. Structural analysis. *Journal of Geophysical Research*, 98:20685–20711.
- LeMone, M. A. and Zipser, E. J. 1980. Cumulonimbus vertical velocity events in GATE. Part I: Diameter, intensity and mass flux. *Journal of the Atmospheric Sciences*, 37:2444–2457.
- Lennard, R. 2004. The distribution of cumulus cloud sizes. *M.S. Thesis, University of Reading*, pages 1–67.
- Lilly, D. K. 1962. On the numerical simulation of buoyant convection. *Tellus*, 14:148–172.
- Lilly, D. K. 1967. *The representation of small-scale turbulence in numerical simulations experiments*, pages 195–210. Proc. IBM Scientific Symp. on Environmental Sciences, Yorktown Heights, NY, IBM DP Division.
- Lilly, D. K. 1987. *Modes of turbulence in stably stratified environments: Part II*, chapter Lecture Notes on Turbulence. J. R. Herring and J. C. McWilliams, Eds., World Scientific.
- Lin, J. W.-B. and Neelin, J. D. 2003. Toward stochastic deep convective parameterisation in general circulation models. *Geophysical Research Letter*, 30:doi:10.1029/2002GL016203.
- Lin, Y. L., Farley, R. D., and Orville, H. D. 1983. Bulk parameterisation of the snow field in a cloud model. *Journal of Climate and Applied Meteorology*, 22:1065–1092.

- Lipps, F. B. and Helmer, R. S. 1986. Numerical simulation of deep tropical convection associated with large-scale convergence. *Journal of the Atmospheric Sciences*, 43:1796–1816.
- Lopez, R. E. 1977. The lognormal distribution and cumulus cloud populations. *Monthly Weather Review*, 105:865–872.
- Machado, L. A. T. and Rossow, W. B. 1993. Structural characteristics and radiative properties of tropical cloud clusters. *Monthly Weather Review*, 121:3234–3260.
- Manabe, S. and Strickler, R. F. 1964. Thermal equilibrium of the atmosphere with a convective adjustment. *Journal of the Atmospheric Sciences*, 21:361–385.
- Margolin, L. G., Smolarkiewicz, P. K., and Sorbjan, Z. 1999. Large-eddy simulations of convective boundary layers using nonoscillatory differencing. *Physica D*, 133:390–397.
- Moeng, C.-H. 1984. A large-eddy simulation model for the study of planetary boundary-layer turbulence. *Journal of the Atmospheric Sciences*, 41:2052–2062.
- Moorthi, S. and Suarez, M. J. 1992. Relaxed Arakawa-Schubert. A parameterisation of moist convection for general circulation models. *Monthly Weather Review*, 120:978–1002.
- Nair, U. S., Weger, P. C., Kuo, K. S., and Welch, R. M. 1998. Clustering, randomness, and regularity in cloud fields: 5. The nature of regular cumulus cloud fields. *Journal of Geophysical Research*, 103:11363–11380.
- Neggers, R. A. J., Jonker, H. J. J., and Siebesma, A. P. 2003. Size statistics of cumulus cloud populations in large-eddy simulations. *Journal of the Atmospheric Sciences*, 60:1060–1074.
- Nitta, T. 1975. Observational determination of cloud mass flux distributions. *Journal of the Atmospheric Sciences*, 32:73–91.
- Palmer, T. N. 2001. A nonlinear dynamical perspective on model error: A proposal for non-local stochastic-dynamic parameterisation in weather and climate prediction models. *Quarterly Journal of the Royal Meteorological Society*, 127:279–304.
- Parodi, A. and Emanuel, K. 2009. A theory for buoyancy and velocity scales in deep moist convection. *Journal of the Atmospheric Sciences*, 66:3449–3463.
- Pauluis, O. and Held, I. M. 2002. Entropy budget of an atmosphere in radiative-convective equilibrium. Part I: Maximum work and frictional dissipation. *Journal of the Atmospheric Sciences*, 59:125–139.
- Petch, J. C. and Gray, M. E. B. 2001. Sensitivity studies using a cloud-resolving model simulation of the tropical west pacific. *Quarterly Journal of the Royal Meteorological Society*, 127:2287–2306.

- Piotrowski, Z. P., Wyszogrodzki, A. A., and Smolarkiewicz, P. K. 2011. Towards petascale simulation of atmospheric circulations with soundproof equations. *Acta Geophysica*, 59:1294–1311.
- Plank, V. G. 1969. The size distribution of cumulus clouds in representative Florida populations. *Journal of Applied Meteorology*, 8:46–67.
- Plant, R. S. and Craig, G. C. 2008. A stochastic parameterisation for deep convection based on equilibrium statistics. *Journal of the Atmospheric Sciences*, 65:87–105.
- Prusa, J. M., Smolarkiewicz, P. K., and Wyszogrodzki, A. A. 2008. EULAG, a computational model for multiscale flows. *Computers and Fluids*, 37:1193–1207.
- Randall, D. A., Xu, K.-M., Hu, Q., and Krueger, S. 1994. Radiative-convective disequilibrium. *Atmospheric Research*, 31:315–327.
- Robe, F. R. and Emanuel, K. A. 1996. Moist convective scaling: Some inferences from three-dimensional cloud ensemble simulations. *Journal of the Atmospheric Sciences*, 53:3265–3275.
- Robe, F. R. and Emanuel, K. A. 2001. The effect of vertical wind shear on radiative-convective equilibrium states. *Journal of the Atmospheric Sciences*, 58:1427–1445.
- Romps, D. M. 2010. A direct measure of entrainment. *Journal of the Atmospheric Sciences*, 67:1908–1927.
- Schlemmer, L. and Hohenegger, C. 2014. The formation of wider and deeper clouds as a result of cold-pool dynamics. *Journal of the Atmospheric Sciences*, doi: <http://dx.doi.org/10.1175/JAS-D-13-0170.1>.
- Schumann, U. 1987. Minimum friction velocity and heat transfer in the rough surface layer of a convective boundary layer. *Boundary Layer Meteorology*, 44:311–326.
- Schumann, U. 1991. Subgrid length-scales for large-eddy simulation of stratified turbulence. *Theoretical and Computational Fluid Dynamics*, 2:279–290.
- Sengupta, S. K., Welch, R. M., Navar, M. S., Berendes, T. A., and Chen, D. W. 1990. Cumulus cloud field morphology and spatial patterns derived from high spatial resolution landsat imagery. *Journal of Applied Meteorology*, 29:1245–1267.
- Shutts, G. J. and Gray, M. E. B. 1999. Numerical simulations of convective equilibrium under prescribed forcing. *Quarterly Journal of the Royal Meteorological Society*, 125:2767–2787.
- Siebesma, A. P. and Cuijpers, J. W. M. 1995. Evaluation of parametric assumptions for shallow cumulus convection. *Journal of the Atmospheric Sciences*, 52:650–666.

- Simpson, J. and Wiggert, V. 1969. Models of precipitating cumulus towers. *Monthly Weather Review*, 97:471–489.
- Smagorinsky, J. 1963. General circulation experiments with the primitive equations: I. The basic experiment. *Monthly Weather Review*, 91:99–164.
- Smith, R. K. 1997. *The physics and parameterisation of moist atmospheric convection*. Kluwer Academic Publishers.
- Smolarkiewicz 2005. Towards mesh adaptivity for geophysical turbulence: Continuous mapping approach. *International Journal for Numerical Methods in Fluids*, 47:789–801.
- Smolarkiewicz, P. K., Grubisic, V., Margolin, L. G., and Wyszogrodzki, A. A. 1998. Forward-in-time differencing for fluids: Nonhydrostatic modeling of fluid motions on a sphere. In *Proc. 1998 ECMWF Seminar on Recent Developments in Numerical Methods for Atmospheric Modeling*, pages 21–43.
- Smolarkiewicz, P. K. and Margolin, L. G. 1997. On forward-in-time differencing for fluids: An Eulerian/semi-Lagrangian non-hydrostatic model for stratified flows. *Atmosphere–Ocean*, 35:127–152.
- Smolarkiewicz, P. K. and Margolin, L. G. 1998. MPDATA: A finite-difference solver for geophysical flows. *Journal of Computational Physics*, 140:459–480.
- Sorbjan, Z. 1996. Numerical study of penetrative and "Solid Lid" nonpenetrative convective boundary layers. *Journal of the Atmospheric Sciences*, 53:101–112.
- Stevens, B. 2005. Atmospheric moist convection. *Annual Review of Earth and Planetary Sciences*, 33:605–648.
- Stevens, D. E., Ackerman, A. S., and Bretherton, C. S. 2002. Effects of domain size and numerical resolution on the simulation of shallow cumulus convection. *Journal of the Atmospheric Sciences*, 59:3285–3301.
- Stull, R. B. 1994. A convective transport theory for surface fluxes. *Journal of the Atmospheric Sciences*, 51:3–22.
- Tiedtke, M. 1989. A comprehensive mass flux scheme for cumulus parameterisation in large-scale models. *Monthly Weather Review*, 117:1779–1800.
- Tompkins, A. M. 2001. Organization of tropical convection in low vertical wind shears: The role of cold pools. *Journal of the Atmospheric Sciences*, 58:1650–1672.
- Tompkins, A. M. and Craig, G. C. 1998a. Radiative–convective equilibrium in a three-dimensional cloud-ensemble model. *Quarterly Journal of the Royal Meteorological Society*, 124:2073–2097.

- Tompkins, A. M. and Craig, G. C. 1998b. Timescales of adjustment to radiative–convective equilibrium in the tropical atmosphere. *Quarterly Journal of the Royal Meteorological Society*, 124:2693–2713.
- Warner, J. 1977. Time variation of updraft and water content in small cumulus clouds. *Journal of the Atmospheric Sciences*, 34:1306–1312.
- Weisman, M. L., Skamarock, W. C., and Klemp, J. B. 1997. The resolution dependence of explicitly modeled convective systems. *Monthly Weather Review*, 125:527–548.
- Wielicki, B. A. and Welch, R. M. 1986. Cumulus cloud properties derived using landsat satellite data. *Journal of Applied Meteorology and Climatology*, 25:261–276.
- Wilks, D. S. 2005. Effects of stochastic parameterisations in the Lorentz ’96 system. *Quarterly Journal of the Royal Meteorological Society*, 131:389–407.
- Xu, K. M., Arakawa, A., and Krueger, S. K. 1992. The macroscopic behaviour of cumulus ensembles simulated by a cumulus ensemble model. *Journal of the Atmospheric Sciences*, 49:2402–2420.

# Acknowledgements

First and foremost, I would like to thank Prof. Dr. George C. Craig who provided me with the opportunity to undertake this thesis. His guidance, valuable suggestions and encouraging way of thinking about problems from all possible perspectives, contributed significantly to this work.

I would also like to thank Prof. Dr. Roger K. Smith for reviewing this thesis as co-examiner.

I am deeply grateful to Dr. Andreas Dörnbrack (DLR, Oberpfaffenhofen) for his time and advice whenever needed, regarding model setup and technical issues. His comments on numerical problem-solving were invaluable.

In this context, great thanks also goes to Dr. Andrzej Wyszogrodzki and Dr. Wojtek Grabowski (NCAR, Boulder) for their helpful suggestions and numerous advice in numerical simulation matters.

I would also like to acknowledge the supercomputer facilities at the Deutsches Klimarechenzentrum (DKRZ) and the Gauss Centre for Supercomputing e.V. for funding this project by providing computing time.

In addition, I would like to thank all my colleagues at the Meteorological Institute at LMU Munich for the friendly work environment, fruitful discussions and many coffee break chats. Special thanks goes to Renate Wilcke, Lotte Bierdel, Claudia Eller and Susanne Lurtz for proofreading, their insightful comments and many suggestions that helped improve this thesis. Moreover, I would like to thank my room mates in the last years, Kathrin and Richard, for many encouraging and motivating words when needed most.

Most deeply I would like to thank my family for their constant support in every possible way and to my closest friends for continuously encouraging and reminding me that there is a life beside work.





# Curriculum vitae

Katrin Scheufele

Born on 20 June 1986 in Weingarten, Germany

## PUBLICATIONS

Scheufele et al., 2014: *Combining probabilistic precipitation forecasts from a nowcasting technique with a time-lagged ensemble*. Meteorological Applications, 21, 230-240.

## UNIVERSITY EDUCATION

2010 - 2014	Ph.D. student at Ludwig-Maximilians Universität München
August 2010	Diploma in Meteorology Diploma Thesis at Deutsches Zentrum für Luft- und Raumfahrt, Institut für Physik der Atmosphäre, Oberpfaffenhofen: "Probabilistic forecasting of precipitation by combining nowcasts and the time-lagged COSMO-DE ensemble"
March 2009	Internship at the Bureau of Meteorology, Brisbane, Australia
August 2007	Internship at the Meteorologisches Observatorium, Lindenberg
2005 - 2010	Study of Meteorology at the Ludwig-Maximilians Universität München

## PRIMARY AND SECONDARY SCHOOL

2003 - 2005	Josef-Effner-Gymnasium, Dachau
2002 - 2003	Angleton High-School, TX, USA
1996 - 2002	Josef-Effner-Gymnasium, Dachau
1993 - 1996	Primary School, Hebertshausen
1992 - 1993	Primary School, Schorndorf-Weiler